Orbit based treatments of quantum interference in atomic and molecular high-order harmonic generation

by

Bradley Bernhard Augstein
Under the supervision of Doctor Carla Figueira de Morisson Faria
and the subsidiary supervision of Professor Roy Newell

A thesis submitted in partial fulfillment for the
degree of Doctor of Philosophy

University College London
Department of Physics and Astronomy

Examination committee:
Professor Jon P. Marangos, Department of Physics (Imperial College London)
Professor Doctor Jan-Michael Rost, Physik Komplexer Systeme (Max-Planck Institut)

June 2012

Declaration of authorship

I, Bradley Bernhard Augstein, declare that this thesis titled 'Orbit based treatments of interference in atomic and molecular high-order harmonic generation' and the work presented in it is my own. I confirm that:

- This work was done wholly or mainly while in candidature for a research degree at this University.
- Where any part of this thesis has previously been submitted for a degree or any other qualification at this University or any other institution, this has been clearly stated.
- Where I have consulted the published work of others, this is always clearly attributed.
- Where I have quoted from the work of others, the source is always given. With the exception of such quotations, this thesis is entirely my own work.
- I have acknowledged all main sources of help.
- Where the thesis is based on work done by myself jointly with others, I have made clear exactly what was done by others and what I have contributed myself.

Signed: _____

Date: _____

"Out of clutter find simplicity; From discord find harmony; In the middle of difficulty lies opportunity"

Albert Einstein

Abstract

Orbit-based theoretical approaches to modelling strong field phenomena allow physical intuition to be extracted from complex multi-dimensional quantum processes. High-order harmonic generation (HHG) has been interpreted relatively successfully for almost two decades as a three step process in which an ionized electron is accelerated by the field and recombines with its parent ion, resulting in high-order multiples of the laser frequency. This process is often modelled within the strong-field approximation (SFA), where the effect of the Coulomb potential on the electron is neglected while the electron is accelerated by the field, and the single-active electron (SAE) approximation. The SFA provides an appealing interpretation of HHG in terms of interfering electron trajectories. Although successful in reproducing experimental observables in atomic systems, in recent years the importance of multi-electron effects, molecular orbital symmetry and the Coulomb potential in atoms and diatomic molecules have been seen experimentally and theoretically. These effects, neglected by the original SFA formulation, mean that either modifications to the original SFA, or new trajectory based theories, are essential for a more complete physical understanding of the HHG phenomenon.

This thesis investigates these effects in HHG from homonuclear and heteronuclear diatomic molecules in strong fields. We model and assess the importance of multiple molecular orbital contributions, molecular orbital geometry and two-centre interference on the HHG spectrum. These problems are approached within a semi-analytical, SFA, framework and with a static core. It is found that these effects can be seen in the HHG spectrum. By predicting novel features in the spectrum arising from such effects we obtain not only a better understanding and interpretation of current experimental results, but also new insight and applicability to molecular imaging.

In addition to these modifications, a new theoretical approach, the coupled coherent state (CCS) method is used to model Hydrogen in an intense field, although it can be extended to multi-electron systems and diatomic molecules. In the CCS method, the Coulomb potential is fully included at all stages in the HHG process, and most notably, during the electron propagation, where it is neglected by the SFA. The CCS method has favourable scaling with dimensionality, compared to other numerical approaches, as well as being fully quantum. It is trajectory based, facilitating comparison with the three step model and the strong field approximation. Therefore we benefit from the physical intuition of semi-classical approaches but within a fully quantum framework and without the approximations of semi-analytical methods.

Acknowledgements

My greatest thanks are to Dr. Carla Figueira de Morisson Faria for her guidance, belief and encouragement. I am grateful to the United Kingdom Physical Sciences Research Council and the Science and Technologies Facilities Council for funding my PhD. In extending the coupled coherent state code and for fruitful discussions I would like to acknowledge Dr. Dmitry Shalashilin at the University of Leeds and Dr. Adam Kirrander at Laboratoire Aimé Cotton, as well as Mr. Wu Jie at University College London. For advice and discussion on the use of the GAMESS-UK code my thanks go to to Dr. Huub van Damm, Dr. Paul Sherwood and Dr. Paul Durham at the Daresbury Laboratories, Prof. Jonathan Tennyson at University College London and Dr. Ricardo Torres at Imperial College London. For help with numerical problems I am extremely thankful to Mr. Tuomas Nygren. For extensive assistance with the Qprop code I am very thankful to Prof. Dr. Dieter Bauer. For all research related issues and guidance I am grateful to Tahir Shaaran. Finally, I am grateful to my family and friends for their love and support, and especially my parents, Alvin Bruce Augstein and Amanda Louise Augstein.

Frame of this research

This work was mainly carried out at the Physics and Astronomy department of Universtity College from October 2008 until October 2011, under the supervision of Dr. Carla Figueira de Morisson Faria and the subsidiary supervision of Prof. Roy Newell. However, it also includes collaborations with Prof. Dr. Dieter Bauer at the University of Rostock, Dr. Dmitry Shalashilin at the University of Leeds, Dr. Adam Kirrander at the Laboratoire Aimé Cotton and Dr. Paul Durham at Daresbury Laboratories. Parts of this thesis may be found in the following publications:

Paper 1: C. Figueira de Morisson Faria and B. B. Augstein, 'Molecular high-order harmonic generation with more than one active orbital: Quantum interference effects', Phys. Rev. A, **81**, 043409 (2010) (reference [1])

Paper 2: B. B. Augstein and C. Figueira de Morisson Faria, 'Multielectron corrections in molecular high-order harmonic generation for different formulations of the strong-field approximation', J. Mod. Opt., **58**, 1173 (2011) (reference [2])

Paper 3: B. B. Augstein and C. Figueira de Morisson Faria, 'Influence of asymmetry and nodal structures on high-harmonic generation in heteronuclear molecules', J. Phys. B, **44**, 055601 (2011) (reference [3])

Paper 4: T. Shaaran, B. B. Augstein and C. Figueira de Morisson Faria, 'Excitation, two-center interference and the orbital geometry in laser-induced nonsequential double ionization of diatomic molecules', Phys. Rev. A, **84**, 013429 (2011) (reference [4])

Paper 5: B. B. Augstein and C. Figueira de Morisson Faria, 'High-order harmonic generation in diatomic molecules: Quantum interference, nodal structures and multiple orbitals', Mod. Phys. Lett. B, accepted (2011) (reference [5])

Paper 6: B. B. Augstein, J. Wu, A. Kirrander, D. V. Shalashilin and C. Figueira de Morisson Faria, 'High-order harmonic generation in single electron atoms: The coupled coherent state approach', in preparation (2012) (reference [2])

In this thesis, the content of paper 1 mainly appears in Chapter 5 and Chapter 7, paper 2 is presented in Chapter 6 and paper 3 is found in Chapter 8. I am the first author in all papers except for paper 1 and paper 4. In these papers I contributed to constructing the molecular wavefunctions, which is described in Chapter 4. I also assisted in developing the mathematics and programming in paper 1.

Contents

Declaration of authorship i

Abstract iii

Acknowledgements iv

Frame of this research v

List of figures ix

List of tables xiv

1 Overview 1

2 Introduction 4
2.1 Historical overview . . . 4
2.2 Multi-electron effects and orbital symmetry . . . 9
2.3 Two-centre interference . . . 11
2.4 Coulomb effects . . . 14
2.5 Increasing the harmonic cutoff . . . 15
2.6 Heteronuclear molecules and orbital symmetry . . . 16

3 Theoretical approaches 17
3.1 Physical framework . . . 17
3.2 Forms of the dipole operator . . . 18
3.3 Numerical solutions to the time-dependent Schrödinger equation . . . 20
3.4 Classical interpretation . . . 22
3.5 Classical and semi-classical trajectory-based approaches . . . 24
3.6 The coupled coherent state approach . . . 25

4 The strong-field approximation 26
4.1 Traditional SFA . . . 26
4.1.1 SFA transition amplitude . . . 26
4.1.2 Saddle-point approximation . . . 30

4.1.3 Uniform approximation . . . 33
4.2 Extension to diatomic molecules . . . 33
4.2.1 Gaussian vs Slater basis sets in molecular orbital construction . . . 35
4.2.2 Analytical form of the dipole matrix elements . . . 37
4.2.3 Interference condition . . . 38
4.2.4 Modified saddle-point equations . . . 39

5 Multi-electron ground state wavefunction 43
5.1 Theory . . . 44
5.2 Influence of the HOMO-1 on the harmonic spectra . . . 48
5.3 Conclusions . . . 51

6 Multi-electron Lewenstein ansatz 53
6.1 Theory . . . 53
6.2 Harmonic spectra including multi-electron effects . . . 58
6.3 Conclusions . . . 66

7 Coherent superposition of molecular orbitals 68
7.1 Theory . . . 68
7.2 Imprints of orbital structure . . . 69
7.3 Conclusions . . . 72

8 Asymmetry and nodal structures in heteronuclear molecules 74
8.1 Signatures of nodal structures in high-order harmonic generation . . . 76
8.1.1 Standard SFA . . . 77
8.1.2 Importance of exchange harmonics . . . 81
8.2 Conclusions . . . 82

9 Coupled coherent states 84
9.1 Model . . . 85
9.1.1 Static basis representation . . . 86
9.1.2 Dynamic basis representation . . . 87
9.1.3 Assessing the dipole operator . . . 89
9.2 Sampling . . . 90
9.3 Results . . . 90
9.4 Conclusions and outlook . . . 93

10 Summary 95

A List of abbreviations 97

B Atomic units 98

C Gauge transformations 99

D Azimuthal angular integration 100

E Overalp integrals for multi-electron corrections **103**
E.0.1 Length form . . . 103
E.0.2 Velocity form . . . 104
E.0.3 Specific integrals for J and K . . . 105

F Derivation of the multi-electron dipole matrix element **107**

G Derivation of the dipole matrix elements in the CCS basis **110**
G.1 Length form . . . 110
G.2 Velocity form . . . 110
G.3 Acceleration form . . . 111

Bibliography **113**

List of Figures

2.1 Some of the main results resulting from the HHG mechanism. a) An early harmonic spectrum from atomic Ar in an Nd:YAG laser. From reference [6]. b) A tomographic reconstruction of the HOMO of N_2. From reference [7]. c) Kinetic energy spectra of electrons detached from a neon atom versus the delay between the attosecond pulse and the strong femtosecond pulse. From reference [8]. d) Hole dynamics measured using the harmonic spectrum in CO_2: 1) initial hole density 2) shape after a quarter period 3) after a half period. From reference [9] 6

2.2 Illustration of the three step process for a system of ionization potential I_p. The steps are 1) tunnelling ionization from the Coulomb potential which has been deformed by the strong laser field 2) acceleration of the electron by the laser field 3) recombination with the core leading to the generation of a high-energy photon. From reference [10]. 7

2.3 Ionization and recombination times during the laser field cycle for a given harmonic. The right hand panel shows a cosine laser field of wavelength $\lambda = 800nm$ and intensity $1.2 \times 10^{14} W cm^{-2}$. The left panel depicts the times of ionization and recombination for a given energy of recollision. The dashed line corresponds to long trajectories and the solid line to short trajectories. From reference [11]. 7

2.4 Schematic representation of destructive two-center interference occurring when a plane wave of wavelength λ_k collides with a diatomic molecule of internuclear separation, R, aligned at an angle θ_L, relative to the linearly polarized laser field. 12

2.5 Schematic representation of a) an oriented sample of heteronuclear molecules and b) an aligned sample of heteronuclear molecules. The arrow on the right hand side of the figure indicates the linearly polarized laser field direction. 16

4.1 Real part of the start time, t', and recombination times, t, shown in the lower and upper panels, respectively, of electron trajectories for a harmonic of order n. We are using a continuous wave sin field. The dashed and solid lines correspond to the long and short trajectories, respectively. Red lines correspond to ionization and recombination in the first cycles and black lines to ionization in the first cycle and recombination in the second cycle. The blue lines represent the similar trajectories as those by the red lines except occuring 0.5 cycles later. 32

4.2 Comparison of a Slater type orbital (STO) used for a 1s atomic state and its approximation with one, two and three contractions of Gaussian type orbitals (GTO) [12]. The coefficients for the GTO are obtained using a least squares fit. 35

4.3 Molecular orbitals in position space corresponding to a) the HOMO, which is a $3\sigma_g$ type orbital b) the HOMO-1 which is a $1\pi_u$ type orbital and c) the LUMO, which is a $1\pi_g$ type orbital, of N_2. We use a LCAO with 6-31G split valence basis and an equilibrium internuclear separation of 2.068 a.u. The energies of these orbitals are $E_{3\sigma_g}$=-0.63485797 a.u., $E_{1\pi_u}$=-0.65087981 a.u. and $E_{1\pi_g}$=0.17238733 a.u., respectively. 36

4.4 High-order harmonic spectra for the HOMO in N_2 subject to a linearly polarized laser field of frequency $\omega = 0.057$ a.u. and intensity $I = 4 \times 10^{14} W cm^{-2}$, as a function of the alignment angle θ_L between the molecular axis and the field. The spectra in the upper panels have been constructed using a gaussian basis set and coefficients obtained from GAMESS-UK [13], while those in the lower panels have been built using Slater-type orbitals, and the coefficients in [14]. From left to right, we display the spectra from the full $3\sigma_g$ orbital [panels (a) and (d)], the contributions from the s states [panels (b) and (e)], and those from the p states [panels (c) and (f)]. The bound-state energy of the HOMO and the equilibrium internuclear distance have been taken from the respective computations. For the upper panels, $E_{3\sigma_g} = 0.63485797$ a.u., while for the lower panels $E_{3\sigma_g} = 0.63495$ a.u. In both cases, $R = 2.068$ a.u. 40

4.5 Schematic of contributions to the overall harmonic yield when incorporating the molecular structure of a diatomic molecule into the action. $S_{L,L}$ and $S_{R,R}$ are the direct harmonics, where the electron leaves and returns to the same center, whereas $S_{L,R}$ and $S_{R,L}$ are the exchange harmonics, where the electron leaves from one center and returns to the other. 41

5.1 Contribution of different processes to the high-harmonic spectra, as functions of the alignment angle θ_L, for an N_2 molecule subject to a linearly polarized laser field of frequency $\omega = 0.057$ a.u. and intensity $I = 4 \times 10^{14} W cm^{-2}$. We chose $\phi_p = 0$ so that the $1\pi_{uy}$ orbital does not contribute. The dipole matrix elements have been computed using a gaussian basis set and coefficients from GAMESS-UK [13]. The orbital energies are, $E_{3\sigma_g} = 0.63485797$ a.u and $E_{1\pi_u} = 0.65087981$ a.u. and the internuclear distance is $R = 2.068$ a.u. Panel (a): coherent sum $|M_{\sigma\sigma} + M_{\pi_x\pi_x}|^2$; panel (b): incoherent sum $|M_{\sigma\sigma}|^2 + |M_{\pi_x\pi_x}|^2$; panel (c): Processes involving the $3\sigma_g$ orbital, i.e., $|M_{\sigma\sigma}|^2$; panel (d): processes involving the $1\pi_{ux}$ orbital, i.e., $|M_{\pi_x\pi_x}|^2$. In order to facilitate a comparison with the next figure, the transition amplitudes have not been multiplied by a factor two to account for the two active electron and to ease comparison with the next figure, which considers three active electrons. 49

5.2 Contribution of different processes to the high-harmonic spectra, as functions of the alignment angle θ_L, for the same field parameters in the previous figure. We are considering a three-dimensional scenario, in which the azimuthal angular variable has been integrated over. The dipole matrix elements have been computed using a Gaussian basis set and GAMESS-UK [13]. In this case, $E_{3\sigma_g} = 0.63485797$ a.u, $E_{1\pi_u} = 0.65087981$ a.u. and $R = 2.068$ a.u. Panel (a): coherent sum $|M_{\sigma\sigma} + M_{\pi_x\pi_x} + M_{\pi_y\pi_y}|^2$; panel (b): processes involving the only $1\pi_u$ orbitals, i.e., $|M_{\pi_x\pi_x} + M_{\pi_y\pi_y}|^2$; panel (c): Processes involving the $3\sigma_g$ orbital, i.e., $|M_{\sigma\sigma}|^2$; panel (d): incoherent sum $|M_{\sigma\sigma}|^2 + |M_{\pi_x\pi_x}|^2 + |M_{\pi_y\pi_y}|^2$. In order to facilitate a comparison with the previous figure, the transition amplitudes have not been multiplied by a factor 3 to account for the three active electrons. 51

6.1 Highest occupied molecular orbitals for CO (panels (a) and (c)) and N2 (panels (b) and (d)), in the position and momentum space (upper and lower panels, respectively). The absolute value of the momentum space wavefunctions of the HOMO is taken. The internuclear separation for CO is taken as R=2.1283 a.u. and for N_2 as R=2.068 a.u., and the internuclear axis is along the z-axis. The orbitals are constructed using the LCAO procedure detailed in Sec. 4.2 and coefficients from GAMESS-UK [13] 59

6.2 Schematic representation of atomic orbital contributions to bound molecular orbitals of N_2. The molecular orbitals are the position space wavefunctions, constructed using the LCAO procedure in the same way as the previous figure. The lines connecting the atomic and molecular orbitals symbolise the contribution of the former to the latter. 60

6.3 Schematic representation of atomic orbital contributions to bound molecular orbitals of CO. The molecular orbitals are presented in the position space representation. The figure demonstrates the relative difference in energy of the C and O atomic orbitals. As in previous figures, the LCAO procedure has been used with coefficients found from GAMESS-UK [13]. 61

6.4 Harmonic spectra for N_2 subject to a linearly polarized laser field of frequency $\omega = 0.057$ a.u. and intensity $I = 4 \times 10^{14} W cm^{-2}$. We display the harmonic spectra calculated using the length form, with the multi-electron corrections incorporated, and the harmonic spectra considering the corrections alone, a) and c), respectively. The harmonic spectra calculated using the velocity form, with the multi-electron corrections included, and from the corrections alone, are presented in panels b) and d), respectively. The angle θ_L is the angle between the internuclear axis and the laser field polarization. 62

6.5 High-order harmonic spectra for N_2 in a driving field with the same parameters as in the previous figure, and an alignment angle $\theta_L = \pi/4$. The figure shows the overall spectra together with the first-order corrections taking into account only the direct or both the direct and overlap integrals. We consider both the ionization and recombination prefactors, or the recombination prefactor only (orange and red lines in the figure). Panels (a) and (b) give the velocity and length forms of the dipole operator, respectively. 63

6.6 Harmonic spectra for CO with the same laser parameters as in Fig. 5.1. Presented are the harmonic spectra calculated using the length form, with the multi-electron corrections incorporated, and the harmonic spectra considering the corrections alone, a) and c), respectively. We also present the harmonic spectra calculated using the velocity form, with the multi-electron corrections included, and from the corrections alone, panels b) and d), respectively. 64

6.7 Contributions of the first order corrections to the 45th harmonic versus orientation angle θ_L for N_2 in the length and velocity form, a) and b), respectively, and CO in the length and velocity forms, c) and d), respectively. The two-center interference is labelled by the green arrows. The thick black line represents the contributions of the σ orbitals and the orange stars the contribution of the π orbital. 65

7.1 Harmonic spectrum as a function of alignment angle from an N_2^+ molecule prepared in a coherent superposition of the $3\sigma_g$ HOMO and $1\pi_g$ LUMO, subject to a linearly polarized laser field of frequency $\omega = 0.057$ a.u. and intensity $I = 4 \times 10^{14} Wcm^{-2}$. The energies of the orbitals are $E_{3\sigma_g} = 1.12657012$ a.u. and $E_{1\pi_g} = 0.26871290$ a.u., respectively, with the internuclear distance taken as R=2.113 a.u. The results presented are for a two-dimensional calculation such that the $1\pi_{uy}$ orbital is neglected. a) Coherent sum of all contributions to the harmonic spectrum $\left|M_{3\sigma_g 3\sigma_g} + M_{1\pi_{gx} 1\pi_{gx}} + M_{1\pi_{gx} 3\sigma_g} + M_{3\sigma_g 1\pi_{gx}}\right|^2$, b) Contributions finishing at the $3\sigma_g$ orbital $\left|M_{3\sigma_g 3\sigma_g} + M_{3\sigma_g 1\pi_{gx}}\right|^2$, c) Contributions finishing at the $1\pi_g$ orbital$\left|M_{1\pi_{gx} 1\pi_{gx}} + M_{1\pi_{gx} 3\sigma_g}\right|^2$, d) Contributions starting at the $3\sigma_g$ orbital$\left|M_{3\sigma_g 3\sigma_g} + M_{1\pi_{gx} 3\sigma_g}\right|^2$, e) Contributions starting from the $1\pi_{gx}$ orbital $\left|M_{1\pi_{gx} 1\pi_{gx}} + M_{3\sigma_g 1\pi_{gx}}\right|^2$ and f) Considering the HOMO only $\left|M_{3\sigma_g 3\sigma_g}\right|^2$ 70

7.2 Harmonic spectrum from an N_2^+ molecule prepared in a coherent superposition of the $3\sigma_g$ HOMO and the degenerate $1\pi_{gx}$ and $1\pi_{gy}$ LUMO. The orbital energies are $|E_{3\sigma_g}| = 1.12657012$ a.u. and $|E_{1\pi_g}| = 0.26871290$ a.u., respectively, and an internuclear distance of R=2.113 a.u. is taken. a) Coherent sum of all contributions to the harmonic spectrum as a function of alignment angle, where the full three-dimensional calculation has been performed. b) Spectra for alignment and $\theta_L = \pi/3$ in where the signal has been calculated in 3D (black line), 2D (orange line) and reduced 2D (dashed line)[1]. For more details see text. 72

8.1 Position space wavefunctions of a) Be_2, b) LiB, c) O_2 and d) NF. The orbital wavefunstions are $2\sigma_u$, 4σ, $1\pi_g$ and 2π, respectively, with internuclear distances R^{Be_2}=4.642 a.u. R^{LiB}=4.642 a.u. R^{O_2}=2.280 a.u. and R^{NF}=2.485 a.u.. On the right hand side the direction of the static dipole moment is marked. Considering the HOMO only this is $d_{LiB}^{(HOMO)}$=0.9461 a.u. for LiB and $d_{NF}^{(HOMO)}$=0.1164 a.u. for NF 75

8.2 Absolute momentum space wavefunctions of a) Be_2, b) LiB, c) O_2 and d) NF. All other parameters are the same as those in the previous figure. 76

8.3 Harmonic spectra calculated using the HOMO of a) O_2, b) NF, c) Be_2 and d) LiB using a linearly polarized continuous wave laser field of frequency $\omega = 0.057$ a.u. and intensity I=$4 \times 10^{14} Wcm^{-2}$, as a function of the orientation angle, θ_L. The orbital energis are $E_{1\pi_g}$=0.2446 a.u., $E_{2\pi}$=0.2246 a.u., $E_{2\sigma_u}$=0.2390 a.u. and $E_{4\sigma}$=0.1942 a.u., respectively. . 77
8.4 Harmonic spectra for Be_2 and LiB considering s-type atomic orbitals, a) and c) respectively, and p-type orbitals, b) and d) respectively, using the same laser and molecular parameters as in the previous figure. 80
8.5 Contributions of the s, p and all atomic orbitals to the yield of the 25th harmonic of a) Be2 and b) LiB as functions of the orientation angle θ_L. All parameters are the same as in the previous figure. 80
8.6 Comparison of the harmonics calcualted where the molecular structure is incorporated into the prefactors, and where the molecular structure is incorporated into the action, for N_2 and NF, displayed in a) and b) respectively. We consider the intensity of the 25th harmonic versus the orientation angle. The laser and molecular parameters are the same as those in the previous figure. 82

9.1 Figure representing the evolution of the coherent state basis. A wavefunction at time $t = 0$, $\Psi(0)$, is constructed from the coherent states with position and momentum $q_i(0)$ and $p_i(0)$ and with an initial coefficient $C_i(0)$. The coherent state basis moves along classical trajectories, governed by Hamilton's equations, with positions $q_i(t)$ and momentum $p_i(t)$ and enables us to construct a wavefunction at time t with a coefficient $C_i(t)e^{iS/\hbar}$. From reference [15] 88
9.2 Harmonic spectra from a sample of CCS trajectories distributed at the quiver distance using the acceleration form of the dipole operator with an electric field with a maximum strength of $E_0 = 0.5$ a.u. and frequency $\omega = 0.05$ a.u.. We consider a trapezium shaped pulse with one cycle ramp up, one cycle ramp down and three cycles of constant intensity. 92
9.3 Comparison of the acceleration form of the dipole operator including the off diagonal terms and neglecting them, a) and b), respectively, and the harmonic spectra calculated using the dipole acceleration with and without off diagonal terms, c) and d), respectively. We consider a laser pulse with the same parameters as the previous figure. 93
9.4 The dipole moment and corresponding harmonic spectrum in the length form, a) and b), respectively, the acceleration form, c) and d) respectively, and the velocity form, e) and f) respectively. The laser field has a strength of $E_0 = 0.1$ a.u. and $\omega = 0.0378$ a.u., and a pulse shape the same as that in previous figures. 94

List of Tables

5.1 Weights $\mathcal{W}(\alpha, \beta, i, \nu)$, corresponding to Eq. (5.25), where the azimuthal the azimuthal angle ϕ_k has been integrated over. 48

6.1 Coefficients $\Xi_{\xi'\xi}(l_\alpha, l_\beta)$ found in Eq. (6.12) for the four possible values of the indices ξ', ξ related to the right and left ions. 55

Chapter 1

Overview

This thesis brings together molecular physics and strong field physics using trajectory based approaches to model the physical phenomenon of high harmonic generation (HHG). This is a non-linear process in which an atom or molecule is exposed to a strong laser field, of intensity greater than $10^{13} W cm^{-2}$, and results in a spectrum of harmonics, which are integer multiples of the driving laser field.

The interaction of light with matter is a prominent area of modern physics which dates back to Hertz's realization, in 1886, that light could influence matter. The ability to generate coherent light, following the invention of the maser in 1953 [16], allowed matter to be understood with much greater precision by probing particular energy levels. This possibility arose from Einstein's proposal of the existence of photons in 1917 [17] and the description of light matter interaction through perturbation theory. Initially, the available laser intensity was limited by the gain medium, but the development of chirped pulse amplification [18], in 1985, allowed higher intensity laser light to be produced. Nowadays, laser light of intensities beyond $10^{18} W cm^{-2}$ are possible from table top laser systems.

At such high intensities, a wealth of phenomena arise which are no longer well described by a perturbative description of laser matter interaction. This is because the laser field is of a similar strength to the atomic binding force. Such phenomena include above threshold ionization (ATI) and high harmonic generation (HHG). In addition, at intensities of $10^{18} W cm^{-2}$ and above, relativistic effects become important because the energy transfered to the system is of the order of the rest mass of the electron.

Early on, HHG was recognised to be of practical importance because of its potential as a coherent source of extreme ultraviolet (XUV) and x-ray radiation. More recently, it

has led to an exciting, and a rapidly evolving, scientific field known as 'Attosecond Science'. This is because the physical mechanism behind HHG takes place on a timescale of attoseconds (atto=10^{-18}), which is a timescale of an order comparable to electron rearrangement in a chemical reaction. For example, the atomic unit (a.u.) of time is 0.00243 femtoseconds (femto=10^{-15}). Thanks to great theoretical and experimental efforts, HHG has consequently become an important practical tool for generating extreme ultraviolet (XUV) attosecond pulses [8, 19, 20] and attosecond tomographic imaging of molecular orbitals [7, 9, 21].

From a theorist's viewpoint, when modelling such phenomena, a full solution to the time-dependent Schroödinger equation (TDSE) is desirable. However, there is no exact analytical solution of the TDSE, even for a single electron atomic system in a strong laser field. Numerical solutions are available but only up to two active electrons [22]. Many of the early simulations therefore resorted to modelling HHG within a single active electron (SAE) approximation, which proved to be quite an accurate approximation and reproduced the most important features of the phenomenon. However, recent experiments [9, 23] have demonstrated the importance of multi-electron effects in HHG. Many theoretical efforts have demonstrated the limits to the validity of the SAE approximation [1, 24–26] and the importance of multi-electron effects. Much of the work in this area is highly numerical, using approximate techniques borrowed from quantum chemistry.

In this thesis we approach the problem from a much more analytical perspective. Mainly, the methods presented are extensions to the workhorse of strong field physics, the strong-field approximation (SFA). In addition, we apply the coupled coherent state (CCS) approach to HHG. This has the main benefit over existing numerical approaches in that it is a trajectory based approach, which allows easier comparison to the SFA and facilitates a fresh interpretation of the physics behing the generation of high harmonic light. Also, it fully includes the Coulomb potential, which in the SFA is neglected in certain parts of the computation, a sacrifice which is made to simplify the problem.

We also use the SFA to study the effects of molecular orbital geometry on HHG spectra. The influence of molecular structure is imprinted on the harmonic spectrum [1, 3, 9, 23, 27]. Therefore predicting what features one might expect from performing a HHG experiment with a system exhibiting a specific type of molecular orbital extends the applicability of HHG to molecular imaging.

High harmonic generation can be well understood using semi-classical models, such that much of the important physics may be understood in terms of classical electron trajectories. However, quantum interference is an inherent part of HHG. Even in Hydrogenic, single electron, systems, interference occurs between different possible trajectories along

which the electron may return. In diatomic systems there is also two-center interference arising from electron recombination to the spatially separated atomic centers. In addition, for systems with more than a single active bound state, interference may occur between processes coupling different bound states. In this work, all three types of quantum interference are discussed, and their influence on the harmonic spectrum examined.

This thesis focuses on trajectory based approaches to high-order harmonic generation. In Chapter 2 the main issues and challenges within the field are reviewed. In Chapter 3 the most common theoretical approaches used to model HHG are presented. Chapter 4 details the workhorse of strong field physics, the strong-field approximation (SFA) and its extension to diatomic molecules. Chapter 5, Chapter 6 and Chapter 7 deal with approaches we have developed to expand the traditional SFA beyond the SAE approximation for diatomic systems. In Chapter 8 we focus on the effects that particular features in a molecular electron orbital have on the harmonic spectrum, with a particular emphasis on heteronuclear diatomic systems. Chapter 9 will look at coupled coherent state (CCS) approach and apply it to obtain harmonic spectra from single electron Hydrogenic systems. Finally, in Chapter 10 we summarise our main findings and conclusions.

The appendices provide material of either a complementary or technical nature. In Appendix A we list the abbreviations most commonly used in this field and this thesis. Appendix B defines the atomic units used throughout this work. An explanation of different gauge formulations of the Hamiltonian is provided in Appendix C. Some of the integrations required for Chapter 6 are provided in Appendix E, which contains expressions for the overlap integrals and Appendix D, which contains integrations for the three-dimensional model. A derivation of the approach in Chapter 6 is presented in Appendix F. Appendix G provides some important derivations of some of the expressions we use when calculating harmonic spectra with the CCS approach.

Chapter 2

Introduction

2.1 Historical overview

The first observations of high-oder harmonic generation (HHG) [28, 29] and above-threshold ionization (ATI) [30] were in the late 1980s and followed earlier work on multi-photon ionization in intense fields [31]. These early experiments found that multi-electron rare gas atoms interacting with intense infra-red fields ($I \geq 10^{13} W cm^{-2}$) gave rise to spectrum of harmonics. The harmonics were odd multiples of the driving laser frequency, and were of similar intensity to each other with increasing harmonic order, a feature known as the 'plateau'. This region of similar intensity was followed by an abrupt decrease in harmonic intensity after a certain harmonic order, which is called the 'cutoff'. Such observations were counterintuitive to the monotonic decrease in harmonic intensity with harmonic order, which one would intuitively expect from perturbation theory. The specific features of a harmonic spectrum are illustrated in Fig. 2.1 a). Similar observations were made for ATI photo-electron spectra, a process where more photons than required for ionization to take place are absorbed.

These highly non-linear phenomena may be understood as the outcome of laser-induced rescattering or recombination [32]. For HHG this consists of three consecutive steps of ionization of the target system, propagation of the ionized electron in the laser field and finally recombination of the electron to the system from which ionization occurred, as illustrated in Fig. 2.2. The figure shows that the Coulomb potential is deformed by the laser field, which allows the electron to tunnel through the potential barrier. In principle, if the field is intense enough the electron may also escape over the barrier. The three step model (TSM), as it is known, is also applicable to above-threshold ionization, where after ionization the electron either leaves the vicinity of the atom and travels to the detector, or rescatters elastically with its parent ion, and non-sequential double

ionization (NSDI), where, when the electron returns to the atom, an inelastic ionization event occurs, releasing two electrons into the continuum [33, 34]. In addition, the TSM may also be modified to incorporate other important physical phenomena occurring in strong fields, such as recollission excitation followed by subsequent tunnelling [4, 35, 36], which is a rescattering mechanism in NSDI.

The recollision model of HHG interprets the energy of an emitted harmonic to be the combined energy of the recombining electron and the ionization potential of the bound state to which it is recombining to. This simple interpretation also can be used to obtain good predictions of the cutoff in the harmonic spectrum, which is determined by the maximum possible energy that the recombining electron may have acquired from the field. Most of the modern applications of HHG are understood within this framework.

Several years after the experimental observation of HHG, the imaging applications of this phenomena were recognised. These include tomographic reconstruction of the highest occupied molecular orbital (HOMO) of diatomic molecules [7, 21] using the harmonic spectra, imaging of orbitals lying energetically below the HOMO [23, 37, 38] and real time imaging of electron-hole dynamics [9]. This latter issue is related to the fact that, by removing an electron under the influence of the field, a hole is created in the core, which will evolve on a sub femtosecond timescale. The experimentally reconstructed HOMO and real time electron hole dynamics are displayed in Fig. 2.1 b) and d). In the case of ATI, photo-electron holographic imaging of rare gases is possible using velocity-map imaging techniques [10, 39]. These dynamic imaging possibilities arise from the sub cycle dynamics of the propagating electron and the width of the returning wavepacket, which allows matter to be probed with attosecond (10^{-18}) temporal resolution, and angstrom (10^{-10}) spatial resolution, respectively.

In some senses the three step mechanism is similar to the pump-probe experiments used very successfully in femtochemistry, which, for example, allowed intermediate states of a chemical reaction to be imaged. There is a vast literature for the topic of femtochemistry (see for example [40]), for which the Nobel Prize was awarded to Ahmed Zewail in 1999. However, for electron and electron hole dynamics to be observed pulses with a duration less than a femtosecond are required. This is due to the atomic unit of time being of the order of attoseconds. Rather than use shorter laser pulses one may use the physical mechanism behind the HHG process to image matter. The 'self-probing' of a molecular species, where the recombination of the electron wavepacket is seen as the probe in a pump probe type experiment has recently been utilised, for example, to model electron core dynamics in a molecule [9], and also to record molecular dynamics in H_2 and methane [41, 42].

FIGURE 2.1: Some of the main results resulting from the HHG mechanism. a) An early harmonic spectrum from atomic Ar in an Nd:YAG laser. From reference [6]. b) A tomographic reconstruction of the HOMO of N_2. From reference [7]. c) Kinetic energy spectra of electrons detached from a neon atom versus the delay between the attosecond pulse and the strong femtosecond pulse. From reference [8]. d) Hole dynamics measured using the harmonic spectrum in CO_2: 1) initial hole density 2) shape after a quarter period 3) after a half period. From reference [9]

This approach to molecular imaging, known as high harmonic spectroscopy, utilizes the fact that each harmonic in the spectrum corresponds to a particular return time of the previously ionized electron. This can be seen in Fig. 2.3, which demonstrates that each harmonic energy has two contributions, the so called long and short trajectories. If only the short trajectories are selected, each harmonic is generated at a very specific time interval, implying that each harmonic is a snapshot of the system at a particular time. In other words, the harmonic spectrum encodes temporal information about the target system. For a typically HHG experiment, the driving laser pulse is of femtosecond duration and wavelength of $800nm$, which corresponds approximately to a period of $2.7fs$. The sub-cycle electron dynamics, which corresponds to the time between ionization and recombination, are thus on the attosecond timescale.

FIGURE 2.2: Illustration of the three step process for a system of ionization potential I_p. The steps are 1) tunnelling ionization from the Coulomb potential which has been deformed by the strong laser field 2) acceleration of the electron by the laser field 3) recombination with the core leading to the generation of a high-energy photon. From reference [10].

FIGURE 2.3: Ionization and recombination times during the laser field cycle for a given harmonic. The right hand panel shows a cosine laser field of wavelength $\lambda = 800nm$ and intensity $1.2 \times 10^{14} W cm^{-2}$. The left panel depicts the times of ionization and recombination for a given energy of recollision. The dashed line corresponds to long trajectories and the solid line to short trajectories. From reference [11].

Not only does HHG enable access to attosecond system dynamics, but it also allows angstrom spatial resolution. This is due to the de Broglie wavelength of the returning electron. If such resolution was required using photons the energy would have to be very high, that is, in the X-ray regime. Such high energy photons are likely to probe deeper into the atomic or molecular species, which is unsuitable for most chemical reactions in which rearrangement occurs in valence shells. In high harmonic spectroscopy, on the other hand, the energy of the recombining wavepacket can be relatively low to achieve angstrom spatial resolution. This makes HHG a novel, tabletop technique, for molecular imaging. It could benefit many scientific fields where electron dynamics are important, including, but not limited to, physics, chemistry and biology.

The highest energy harmoncis, which in Fig. 2.3 are around $23eV$, have only one contributing solution, which implies that the highest order harmonics are emitted at a very specific time in the field cycle. Consequently, HHG may also be used as a mechanism to create isolated attosecond pulses of XUV radiation [43]. Such attosecond bursts have allowed, for example, the complete characterization of femtosecond laser pulses [8, 19, 20], the measurement of atomic processes on an attosecond timescale, for example, the ejection of an Auger electron from Krypton atoms [44], and tunnelling dynamics [45]. In Fig. 2.1 c) a kinetic energy spectrum versus the time delay between a attosecond pulse and a femtosecond strong laser field is presented. This allows the femtosecond pulse to be fully characterised.

HHG is a non-perturbative phenomenon because the force exerted on the electron by the high intensity driving laser field is comparable to the Coulomb force exerted by the target system. Therefore, it is not possible to use perturbation theory to model strong field phenomena. Many other theoretical approaches and approximations are regularly employed by the strong field community when modelling HHG. The strong field approximation (SFA) [46] has facilitated theoretical calculations on atoms and molecules (see, for example [1, 27, 47–49]) to be carried out analytically to a great extent. This approximation assumes that, during the propagation step of the three step model, the electron does not feel the binding potential of the residual core and that the field does not influence the core when the electron is bound. In addition, the recolliding electron wavepacket is assumed to be a plane wave. This is often a good approximation because the electron travels a large distance from the atom or molecule during its propagation in the field.

Another widely used approximation is the single active electron (SAE) approximation, which assumes that only the least bound electron contributes to the physics of the phenomenon. Several other approximations are also made. For example, it is often assumed that the ground state does not become depleted, that continuum-continuum transitions

are neglected, that the single atom response is sufficient to understand the HHG phenomenion and that the core does not evolve while the electron is in the continuum. Although many of these approximations are often valid, depending on the particular experiment, they often break down.

Throughout this work the single atom or molecule response to the strong laser field is discussed. However, we recognise that in a HHG experiment, where there is a large number of atoms or molecules, harmonics produced at each atom or molecule must be phase matched. In other words, that for a strong harmonic signal each contribution must add coherently. The phase of a harmonic is dependent on the laser intensity [50]. Therefore, in a gaussian profile laser beam, harmonics emitted from different regions may have different phases. The propagation of the harmonic in the medium may also have a strong effect on the overall harmonic signal.

In what follows we will now elaborate on some of the most important issues and recent developments in high harmonic generation.

2.2 Multi-electron effects and orbital symmetry

The single active electron approximation is often applicable to many electron atoms and simple molecules, and has worked very well in modelling early experimental data. This is because electrons more deeply bound than the least bound electron in an atom, or highest occupied molecular orbital (HOMO) in a molecule have a very low probability of ionization, and, consequently, are expected not to contribute significantly to the HHG process. However, harmonic generation experiments have been performed on systems of increasing complexity, ranging from diatomic molecules [51] to hydrocarbons [52], to surfaces [53, 54], where SAE, single orbital approximations are likely to break down. Even in relatively simple diatomic molecular systems, which are the focus of this work, there is a wealth of phenomena resulting from the effect of many electrons and multiple orbitals which cannot be explained within these approximations.

Since the beginning of this century it has become experimentally possible to align an ensemble of molecules with a low intensity picosecond 'pump' pulse, prior to an intense 'probe' femto-second laser pulse, which generates the high harmonic radiation [55–57]. This capability enables harmonic generation to be performed for arbitrary angles between the laser field polarization and the internuclear axis of a diatomic molecule and has led to important observations in the study of multi-electron effects. There are two important questions which must be considered when modelling HHG for many electron diatomic systems

- What is the effect of lower lying orbitals when performing a HHG experiment on diatomic molecules?
- How does orbital geometry and symmetry influence the strength of the harmonic yield?

The molecular orbital geometry of a diatomic molecular orbital will have a strong influence on the harmonic spectrum. This is especially true for such features as nodal planes, which are regions of vanishing probability density in the molecular wavefunction. Let us assume that the molecular orbital from which the active electron tunnels has a nodal plane along the internuclear axis. If this axis is aligned parallel to the laser-field polarization, the probability density will be vanishing at the geometric center of the molecule. This leads to the harmonic signal being strongly suppressed for parallel alignment in this instance. The issue has been extensively explored in the construction and interpretation of photoionization angular-dependent maps, which are based on the fact that the tunnel ionization probability is highly influenced by the molecular alignment angle [58–60]. Since ionization is inherent in the HHG process, one would expect a similar suppression in the harmonic signal. Such a suppression has indeed been identified in HHG spectra [2, 9, 23, 27]

The issue of molecular geometry is also linked to the observation of multiple orbital contributions in HHG. For example, in N_2, the HOMO has geometry such that the electron density is distributed along the internuclear axis. This results in a greater ionization rate when the molecule is aligned parallel to the field polarization direction compared to when it is aligned perpendicular to the field. However, the HOMO-1, which is the first molecular orbital that lies energetically below the HOMO, has a nodal plane along the internuclear axis, and therefore ionization from this orbital is greatest when the internuclear axis is aligned perpendicular to the driving field polarization [58, 61]. As the HOMO-1 in this specific instance lies energetically only a few electron volts below the HOMO and has the opposite ionization behaviour to the HOMO, it is not a good approximation to neglect it. Observation of the opposite behaviour of harmonic yield versus alignment angle to that expected from the HOMO [23] which in this case means increased harmonic yield for perpendicular alignment, indicates the influence of the HOMO-1. These effects, previously attributed to the depletion of the ground state [62, 63], are exploited in obtaining geometric and dynamic information from multiple orbitals in a HHG experiment [9].

The effect of orbital symmetry can be described well and intuitively using the SFA [1, 27, 48, 49]. However, the effect of multiple orbitals has only been incorporated into the SFA in a few cases [1, 2, 64, 65] and approximate numerical solutions are often

beneficial as a benchmark to analytical techniques. For example, the importance of lower lying orbitals have been observed using time dependent density functional theory (TDDFT) [25, 66, 67].

In addition to the influence of molecular orbitals lying energetically below the HOMO contributing to the harmonic spectra, one must also consider a) electron exchange between the continuum electron and the residual core [2, 64, 65] b), multi-electron polarization of the neutral molecule and the ion [24, 26], c) laser induced excitation of the core during the propagation of the electron in the continuum [24, 68] and d) excitation of the core during recombination [68]. Apart from a), which corrects the traditional SFA semi-analytically, these studies use the approximate numerical approach, multi-configurational time dependent Hartree (MCTDH) theory. This is because incorporating multi-electron effects into the SFA is extremely challenging and fully numerical solutions for all but single electron diatomic systems are currently impossible. For the diatomic systems of interest, such as N_2 or CO_2, the number of degrees of freedom are prohibitive even to MCTDHF methods so the less accurate TDDFT or frozen core approximations must be made, which neglect all or part of the electron exchange or correlation.

In this work we will use the SFA to model the effects of orbital symmetry on the harmonic spectrum and extend the standard SFA to look at the influence of lower lying orbitals and multi-electron effects. The issues of multi-electron, multi-orbital effects are addressed specifically in Chapter 5, Chapter 6 and Chapter 7. The influence of orbital geometry and nodal structures on the harmonic spectrum are also addressed in these Chapters as well as in Chapter 8.

2.3 Two-centre interference

The capability to align an ensemble of molecules with a low intensity laser pulse prior to performing harmonic generation spectroscopy results in two-center, angular dependent interference in the harmonic spectra. Such interference minima were predicted theoretically for photo-electron spectra from H_2^+ in the 1960s [69]. The first theoretical calculations for harmonic generation from H_2^+ at arbitrary alignment angles [57, 70, 71] predicted an angle dependent minimum in the harmonic spectrum which was accompanied by a phase jump in the emitted harmonics, suggesting that this phenomena was an interference effect. The physical interpretation of this phenomenon was that the interference arose from the electron wavepacket recolliding with two spatially separated centers. It should be noted that the interference is not due to harmonic light emitted from spatially separated centers. This is because the wavelength of the harmonics are much higher than the typical internuclear distance of a diatomic wavefunction, such

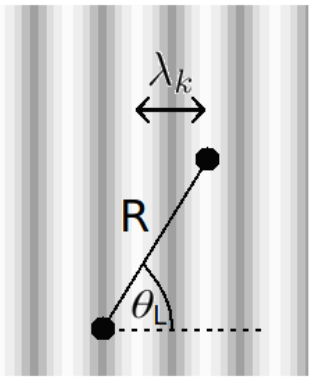

FIGURE 2.4: Schematic representation of destructive two-center interference occurring when a plane wave of wavelength λ_k collides with a diatomic molecule of internuclear separation, R, aligned at an angle θ_L, relative to the linearly polarized laser field.

that interference is not to be expected, whereas the wavelength of the returning electron wavepacket is of a similar order to the internuclear separation.

For a one- or two-electron diatomic molecule of internuclear separation R and with a symmetric wavefunction constructed of s-type atomic orbitals, two centre interference minima are expected for,

$$R\cos(\theta_L) = (2n+1)\frac{\lambda_k}{2}, \tag{2.1}$$

and maxima for,

$$R\cos(\theta_L) = n\lambda_k, \tag{2.2}$$

where θ_L is the alignment angle between the internuclear axis and the laser field polarization and $\lambda_k = \frac{2\pi}{k}$ is the de Broglie wavelength of the returning electron wavepacket, as displayed in Fig. 2.4. Given that the recollision model predicts that the frequency of a harmonic, emitted after a wavepacket of energy E_λ recombines with a system of ionization potential I_p, will be equal to,

$$\Omega = I_p + E_\lambda, \tag{2.3}$$

one would expect interference minima to occur at a harmonic frequency,

$$\Omega = \frac{\pi^2}{2R^2\cos^2(\theta_L)} + I_p, \tag{2.4}$$

and maxima at

$$\Omega = \frac{2\pi^2}{R^2\cos^2(\theta_L)} + I_p. \tag{2.5}$$

Although this intuitive picture seemed to be in agreement with numerical simulations for H_2^+, discrepancies from this interference condition were observed when measuring

the interference minima in experiments. It was found that the harmonic at which the interference minimum occurred was dependent on the driving laser intensity, contrary to what is predicted by Eq. (2.4) and Eq. (2.5). In fact, in the experiment [72] the frequency at which the minimum occurred was well predicted by Eq. (2.3), whereas in [73], it was found that interference minimum occurred at the harmonic frequency,

$$\Omega = E_\lambda \tag{2.6}$$

Possible reasons for such a discrepancy include that the above mentioned experiments were conducted on CO_2, which has a HOMO that consists of both s-type and p-type atomic orbitals, unlike that of H_2^+, which contains only s-type orbitals. This difference will cause the interference minima to deviate from the simple intuitive picture described above [74]. Nonetheless, the simple interference condition can be extended to fully account for orbital symmetry and the presence of p-type atomic orbitals, within the framework of the SFA [27, 47, 75, 76], which is also presented in this work, and generalized for heteronculear molecules [3, 77, 78]. A discussion may be found in Chapter 4.

A distinction must also be drawn between the so called static minimum, described above, which is determined by the shape of the molecular orbital the returning electron wave packet interacts with, which is assumed to be static, and dynamic minimum. The importance of sub-cycle evolution of the HOMO was highlighted as one of the reasons for discrepancies from the simple interference condition [9]. In addition to this, the contribution of orbitals lying energetically below the HOMO, which in many studies had been assumed to be negligible, as discussed in Sec. 2.2, were found to be extremely important. The HOMO-1 is especially prominent near to the harmonic cutoff, because it has a higher ionization potential than the HOMO, and thus recombination will give rise to a higher energy photon. To understand the minimum from a dynamic perspective, the phase from ionization, propagation and recombination of the electron, as well as the phase accumulated by the residual core, must be accounted for. Based on this analysis, the harmonic at which the interference minima occurred scaled linearly with the driving laser intensity, in stark contrast to the situation predicted by the simple interference condition.

Interestingly, even in numerical simulations of H_2^+ the minimum was intensity dependent [79], suggesting the influence of excited states and the Coulomb potential. The relationship between static and dynamic interference was investigated within the context of excited states in H_2 where the phase between the ionic ground state and excited state shifted the predicted minima from those expected to arise from structural interference if

such excited states were energetically close enough to the ground state [80]. The phase depends on the initial position of the electron wavepacket and is intensity dependent.

The interference minimum is, of course, strongly dependent on internuclear distance, which for H_2 is expected to vary on the timescale of the three step model. This has been investigated experimentally [41, 42], and it has been shown that the nuclear dynamics of H_2 shifts the two-center minima to comparatively lower harmonic orders. For larger diatomic molecules, however, it has been demonstrated theoretically that vibrational nuclear dynamics are negligible [81], such that the Born-Oppenheimer approximation is applicable. The Born-Oppenheimer approximation assumes that the electronic motion and the nuclear motion can be decoupled, because the nuclear motion occurs on a much longer timescale to that of the electronic motion. In the context of modelling diatomic species in strong fields this allows the vibrational motion of the nuclei to be neglected.

In this thesis we will examine two-center interference in a static framework in diatomic homonuclear and heteronuclear molecules. The generalised two-center interference condition, which accounts for s-p mixing, and is derived in [27], is presented in Chapter 4. We discuss two-center interference in the harmonic spectrum in Chapter 5, Chapter 6, Chapter 7 and Chapter 8.

2.4 Coulomb effects

Even in atomic hydrogen the effect of the Coulomb potential has been shown to be important in some strong field phenomena, such as the observation of the 'ionization surprise' in the lower energy region of strong field ionization spectra [82, 83]. This is a spike like structure in the low energy region of the photo-electron energy distribution, which appears when using mid-infrared laser frequencies. The feature is not predicted by the SFA or the Keldysh tunneling theory, although it is well produced by solving the time-dependent Schrödinger equation (TDSE) numerically. It was shown later that this result could be well reproduced using a Coulomb corrected SFA [84] in which the effect of the Coulomb potential on the electron is included, indicating not only the importance of the Coulomb potential but also a clear physical interpretation with quantum orbits. When modelling larger systems in strong fields the effects of the Coulomb potential, such as Coulomb focussing of the continuum wavepacket, are likely to become even more important. Therefore, theoretical methods are required which provide an intuitive, trajectory based analytical grounding, such as the SFA, but include these important effects. Analytical work in this direction includes corrections to the SFA [85–87], which has proved very challenging, and apart from the exceptional case of [9] have not been

applied to HHG. Other trajectory based approaches, such as the semi-classical Herman-Kluk (HK) [88], which also fully include the Coulomb potential, have only been applied to HHG in a few cases [89, 90].

In this thesis we propose a novel trajectory based method, called the coupled coherent state (CCS) approach, in which the binding potential is fully included throughout the HHG process. This approach is presented in Chapter 9, as well as harmonic spectra obtained using the method.

2.5 Increasing the harmonic cutoff

An important issue in modeling high-order harmonic generation is how to increase the cutoff energy, or in other words, the maximum frequency obtained from the spectrum. Generation of the highest frequency XUV radiation enables the probing of ever shorter timescales [10], and also increases the spatial resolution on which matter can be probed. Hence, high frequency pulses are desirable. The cutoff energy of a harmonic spectrum is proportional to $I\lambda^2$ where I is the intensity of the driving laser field and λ is the wavelength, suggesting that increasing either of these parameters will increase the cutoff.

Increasing the wavelength of the driving laser will increase the electron excursion time in the field, which will cause additional wavepacket spreading, and therefore a reduction in the overall yield. The scaling of the yield with wavelength has been reported in the literature as proportional to λ^{-5} or proportional to λ^{-7} [91, 92]. This can be overcome to some extent by, for example, the use of an additional frequency doubled orthogonally polarized field [93], which, for a $n\pi$ phase difference between the fields, increase the harmonic yield by a factor of two orders of magnitude, or by the addition of a higher order harmonic pulse, which gave rise to an increase of 17 orders of magnitude [94]. Increasing the laser field intensity, on the other hand, gives rise to problems of depletion of the ground state, which will also reduce the overall harmonic yield.

Various attempts at increasing the cutoff have included the proposed mechanism of sequential double ionization followed by nonsequential double recombination [95], the use of two colour fields [94], quantum path optimisation by using an appropriate waveform [96] and, more recently, considering electron recombination to a core hole [97].

In this thesis a mechanism is considered which could potentially be used not only to increase the cutoff but to map the contributions of different molecular orbitals to different regions of the harmonic spectra. This issue is investigated in Chapter 7.

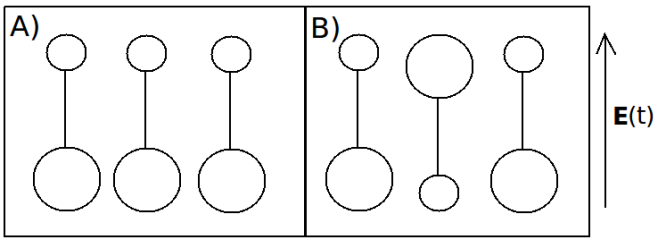

FIGURE 2.5: Schematic representation of a) an oriented sample of heteronuclear molecules and b) an aligned sample of heteronuclear molecules. The arrow on the right hand side of the figure indicates the linearly polarized laser field direction.

2.6 Heteronuclear molecules and orbital symmetry

In recent years, strong field phenomena from heteronuclear molecules has become a research topic of interest theoretically [2, 3, 67, 77, 78, 98–100] and experimentally [101–103]. This has become possible because it has become experimentally feasible to orient polar systems by use of a low intensity femtosecond pulse and a static electric field. We note that the difference between orientation and alignment is that in an oriented system, the direction of the static dipole along the internuclear axis can be specified, over the full 2π possible orientation possibilities. On the other hand, in an aligned sample, the angle between the internuclear axis and the laser field polarization is determined, but not the direction of the dipole moment. Therefore, an aligned sample will be made up of parallel and anti-parallel contributions. This is demonstrated in Fig. 2.5.

Calculation of high order harmonic generation from heteronuclear molecules requires many additional effects to be accounted for. Because the system no longer has a definite symmetry one expects not only odd but also even harmonics to be emitted from the field. The interference minimum one would expect from a homonuclear system is modified and less distinct [3, 100] and the static dipole moment may also give rise to Stark shifts which will shift the interference minimum [77].

In this thesis we compare isoelectronic homonuclear and heteronuclear molecules in strong fields and examine the effect of the static dipole moment on orbital geometry and the resulting harmonic spectrum in Chapter 6 and Chapter 8.

Chapter 3

Theoretical approaches

We now present an overview of some of the most common approaches to calculating the harmonic spectrum from an atom or molecule exposed to an intense laser field, as well as their benefits and shortcommings. These aproaches include full numerical solutions to the time-dependent Schrödinger equation (TDSE), approximate numerical approaches such as the time-dependent density functional theory (TDDFT) and the multi-configurational time-dependent Hartree-Fock (MCTDHF) theory, the strong-field approximation (SFA), which is a widely used semi-classical trajectory based approach, and other semi-classical and classical trajectory based methods.

3.1 Physical framework

For the laser intensities modeled in this work, the electron, during its propagation in the laser field, is non-relativistic. Therefore we can safely ignore relativistic effects. To calculate the wavefunction $\mid \Psi(t)\rangle$, one may solve the time dependent Schrödinger equation (TDSE) which reads

$$i\frac{\partial \mid \Psi(t)\rangle}{\partial t} = H(t) \mid \Psi(t)\rangle, \tag{3.1}$$

with,

$$H(t) = H_0 + H_I(t) \tag{3.2}$$

where for a single electron system,

$$H_0 = \frac{\mathbf{p}^2}{2} + V(\mathbf{r}), \tag{3.3}$$

and

$$H_I(t) = -i\mathbf{A}(\mathbf{r},t)\cdot\nabla + \mathbf{A}(\mathbf{r},t)^2. \tag{3.4}$$

Equation (3.2) is the one-electron Hamiltonian, where $V(\mathbf{r})$ is the Coulombic potential of the sample exposed to the laser field and $\mathbf{A}(\mathbf{r},t)$ is the vector potential of the driving laser field. By employing the dipole approximation, which implies that when the spatial dependence of the field is very large compared to momentum of the returning wavepacket, one may use,

$$e^{i\mathbf{k}\cdot\mathbf{r}} \approx 1, \tag{3.5}$$

which implies that the spacial dependence of the field is neglected. One may then write,

$$\mathbf{E}(t) = \frac{\partial}{\partial t}\mathbf{A}(t), \tag{3.6}$$

where $\mathbf{E}(t)$ is the electric field. By using gauge transformations within the dipole approximation it is possible to rewrite Eq. (3.1) in the velocity gauge

$$i\frac{\partial}{\partial t} \mid \Psi^V(t)\rangle = H^V(t) \mid \Psi^V(t)\rangle, \tag{3.7}$$

where,

$$H^V(t) = \left(H_0 + \mathbf{A}(t)\cdot\mathbf{p}\right), \tag{3.8}$$

or in the length gauge,

$$i\frac{\partial}{\partial t} \mid \Psi^L(t)\rangle = H^L(t) \mid \Psi^L(t)\rangle, \tag{3.9}$$

where,

$$H^L(t) = H_0 + \mathbf{E}(t)\cdot\mathbf{r}. \tag{3.10}$$

Both gauges are equivalent provided that the Schrödinger equation is solved exactly. The gauge invariance is broken if the TDSE is solved by approximate theories. More details about unitary transformations between different gauges, including the Krammers-Hennerberger gauge, which will be used later in this work in deriving the SFA transition amplitude, are presented in Appendix C.

3.2 Forms of the dipole operator

The light emitted by an accelerating charge is proportional to the dipole acceleration. Therefore, to calculate the harmonic spectra, one must calculate the second differential of the expectation value of the dipole moment, given by

$$\mathbf{a}(t) \equiv \ddot{\mathbf{R}}(t) = \frac{\partial^2}{\partial t^2}\mathbf{R}^{(l)}(t), \tag{3.11}$$

where,

$$\mathbf{R}^{(l)}(t) = \langle \Psi(t) \mid \mathbf{r} \mid \Psi(t) \rangle, \tag{3.12}$$

is the expectation value of the dipole in the length form. We then calculate the absolute value of the Fourier transform of the dipole acceleration to obtain the harmonic spectrum in frequency space, in the direction of η,

$$S(\Omega) = |\mathbf{a}(\omega)|^2 \tag{3.13}$$

where

$$\mathbf{a}(\omega) = \frac{1}{\sqrt{2\pi}} \int_{\infty}^{-\infty} e^{i\Omega t} a(t) \hat{e}_\eta \, dt. \tag{3.14}$$

If we consider a laser pulse of length T, starting at time $t = 0$, the integral in Eq. (3.14) can be written as [104],

$$\mathbf{a}(\omega) = \frac{1}{\sqrt{2\pi}} \left(e^{-i\omega T} \dot{\mathbf{R}}^{(l)}(T) + i\omega e^{i\omega T} \mathbf{R}^{(l)}(T) - \omega^2 \int_0^T e^{-i\omega t} \mathbf{R}^{(l)}(t) dt \right). \tag{3.15}$$

We see that the first two terms on the right hand side of Eq. (3.15) depend on the final position and momentum of the electron, and as these terms grow with the length of the simulation, T cannot be taken to infinity. These terms have been identified to give rise to the background noise in a harmonic spectrum in numerical simulations of high harmonic geenration (HHG), and to reduce the intensity of the harmonic peaks [104]. These terms can be neglected and the final term in Eq. (3.15) used alone to calculate the harmonic spectra, which is often the approach used in the literature. For example, in [46] the final term is taken without the ω^2 term. However, a much more elegant approach to calculate an accurate harmonic spectrum is to make use of the Ehrenfest theorem, which, by use of the Heisenberg equation,

$$\frac{\partial A}{\partial t} = \frac{1}{i\hbar}[A, H], \tag{3.16}$$

allows one to express Eq. (3.12) in either the velocity form,

$$\mathbf{R}^{(v)} = \langle \Psi(t) \mid \mathbf{p} \mid \Psi(t) \rangle, \tag{3.17}$$

or the acceleration form

$$\mathbf{R}^{(a)} = -\langle \Psi(t) \mid \nabla V(\mathbf{r}) \mid \Psi(t) \rangle. \tag{3.18}$$

These three formulations are equivalent providing that the wavefunction is an exact solution to the Hermitian Hamiltonian used to describe the system and thus, that all commutation relations hold. In numerical simulations, and especially when employing

the SFA, this is violated in many respects. In numerical applications, for example, an absorbing boundary will violate Hermiticity, and so will discrete approximations of differential operators. In the strong field approximation (SFA), it has been shown, in the context of photo-ionization [105], that the velocity and acceleration forms are the same in the asymptotic limit, although not the length. However, when the ground state wavefunction is approximated by a linear combination of atomic orbitals (LCAO) even in the asymptotic limit velocity and acceleration forms are not the same [48].

Therefore, careful consideration must be made when choosing which form of the dipole operator to use. The acceleration form, Eq. (3.18), is weighted toward contributions from the core, making electron density at the boundaries insignificant, whereas the length form, Eq. (3.12), has the opposite behaviour. This makes the acceleration form more suited for numerical simulations of HHG as it in effect probes the dynamics of the system at the core, which is what one is interested in when considering HHG. The benefits of using the acceleration form can be seen very clearly by comparing the two approaches, because the length form will often result in a less distinct cutoff in the harmonic spectrum, compared to exactly the same calculation in the acceleration form.

Although when solving the time-dependent Schrödinger equation numerically different forms are 'approximately' [48] equivalent, within the SFA the results can be very different. The acceleration form [106, 107], has been recognised to give a better quantitative agreement with a solution of the time-dependent Schrödinger equation compared to the length form. However, it was also pointed out that the velocity form also gives better quantitative agreement than the length form and also has the benefit of being relatively simple to compute, when using the SFA to calculate HHG from diatomic systems [48]. The length form is regarded as being the worst option when using the SFA, as it gives rise to issues of translational variance [108].

Finally, we reiterate the difference between form and gauge. When discussing form we are concerned with how to express the expectation value of the dipole moment, which may be in the length, velocity or acceleration forms, as previously explained. However, gauge determines how the Hamiltonian is written, which may either be in the length, velocity or Krammers-Henneberger gauge.

3.3 Numerical solutions to the time-dependent Schrödinger equation

Where possible, a fully numerical solution to the time-dependent Schrödinder equation (TDSE) is desirable, as this incorporates all time-dependent physical processes, and

can be applied to arbitrary potentials. This approach has been employed since the late 1980s [109, 110]. One of drawbacks is practical, as even for small atoms, such as Helium, which has been computed in the context of NSDI, for example, are extremely demanding [22, 111, 112]. Therefore much of the numerical work has been undertaken within the single active electron approximation (SAE), such that the active electron is moving in an effective potential determined by the frozen core electrons and the Coulomb potential. The other drawback of numerical simulations is that even though the solution may be close to the experimental result, much of the underlying physics is hard to diesntangle.

Methods borrowed from quantum chemistry have been used with much success in modelling the effect of multi-electron systems, and especially diatomic molecules. These include the time-dependent density functional theory (TDDFT) [25, 66, 67, 113] and the multi-configurational time-dependent Hartree-Fock (MCTDHF) theory [24, 26, 68, 114].

The essence of TDDFT is to express the TDSE in terms of the electron density, rather than using the wavefunction itself. This is possible because the electron density completely determines all properties of the ground state, as shown for static systems by Hohenberg and Kohn [115], and for the time-dependent domain by Runge and Gross [116]. The time-dependent Kohn-Sham equations [117] give rise to a self consistent computational scheme,

$$i\frac{\partial \Psi_i(\mathbf{r},t)}{\partial t} = \left[-\frac{\nabla^2}{2} + v_{eff}(\mathbf{r},t)\right], \tag{3.19}$$

where i=1,2.....N, with N being the number of electrons and v_{eff} is an effective potential made up of functions of the density. In principle the method is exact, although in practice the exchange-correlation term, which appears in the effective potential, has no exact solution. The application of TDDFT to molecules in strong laser fields has shown the importance of lower lying molecular orbitals in determining the harmonic spectrum. It has been shown that interference between different orbital contributions may have, for certain molecules, a significant effect on the overall harmonic spectrum. For example, in diatomic Fluorine, F_2, the interference minimum in the harmonic spectrum of a TDDFT calculation is well predicted by the interference condition in Eq. (2.5), whereas, in diatomic Nitrogen, N_2, the TDDFT spectrum is no longer in agreement [25]. This has been attributed to the contribution of lower lying molecular orbitals. Further TDDFT work shows that the magnitude of the harmonic spectrum strongly depends on the destructive or constructive interference between different molecular orbitals. For example, a harmonic spectrum calculated using the HOMO only and one considering the HOMO as well as lower lying orbitals, may be vastly different. Specifically, in selected homonuclear moelcules it was found that the harmonic spectrum from the HOMO alone had much higher yields than the harmonic spectra in which the contributions from lower

lying orbitals were considered as well. This indicates destructive interference between orbital contributions. For heteronuclear molecules the yield from the HOMO alone was similar to that considering more deeply bound orbitals as well [67], indicating that the asymmetry reduces this interference effect between bound molecular orbitals.

TDDFT scales well with dimensionality, and as seen above, has improved our understanding of diatomic molecules in strong fields. However, as it is a ground state theorem, it cannot be used to model excited state dynamics, and the undetermined form of the exchange-correlation functional suggests that a more accurate this hard to diesntangle model multi-electron effects and excitation. In this sense, the MCTDHF method is the closest approximation to fully numerical solution TDSE, as it actually converges to the exact TDSE result in its limit. The MCTDHF approach [118, 119] is an extension of the simple Hartree-Fock (HF) approach [12]. When using the HF approach to solve the TDSE, the wavefunction is approximated by a Slater determinant which contains all the single electron contributions to the multi-electron wavefunction. Due to the anti-symmetric nature of the Slater determinant, HF includes electron exchange exactly but does not incorporate electron correlation. This approach is extended in the MCTDHF theory by using a linear combination of Slater determinants and therefore contains all possible excited states, as well as electron correlation.

The use of the MCTDHF theory has played a vital role in understanding the influence of multi-electron effects on high harmonic spectra, although so far it has only been applied to diatomic, two-electron and four-electron systems. For these systems, core dynamics have been shown to have a substantial effect on the harmonic spectra, and their influence varies depending on the symmetry of the electron molecular orbital [24]. The importance of core excitation by the returning electron wavepacket has been demonstrated as the most dominant route to core excitation [26, 68], rather than excitation during ionization or by the laser field during propagation. Finally, the polarization of the diatomic species was found to mask the two-center interference in the harmonic spectrum [26, 68].

3.4 Classical interpretation

Although numerical approaches are extremely useful in modelling laser atom interactions, it is difficult to decouple the physics of the process from the results one obtains. Completely classical simulations are extremely useful in this context. The simplest interpretation is to consider an unbound electron, in one-dimension, moving in the strong laser field without the influence of the Coulomb potential. Within the framework of the SFA this corresponds to the moment after ionization. For a linearly polarized, continuous wave, monochromatic field, pointing in the direction of the unit vector $\hat{e}_\eta$, which

is used throughout this work unless otherwise stated, the vector potential $\mathbf{A}(t)$ is given by,

$$\mathbf{A}(t) = \hat{e}_\eta \frac{E_0}{\omega} \cos(\omega t), \tag{3.20}$$

where E_0 is the electric field amplitude and ω is the angular frequency. Taking the electric field to be polarized in the z-direction, and considering dynamics in one-dimension, the electron released into the continuum at time t_0 will have a velocity,

$$v = (A(t_0) - A(t)), \tag{3.21}$$

where the vector potential, $A(t)$, is defined in Eq. (3.20).

The first, time-dependent term in Eq. (3.21) is known as the quiver velocity, which describes the oscillatory motion in the field, whereas the second time-independent term, is known as the drift velocity, which causes a constant drift of the electron from the core. If one defines the ponderomotive energy,

$$U_p = \frac{E_0^2}{4\omega^2}, \tag{3.22}$$

which is the laser cycle averaged quiver energy, one can see that the maximum kinetic energy that can be obtained from the field is $2U_p$. However, if the electron is constrained to return to the core, the maximum energy that can be obtained is $3.17U_p$. By solving these equations one sees that the maximum energy an electron can obtain from the field occurs when an electron is released into the continuum at $t_0 \simeq 0.3T$, where $T = \frac{2\pi}{\omega}$. Therefore, based on this intuitive picture, assuming that an electron is released into the continuum at a time t_0, which leads to it returning to the core with maximum kinetic energy and then recombining with the core, the maximum harmonic order, n_{max} would be,

$$n_{max} = \frac{I_p + 3.17U_p}{\omega}, \tag{3.23}$$

where I_p corresponds to the ionization potential of the ground state to which the electron is recombining.

By integrating Eq. (3.21) one obtains the electron position,

$$x(t) = \frac{\sin(t_0) - \sin(t)}{\omega^2} + A(t_0)(t - t_0), \tag{3.24}$$

where again one sees that the second term, which depends on the time the electron is released into the continuum, is responsible for the drift of the electron.

3.5 Classical and semi-classical trajectory-based approaches

Despite the simple classical arguments of a charged particle in an electromagnetic field giving a good prediction of the cutoff energy, classical trajectory Monte Carlo (CTMC) methods mostly do not reproduce the correct harmonic spectra or the most important features, such as the plateau and cutoff. Using semi-classical approaches, the importance of quantum interference can be assessed. The essence of semi-classical approaches is to replace the Feynmann propagator $K(\mathbf{r}, \mathbf{r}', t)$, by its semi-classical counterpart in the equation,

$$\Psi(\mathbf{r}, t) = \int_0^t d\mathbf{r}' K(\mathbf{r}, \mathbf{r}', t)\Psi(\mathbf{r}'), \tag{3.25}$$

which ammounts to neglecting some of the possible paths in the fully quantum calculation. The Feynmann propagator was replaced by the Herman-Kluk propagator [88] when comparing CTMC, semi-classical and fully quantum solutions of the TDSE in [89, 90]. In this work, it was found that interference between particular trajectories, so called 'regular' and 'irregular', lead to the harmonic cutoff. Notably, when these trajectories are included, the semi-classical calculation reproduces the cutoff seen in the fully numerical quantum calculation, whereas, if these trajectories are removed from the semi-classical simulation, the cutoff in the harmonic spectrum is lost. The classical calculation in this work has no cutoff, as one would expect as there is no interference between contributing trajectories. Recently, a comparison between CTMC and the TDSE also showed that the CTMC method did not reproduce the plateau or the cutoff [120].

A drawback of many semi-classical methods is that tunneling ionization cannot be modelled, so systems in srong fields must either be studied in the multiphoton regime or the ionization step neglected by placing the electron wavepacket at the quiver distance [89, 90, 121]. The strong-field approximation (SFA) is a successful semi-classical approximation in which tunnelling ionization is incorporated. When calculating harmonic generation within the SFA, the wavefunction is approximated as a superposition of the ground states and the continuum states,

$$\mid \Psi(t)\rangle = e^{I_p t}\left(a(t) \mid \Psi_0\rangle + \int d^3\mathbf{k} b(\mathbf{k}, t) \mid \mathbf{k}\rangle\right), \tag{3.26}$$

where I_p is the ionization potential of the system, $\mid \Psi_0\rangle$ is the ground state wavefunction and $\mid \mathbf{k}\rangle$ is a continuum state. Usually, depletion of the ground state is neglected, such that $a(t) \approx 1$. Much of the work in this thesis will involve extending Eq. (3.26) to multi-electron diatomic systems.

Apart from the SFA, which has been ubiquitous in the modelling of strong field phenomena for the last two decades, other semi-classical approaches, apart from those cited

above, have received surprisingly little attention.

3.6 The coupled coherent state approach

The Coupled Coherent State (CCS) approach is a fully quantum, trajectory based theory which has been used with a great deal of success in modelling non-sequential double ionization (NSDI) [122, 123]. In this method, the Schrödinger is expanded on a basis of Gaussians, which are constrained to move on classical trajectories governed by Hamilton's equations. There are many advantages of the CCS approach : it is a trajectory based, it fully includes the binding potential, it scales favourable with dimensionality and it is fully quantum. As previously mentioned, classical trajectory models, although successful at reproducing features in NSDI experiments, fail when modelling HHG because the plateau structure is an interference effect [89, 90, 121]. Crucially, an advantage of CCS over the semi-classical Herman-Kluk (HK) method [88] is that quantum interference is fully incorporated between all trajectories, rather than just with its nearest neighbour, and as it is fully quantum tunneling can in principle be accounted for. The main advantage over the SFA is that the Coulomb potential is included throughout the electron propagation and multi-electron effects are in principle fully considered.

Chapter 4

The strong-field approximation

4.1 Traditional SFA

The strong-field approximation (SFA) was first proposed by Keldysh in 1964 to investigate ionization during the interaction of an atom with an electric field [124]. Along with work by Faisal [125] and Reiss [126] this became known as Keldysh-Faisal-Reiss theory. The Keldysh parameter,

$$\gamma = \sqrt{\frac{|\ E_0\ |}{2U_p}}, \tag{4.1}$$

determines whether ionization occurs via tunnelling or multiphtonon ionization, with $\gamma < 1$ indicating that we are in the tunneling ionization regime and $\gamma > 1$ indicating the multi-photon ionization regime. Much of the work investigating HHG has been carried out in the tunneling regime, and this will also be the case in this thesis. Part of the reason for the success of the three step model in modelling HHG is that in the tunelling regime multi-photon resonances and excitation are less likely to play an important role in the phenomenon and can safely be neglected.

The SFA was applied to HHG by Lewenstein et. al. [46] and also independently by Becker et. al. [127], using a zero-range potential. The two approaches were later unified [128]. In this chapter, the SFA which was first developed and implemented for atomic systems is preseneted. Then, in Sec. 4.2, an extended SFA, in which we can model HHG for diatmonic systems, is explained and compared to the original formalism.

4.1.1 SFA transition amplitude

We now present a formal derivation of the strong-field approximation (SFA) [46, 128], which will be extended in further chapters to investigate orbital symmetry and the effect

of multiple orbitals in diatomic molecules on the harmonic spectrum. Here the derivation from [128] is followed.

We wish to compute the expectation value of the dipole operator in an arbitrary form, defined as $\hat{\mathbf{d}}$,

$$\mathbf{R}(t) = \langle \Psi(t) \mid \hat{\mathbf{d}} \mid \Psi(t) \rangle \tag{4.2}$$

The time evolution operator, $U(t,t')$, propagates the wavefunction $\mid \Psi_0(t') \rangle$, from some time before the pulse, t', to t, under the influence of the full Hamiltonian, given in Eq. (3.2), such that,

$$\mid \Psi(t) \rangle = U(t,t') \mid \Psi(t') \rangle \tag{4.3}$$

This equation is inserted into Eq. (4.2), giving,

$$\mathbf{R}(t) = \lim_{t't'' \to -\infty} \langle \Psi_0(t') \mid U(t',t) \hat{\mathbf{d}} U(t,t'') \mid \Psi_0(t'') \rangle. \tag{4.4}$$

The time-evolution operator to be written as,

$$\begin{aligned} U(t,t') &= U_0(t,t') - i \int_{t'}^{t} dt'' U_0(t,t'') H_I(t'') U(t'',t') \\ &= U_0(t,t') - i \int_{t'}^{t} dt'' U(t,t'') H_I(t'') U_0(t'',t'), \end{aligned} \tag{4.5}$$

which is called the Dyson equation, and where $U_0(t,t')$ is the time evolution for a system under the influence of the field free Hamiltonian, defined in Eq. (3.3). This evolution operator satisfies

$$\begin{aligned} i\frac{\partial}{\partial t} U_0(t,t') &= H_0 U_0(t,t') \\ -i\frac{\partial}{\partial t} U_0(t,t') &= U_0(t,t') H_0. \end{aligned} \tag{4.6}$$

The term $H_I(t)$ is the interaction Hamiltonian which depends on the choice of gauge. In the length gauge $H_I(t) = -\mathbf{r} \cdot \mathbf{E}(t)$ and in the velocity gauge $H_I(t) = \mathbf{A}(t) \cdot \mathbf{k}$. Now inserting the Dyson equation into Eq. (4.4), one obtains four terms,

$$
\begin{aligned}
\mathbf{R}(t) &= \langle \Psi_0(t') \mid U_0(t,t')\hat{\mathbf{d}}U_0(t,t'') \mid \Psi_0(t'')\rangle \\
&- i\int_{-\infty}^{t} dt' \langle \Psi_0(t') \mid U_0(t',t)\hat{\mathbf{d}}U(t,t')H_I(t')U_0(t',t'') \mid \Psi_0(t'')\rangle \\
&+ i\int_{-\infty}^{t} dt'' \langle \Psi_0(t') \mid U_0(t',t'')H_I(t'')U(t'',t)\hat{\mathbf{d}}U_0(t,t'') \mid \Psi_0(t'')\rangle \\
&+ \int_{-\infty}^{t} dt'' \int_{-\infty}^{t} dt' \langle \Psi_0(t') \mid U_0(t',t'')H_I(t'')U(t'',t) \\
&\quad \times \hat{\mathbf{d}}U(t,t')H_I(t')U_0(t',t'') \mid \Psi_0(t'')\rangle.
\end{aligned}
\tag{4.7}
$$

Now the strong-field approximation is made, and the full time-evolution operator, $U(t,t')$, is replaced by the Volkov time-evolution operator, $U_V(t,t')$, which corresponds to the Hamiltonian without the presence of the binding potential,

$$
\begin{aligned}
i\frac{\partial}{\partial t}U_V(t,t') &= \left(\frac{\mathbf{k}^2}{2} + H_I(t)\right) U_V(t,t') \\
-i\frac{\partial}{\partial t'}U_V(t,t') &= U_V(t,t') \left(\frac{\mathbf{k}^2}{2} + H_I(t')\right).
\end{aligned}
\tag{4.8}
$$

Noting that the first term on the right hand side of Eq. (4.7) vanishes due to the symmetry of the wavefunction and the dipole operator and neglecting continuum-continuum transitions, which corresponds to neglecting the last term on the right hand side of Eq. (4.7) one is left with,

$$
\mathbf{R}(t) = -i\int_{-\infty}^{t} dt' \langle \Psi_0(t) \mid \mathbf{d}U_V(t,t')H_I(t')) \mid \Psi_0(t')\rangle + c.c., \tag{4.9}
$$

which is the dipole moment recovered in [46, 128]. Utilizing

$$
\mid \Psi_0(t)\rangle = e^{-iE_0 t} \mid \Psi_0\rangle, \tag{4.10}
$$

where E_0 is the energy of the state $\mid \Psi_0(t)\rangle$, and using the identity operator in momentum space, one obtains,

$$
\begin{aligned}
\mathbf{R}(t) &= -i\int d\mathbf{k}_1 \int d\mathbf{k}_2 \int_{-\infty}^{t} dt' e^{-E_0(t-t')} \langle \Psi_0 \mid \hat{\mathbf{d}} \mid \mathbf{k}_1\rangle \\
&\quad \times \langle \mathbf{k}_1 \mid U_V(t,t') \mid \mathbf{k}_2\rangle \langle \mathbf{k}_2 \mid H_I(t') \mid \Psi_0\rangle + c.c..
\end{aligned}
\tag{4.11}
$$

The explicit expressions for $\langle \mathbf{k}_1 \mid U_V(t,t') \mid \mathbf{k}_2\rangle$ can be obtained by utilizing the unitary equivalence of the length, velocity and Krammers-Henneberger (KH) gauges, as presented in Appendix C. Working in the KH gauge is convenient because in this gauge

the Volkov wave has the form of a plane wave, so that we can write the time evolution operator as

$$U_V(t,t') = \exp(-i\frac{\mathbf{k}^2}{2}(t-t')). \tag{4.12}$$

Then moving between gauges, using the expression,

$$e^{-i\mathbf{r}\cdot\mathbf{A(t)}} \mid \mathbf{k}\rangle = \mid \mathbf{k} - \mathbf{A}(t)\rangle, \tag{4.13}$$

and taking the Fourier transform over all time, to obtain a frequency spectrum, one obtains the transition amplitude within the SFA,

$$\begin{aligned} M(\Omega) &= -i\int_{-\infty}^{\infty} dt \int_{-\infty}^{t} dt' \int d^3\mathbf{k} a^*_{rec}(\tilde{\mathbf{k}}) a_{ion}(\tilde{\mathbf{k}}) \\ &\quad \times \exp[iS(t,t',\Omega,\mathbf{k})] + c.c., \end{aligned} \tag{4.14}$$

where

$$a_{rec}(\tilde{\mathbf{k}}) = \langle \tilde{\mathbf{k}} \mid \hat{\mathbf{d}} \mid \Psi_0 \rangle, \tag{4.15}$$

and

$$a_{ion}(\tilde{\mathbf{k}}) = \langle \tilde{\mathbf{k}} \mid H_I(t') \mid \Psi_0 \rangle, \tag{4.16}$$

are referred to as the recombination and ionization dipole matrix elements, respectively, and $S(t,t',\Omega,\mathbf{k})$, is given by,

$$S(t,t',\Omega,\mathbf{k}) = -\frac{1}{2}\int_{t'}^{t} [\mathbf{k} + \mathbf{A}(\tau)]^2 d\tau - E_0(t-t') + \Omega t, \tag{4.17}$$

which is the semi-classical action.

The expressions for the Volkov state $\mid \tilde{\mathbf{k}}\rangle$ is gauge dependent, which arises from the lack of orthogonality of the ground state and the Volkov state, which was introduced to the system in Eq. (4.9). In the length gauge the canonical momentum becomes $\mid \tilde{\mathbf{k}}\rangle = \mid \mathbf{k} + \mathbf{A}(\tau)\rangle$, where $\tau = t, t'$, whereas in the velocity gauge there is no change, $\mid \tilde{\mathbf{k}}\rangle = \mid \mathbf{k}\rangle$. In the length gauge formalism the continuum wavefunction is refered to as a field dressed plane wave. This shift occurs when moving to the KH gauge to the length gauge, which is the unitary transformation in Eq. (C.6) and is due to Eq. (4.13). Such a shift does not occur when moving from the KH gauge to the velocity gauge, which is the unitary transformation in Eq. (C.5).

It can be see that the ionization prefactor has a dependence on $H_I(t')$, which depends on the gauge the Hamiltonian is expressed in, whereas the recombination prefactor has a dependency form of the dipole operator $\hat{\mathbf{d}}$. The length-gauge formulation will be used throughout this work. The correct choice of gauge has given rise to much debate, and it

has been shown that the length gauge gives rise to potential energy shifts of which the meaning is not clear [48]. Nonetheless, when using the velocity gauge it has been shown that two-center interference patterns are absent [49, 108].

Finally, in the length and velocity forms, the recombination matrix element can be conveniently expressed as,

$$a^{(l)}_{(rec,0)}(\mathbf{k}) = -i\frac{\partial \Psi_0(\mathbf{k})}{\partial \mathbf{k}}, \tag{4.18}$$

or,

$$a^{(v)}_{(rec,0)}(\mathbf{k}) = \mathbf{k}\Psi_0(\mathbf{k}), \tag{4.19}$$

respectively. This indicates that it is convenient to obtain the ground state momentum space wavefunction in order to calculate the prefactors.

4.1.2 Saddle-point approximation

To solve Eq. (4.14), one can exploit the highly oscillatory nature of the action and look for t', t and $\mathbf{k}$ where the action is stationary. This approach is called the saddle-point approximation (SPA). These stationary values will make the largest contributions to the integral, such that $\partial S(t,t',\mathbf{k})/\partial t' = 0$, $\partial S(t,t',\mathbf{k})/\partial t = 0$ and $\partial S(t,t',\mathbf{k})/\partial \mathbf{k} = \mathbf{0}$. This leads to the following three equations,

$$\frac{[\mathbf{k} + \mathbf{A}(t')]^2}{2} + E_0 = 0, \tag{4.20}$$

$$\int_t^{t'} d\tau [\mathbf{k} + \mathbf{A}(\tau)] = \mathbf{0}, \tag{4.21}$$

and

$$\frac{[\mathbf{k} + \mathbf{A}(t)]^2}{2} + E_0 = \Omega, \tag{4.22}$$

respectively. These equations can be interpreted as follows. Equation (4.20) gives the conservation of energy while tunneling. It only has complex solutions, as it corresponds to the quantum mechanical nature of tunneling ionization at time t' and has no classical counterpart. Equation (4.21) constrains the electron to return to the site of its ionization. Finally, Eq. (4.22), gives the conservation of energy when the returning electron recombines with the orbital of energy E_0, giving rise to a harmonic of frequency Ω [1, 2].

The real parts of the solutions of the above stated equations are related to the start times and return times of a classical electron in the laser field. The imaginary parts of these solutions, on the other hand, are associated with classically forbidden processes and in the case of Eq. (4.20), the width of the barrier the active electron must tunnel through.

Each cycle of the laser field gives rise to a pair of trajectories, called the 'long' and 'short' trajectories, due to the time the electron spends in the continuum. This is shown for a pair of trajectories in Fig. 2.3. In a single wave cycle, all harmonics generated have a 'long' and a 'short' contribution, except for the cutoff harmonic, which only has a single trajectory contribution per laser cycle. One can observe from the figure that most trajectories ionize near the maximum of the field. However, for the lower order harmonics, the possible return times vary by almost a laser period depending on whether we have a long or short trajectory. Moving to higher harmonics the difference between the return time of the long and the short trajectory get closer until they converge onto the same time at the higher harmonics, which correspond to the cutoff harmonics. Also, it should be noted that most of the ionization occurs at a very specific time during the laser period. As the ionization step of harmonic generation is largely responsible for the overall intensity of the emitted harmonic, this explains why one observes a plateau type structure of almost equal intensity in the harmonic spectrum.

In addition to the 'long' and 'short' trajectory, an ionized electron wavepacket may return within the same cycle or for any cycle after the first cycle. Hence, there are an infinite number of saddle solutions for a given harmonic, and thus an infinite number of pairs of trajectories. In this work, the first three pairs of trajectories are chosen, where the first pair corresponds to recombination within the first cycle, the second pair to recombination in the second cycle and the third pair to recombination in the third cycle. Electron trajectories that remain in the continuum for a long time experience significant wavefunction spreading resulting in decreasing contributions from longer trajectories. However, they will give rise to more substructure in the harmonic spectrum due to interference between possible trajectories.

In addition, we note that in order to obtain distinct harmonic peaks at odd harmonics in a symmetric system, we must consider trajectories ionized from each cycle. The periodicity of the field will then give rise to the odd harmonics. In this work, we consider only trajectories starting in the first cycle of the laser field. As the focus of this work is on structural features in the harmonic spectra, which such peaks may distort, considering the periodicity of the field is not relevant for the analysis. Therefore we consider only ionization from the first cycle, which is suitable for this purpose.

In Fig. 4.1 we show the various different tpes of trajectories for a continuous wave laser field. We show two of the possible ionization times in the first cycle, represented by the black and red lines, and see that these correspond to two different possible return times. We also show that ionization can occur in the next half cycle, as represented by the blue lines. Only trajectories which begin in the first half cycle are included in this work.

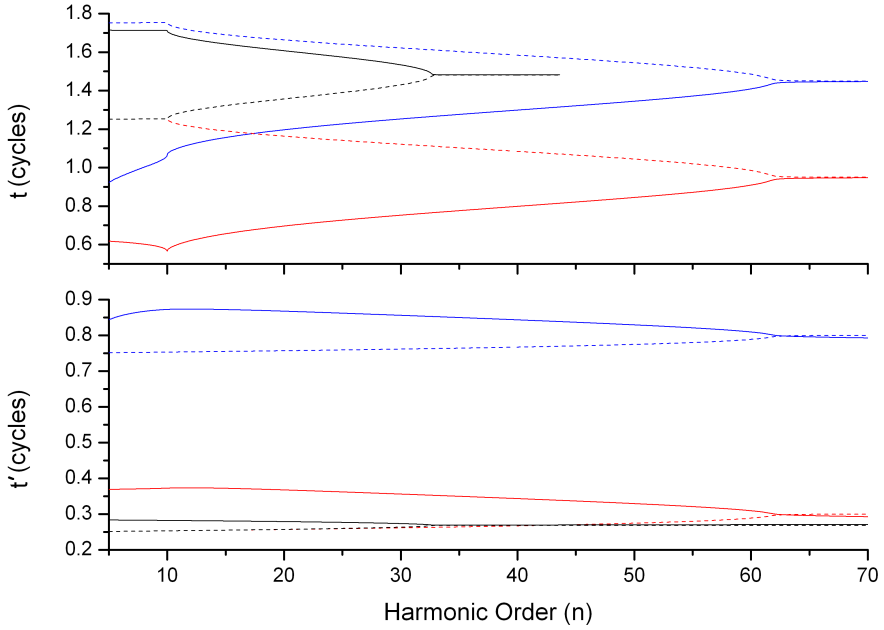

FIGURE 4.1: Real part of the start time, t', and recombination times, t, shown in the lower and upper panels, respectively, of electron trajectories for a harmonic of order n. We are using a continuous wave sin field. The dashed and solid lines correspond to the long and short trajectories, respectively. Red lines correspond to ionization and recombination in the first cycles and black lines to ionization in the first cycle and recombination in the second cycle. The blue lines represent the similar trajectories as those by the red lines except occuring 0.5 cycles later.

Having solved the saddle point equations, the transition matrix element can be written as a summation of the saddle solutions,

$$M(\Omega) = \sum_s A_s \exp[iS(t_s, t'_s, \Omega, \mathbf{k}_s)] \tag{4.23}$$

where

$$A_s = (2\pi)^{5/2} \frac{a_{rec}(\mathbf{k}_s + A(t_s))a_{ion}(\mathbf{k}_s + A(t'_s))}{(\sqrt{detS''(t_s, t'_s, \Omega, \mathbf{k}_s)})}. \tag{4.24}$$

In the above stated equation, $detS''(t_s, t'_s, \Omega, \mathbf{k}_s)$ represents the 5×5 determinant of the second derivatives of the action with regard to t_s, t'_s and k_s. Equation (4.23) can be further simplified by considering $\mathbf{k}$ according to the return condition in Eq. (4.21). This will lead to a 2×2 determinant with regard to t_s and t'_s

4.1.3 Uniform approximation

One can see from Fig. 2.3, that as one approaches the cutoff harmonic, the real parts of the ionization and return times converge to the same value. In fact, it is only the complex nature of the trajectories that prevents the saddles from fully coalescing. This is a problem for the standard SPA because it assumes that saddle points are independent of each other. The nearly coalescing saddles leads to a cusp, and one saddle starts to diverge after the Stokes transition . This problem can be partially solved by removing a saddle by hand [129]. However, a cusp still remains at the higher harmonics. A much more elegant solution is to use the uniform approximation (UA). Unlike the SPA, in which the action is expanded up to only the second order, the UA expands the action to higher orders. Considering a pair of trajectories, i and j, the transition amplitude, within the uniform approximation, prior to the cutoff, may be written in terms of BesselJ functions [130],

$$\begin{aligned} M_{i+j} &= \sqrt{-2\pi\Delta S/3}\exp[i\overline{S}+i\pi/4]\times[\Delta A(J_{1/3}(-\Delta S)+J_{-1/3}(-\Delta S)) \\ &\quad +\overline{A}(J_{2/3}(-\Delta S)-J_{-2/3}(-\Delta S))], \end{aligned} \tag{4.25}$$

and beyond to the cutoff, in terms of BesselK functions,

$$M_{i+j}=\sqrt{2i\Delta S/\pi}\exp[i\overline{S}]\times[\overline{A}K_{1/3}(-i\Delta S)+i\Delta AK_{2/3}(-i\Delta S)], \tag{4.26}$$

where $\Delta S=\frac{(S_i-S_j)}{2}$, $\overline{S}=\frac{(S_i+S_j)}{2}$, $\Delta A=\frac{(A_i-iA_j)}{2}$ and $\overline{A}=\frac{iA_i+A_j}{2}$.

The above equations require no additional information about the electron trajectories. All that is required is for us to calculate the action and the prefactors in Eq. (4.25) and Eq. (4.26). When the saddles are well separated, the UA reduces to the standard SPA. For more details see [130, 131]

4.2 Extension to diatomic molecules

So far, the theory that has been outlined in Sec. 4.1.1 is for a general one-electron ground state corresponding to a general potential V(**r**). For a Hydrogen atom, for example, the ground state $\mid \Psi_0\rangle$ can be found analytically by an exact solution of the time-independent Schrödinger equation and then used in the strong-field approximated transition amplitude in Eq. (4.14). For the specific case of diatomic molecule, there is no exact analytical solution, so to obtain Ψ, one approach is to use a linear combination of atomic orbitals (LCAO),

$$\Psi(\mathbf{r}) = \sum_{\alpha} c_{\alpha}^{(L)} \psi_{\alpha}^{(L)}(\mathbf{r} + \frac{\mathbf{R}}{2}) + (-1)^{l_\alpha - m_\alpha + \lambda_\alpha} c_{\alpha}^{(R)} \psi_{\alpha}^{(R)}(\mathbf{r} - \frac{\mathbf{R}}{2}), \tag{4.27}$$

where $\mathbf{R}$ is the internuclear distance, l is the orbital quantum number, m is the magnetic quantum number and λ determines the orbital symmetry, with $\lambda = m$ corresponding to gerarde (even) and $\lambda = m + 1$ corresponding to ungerarde (odd). The LCAO approach is an effective way of reproducing a molecular orbital if a) the energies of the atomic orbital (AO) at each center are comparable, if b) there is a large overlap between the AOs and if c) the AOs have the same symmetry properties with respect to the symmetry properties of the molecular orbital. The AOs themselves can be expanded as Slater type orbitals (STOs), or each STO expanded as a combination, or 'contraction', of Gaussian type orbitals (GTOs). For the 1s state of hydrogen centred at the origin, the STO is of the form $e^{-\zeta r}$ whereas a GTO is of the form $be^{-\zeta r^2}$. Although STOs are a more suited basis when modelling a molecular orbital, as they are the exact form of the 1s Hydrogen orbital, and their behaviour at $r \to \infty$ is more fitting to a molecular system, GTOs are much more widespread in the quantum chemistry community, due to their convenient mathematical properties [12]. The Gaussian theorem, for example, states that product of two Gaussians centered at different positions is proportional to a single Gaussian centered at a third position,

$$e^{-\zeta_A (r-R_A)^2} e^{-\zeta_B (r-R_B)^2} = K_{AB} e^{-\zeta_p (r-R_p)}, \tag{4.28}$$

where,

$$K_{AB} = e^{-\frac{\zeta_A \zeta_B (R_A - R_B)^2}{\zeta_p}}, \tag{4.29}$$

with

$$\zeta_p = \zeta_A + \zeta_B, \tag{4.30}$$

and

$$R_p = \frac{\zeta_A R_A + \zeta_B R_B}{\zeta_p}. \tag{4.31}$$

We will use this relation in later Chapters, especially Chapter 6. By using a combination of GTOs to mimic the behaviour of an STO and choosing the correct contraction coefficient, b, by a least squares fit, one obtains the same behaviour of the STOs but with the mathematical conveniences of the GTO, as shown in Fig. 4.2. Having said this STOs have been employed in some instances by the strong field community [27, 47, 81], and therefore both methods will be presented and compared in what follows.

The highest occupied molecular orbital (HOMO), HOMO-1 and lowest unoccupied molecular orbital (LUMO) for N_2 are displayed in Fig. 4.3. These orbitals have been calculated using the GTO contraction described above. These three molecular orbitals

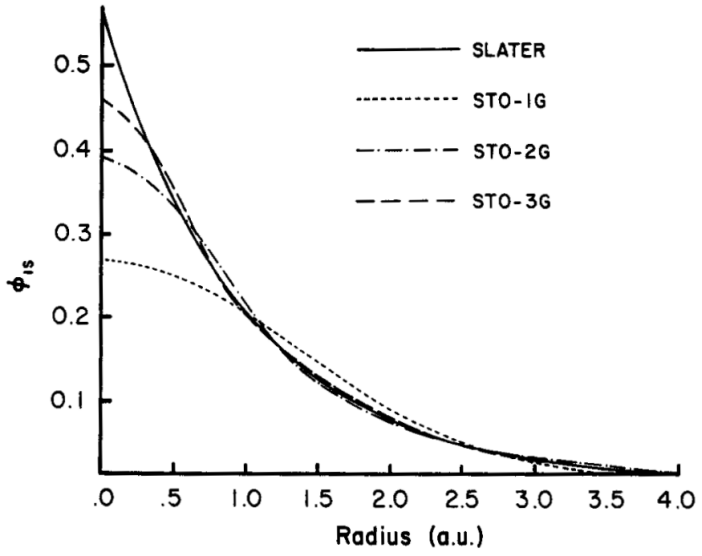

FIGURE 4.2: Comparison of a Slater type orbital (STO) used for a 1s atomic state and its approximation with one, two and three contractions of Gaussian type orbitals (GTO) [12]. The coefficients for the GTO are obtained using a least squares fit.

are widely employed in this work and include the σ_g orbital, the π_u orbital and the π_g orbital, displayed in Figs. 4.3 a), b) and c), respectively. The subscripts correspond to the symmetry of the orbital, with g standing for gerarde symmetry and u standing for ungerarde symmetry. We also note that the π_u and π_g orbitals are degenerate.

4.2.1 Gaussian vs Slater basis sets in molecular orbital construction

Starting with a GTO contraction, we now give the expressions for a general atomic wavefunction ψ, given in Eq. (4.27). This reads,

$$\psi_\alpha(\mathbf{r}) = \sum_j c^\chi_{\alpha,j}\phi^{(\chi)}_j(\mathbf{r}), \tag{4.32}$$

where,

$$\phi^\chi_j(\mathbf{r}) = \sum_\nu b^\chi_\nu (r_\beta)^{l_\alpha} e^{-\zeta^\chi_\nu r^2}, \tag{4.33}$$

and β=x,y,z is determined by the orbital one wishes to reconstruct, π_x, π_y, σ, respectively. Also, $\chi = L, R$ depending on the left or the right atom. This is a distinction which is required for heteronuclear molecules but for homonuclear molecules the coefficients will be the same as the atomic orbital used at each atom will be the same. The expansion coefficient b is called the contraction coefficient, we refer to c as the LCAO coefficient and ζ is an exponential coefficient. All of these coefficients are obtained from the quantum chemistry code GAMESS-UK [13]. The diatomic system is modelled within

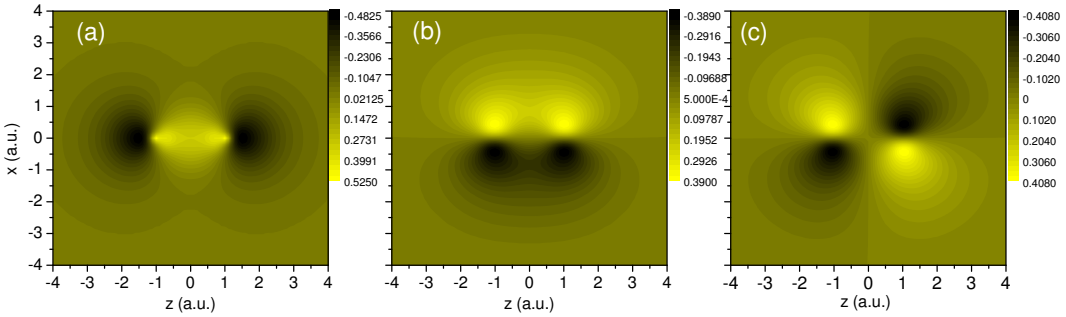

FIGURE 4.3: Molecular orbitals in position space corresponding to a) the HOMO, which is a $3\sigma_g$ type orbital b) the HOMO-1 which is a $1\pi_u$ type orbital and c) the LUMO, which is a $1\pi_g$ type orbital, of N_2. We use a LCAO with 6-31G split valence basis and an equilibrium internuclear separation of 2.068 a.u. The energies of these orbitals are $E_{3\sigma_g}$=-0.63485797 a.u., $E_{1\pi_u}$=-0.65087981 a.u. and $E_{1\pi_g}$=0.17238733 a.u., respectively.

the Born-Oppenheimer approximation, which is valid for larger systems, such as N_2 and O_2 [81].

For much of the work within that follows an expression for the momentum space wavefunction is beneficial, as it can be conveniently used in determining the recombination matrix element displayed in Eq. (4.18) and Eq. (4.19). Considering only p-type and s-type atomic orbitals, this is written as

$$\Psi(\mathbf{k}) = \sum_{\alpha} \exp[\frac{i\mathbf{k}\cdot\mathbf{R}}{2}]\psi_{\alpha}^{(L)}(\mathbf{k}) + (-1)^{l_\alpha - m_\alpha + \lambda_\alpha} \exp[\frac{-i\mathbf{k}\cdot\mathbf{R}}{2}]\psi_{\alpha}^{(R)}(\mathbf{k}), \tag{4.34}$$

where,

$$\psi_{\alpha}^{\chi}(\mathbf{k}) = \sum_{j,\nu} c_{\alpha,j}^{\chi} b_{\nu}^{\chi} \phi_{\nu}^{\chi}(\mathbf{k}), \tag{4.35}$$

and,

$$\phi_{\nu,j}^{\chi}(\mathbf{k}) = (-ik_\beta)^{l_\alpha} \frac{\pi^{3/2}}{2^{l_\alpha}(\zeta_\nu^{\chi})^{3/2+l_\alpha}} \exp[-\frac{k^2}{4\zeta_\nu^{\chi}}]. \tag{4.36}$$

When actually calculating the molecular orbital a split valence basis is used. This means that the LCAO coefficients of the core orbitals are the same, however the valence orbitals coefficients are split. For example, a 6-31G basis means that six Gaussians are used to model the 1s electrons, each with the same LCAO coefficient, whereas four are used to model the 2s and 2p electrons, with the fourth having a different LCAO coefficient to the previous three.

Rather than using a GTO contraction, one may express the atomic orbitals ψ_α^χ in Eq. (4.27) as STOs, which reads as,

$$\psi_\alpha^\chi(\mathbf{r}) = \frac{c_\alpha^\chi(2\zeta_\alpha^\chi)^{n_\alpha+1/2}}{\sqrt{(2n_\alpha)!}} r^{n_\alpha-1} e^{-\zeta_\alpha^\chi r} Y_{l_\alpha}^{m_\alpha}(\theta,\phi), \tag{4.37}$$

where in this instance the coefficients c_α and ζ are obtained from the literature [14], and $Y_{l_\alpha}^{m_\alpha}(\theta,\phi)$ is a spherical harmonic. The momentum space wavefunction in a STO basis, corresponding to Eq. (4.35) is,

$$\begin{aligned}\psi_\alpha^\chi(\mathbf{k}) &= \frac{(-ik)^{l_\alpha} 2^{n_\alpha-l_\alpha}(\zeta_\alpha^\chi)^{-l_\alpha+3/2}}{\sqrt{(2n_\alpha)!}} \frac{\Gamma(2+l_\alpha+n_\alpha)}{\Gamma(3/2+n_\alpha)} \\ &\quad \times {}_2F_1(a_1,a_2,a_3,a_4) Y_{l_\alpha}^{m_\alpha}(\theta_p,\phi_p),\end{aligned} \tag{4.38}$$

where F is a hypergeometric function and $a_1 = 1+(l_\alpha+n_\alpha)/2$, $a_2 = a_1+1/2$, $a_3 = l_\alpha+3/2$ and $a_4 = -k^2/(\zeta_\alpha^\chi)^2$. Finally, the polar and $\theta_p = \cos^{-1}(p_z/p)$ and the azimuthal angle $\phi_p = \tan^{-1}(p_y/p_x)$.

4.2.2 Analytical form of the dipole matrix elements

The dipole matrix element for recombination, as in Eq. (4.18), for a general molecular orbital of a diatomic molecule, ψ_j, can be calculated analytically to give,

$$\begin{aligned}a_{(rec,j)}^{(l)} &= i\sum_\alpha c_\alpha^{(L)} \exp[i\mathbf{k}\cdot\frac{R}{2}]\partial_{\mathbf{k}}\Phi_{\alpha,j}^{(L)}(\mathbf{k}) + (-1)^{l_\alpha-m_\alpha+\lambda_\alpha} c_\alpha^{(R)} \exp[i\mathbf{k}\cdot\frac{R}{2}]\partial_{\mathbf{k}}\Phi_{\alpha,j}^{(R)}(\mathbf{k}) \\ &\quad + \frac{\mathbf{R}}{2}\Lambda_j(\mathbf{k}),\end{aligned} \tag{4.39}$$

where,

$$\Lambda_j(\mathbf{k}) = \sum_\alpha c_\alpha^{(L)} \exp[i\mathbf{k}\cdot\frac{R}{2}]\phi_{\alpha,j}^{(L)}(\mathbf{k}) + (-1)^{l_\alpha-m_\alpha+\lambda_\alpha} c_\alpha^{(R)} \exp[i\mathbf{k}\cdot\frac{R}{2}]\phi_{\alpha,j}^{(R)}(\mathbf{k}), \tag{4.40}$$

when using the length form and,

$$a_{(rec,j)}^{(v)} = \sum_\alpha c_\alpha^{(L)}\mathbf{k} \exp[i\mathbf{k}\cdot\frac{R}{2}]\Phi_{\alpha,j}^{(L)}(\mathbf{k}) + (-1)^{l_\alpha-m_\alpha+\lambda_\alpha} c_\alpha^{(R)}\mathbf{k} \exp[i\mathbf{k}\cdot\frac{R}{2}]\Phi_{\alpha,j}^{(R)}(\mathbf{k}), \tag{4.41}$$

in the velocity form.

In the length form recombination matrix element, Eq. (4.39), the third term on the right hand side increases with internuclear separation. In fact, one finds that when using the SFA an atomic system does not posses translational invariance, such that this term will increase as the system is moved from the origin of the co-ordinate system. This artefact

has been attributed to the lack of orthogonality between the continuum states, which in the SFA is approximated by field dressed plane waves, and the ground state [108]. Such problems do not occur when using the velocity form of the dipole operator, as we can see by inspecting Eq. (4.41). Previous calcualtions on homonuclear molecules within the SFA have shown that the velocity form is the prefered form of the dipole operator when describing molecular systems [48], because it is as more accurate than the acceleration form when calculating two-center interference and easier to compute.

4.2.3 Interference condition

The recombination matrix element Eq. (4.14) contains all of the structural information about the molecular system. This term can fully be described by the momentum space wavefunction, as detailed in Sec. 4.2.2. Therefore, minima in the momentum space wavefunction will lead to minima in the harmonic spectrum. Now we present a generalised interference condition, which is a heteronuclear extension to the homonuclear interference condition presented in [27]. This goes beond the simple interference conditions mentioned in the introduction, where s-p mixing is not considered [57, 71], and the wavefunction is assumed to be symmetric, which in this instance is simply a summation of two s-type atomic oprbitals. The momenum space wavefunction, Eq. (4.34), for a molecular orbital built of s- and p-type atomic orbitals, can be re-expressed in terms of trigonometric functions,

$$\psi_j(\mathbf{k}) = \sum_\alpha C_+^{(\alpha,j)} \cos[\frac{\mathbf{k}\cdot\mathbf{R}}{2}] + iC_-^{(\alpha,j)} \sin[\frac{\mathbf{k}\cdot\mathbf{R}}{2}], \tag{4.42}$$

where,

$$C_\pm^{\alpha,j} = \pm c_{\alpha,j}^{(L)} \phi_{\alpha,j}^{(L)}(\mathbf{k}) + (-1)^{l_\alpha - m_\alpha + \lambda_\alpha} c_{\alpha,j}^{(R)} \phi_{\alpha,j}^{(R)}(\mathbf{k}) \tag{4.43}$$

Defining,

$$\vartheta = \arctan\left(\frac{iC_+^{\alpha,j}}{C_-^{\alpha,j}}\right), \tag{4.44}$$

gives,

$$\psi_j(\mathbf{k}) = \sqrt{(C_+^{\alpha,j})^2 - (C_-^{\alpha,j})^2}\sin(\vartheta + \frac{\mathbf{k}\cdot\mathbf{R}}{2}). \tag{4.45}$$

Seeing that Eq. (4.42) sees a minimum when Eq. (4.45) sees a minimum, one expects interference minima in the harmonic spectra when considering field dressed plane waves, if,

$$\vartheta + [\mathbf{k} + \mathbf{A}(t)] \cdot \frac{\mathbf{R}}{2} = \kappa\pi. \tag{4.46}$$

Using the saddle point equation, Eq. (4.22), for the specific case of a continuous wave, linearly polarized laser of frequency ω, the harmonic minima will occur at,

$$n = \frac{E_0}{\omega} + \frac{2(\kappa\pi - \vartheta)}{\omega R^2 \cos^2(\theta_L)}, \tag{4.47}$$

where θ_L is the angle between the momentum vector, which is in the direction of the laser field polarization, and the position vector, or in other words, the angle between the internuclear axis and the laser field polarization.

Now we compare the two types of orbital construction described in Sec. 4.2.1 and their effect on the interference minimum. In Fig. 4.4, we display results, either computed with a 6-31G gaussian basis set and coefficients obtained from GAMESS-UK [13], or with STOs, and the coefficients in [14] [upper and lower panels, respectively]. The outcome of the split-valence computation, displayed in Fig. 4.4 a), exhibits a minimum which, for parallel molecular alignment, is near $\Omega = 25\omega$. This is a slightly higher harmonic order than that observed in [27] (see Fig. 4 therein). The minima observed for the individual s and p contributions, in contrast, agree with the results presented in [27] (c.f. Fig. 4.4.(b) and Fig. 4.4 c), respectively). This suggests that the s-p mixing possesses different weights in the present case and in [27]. The spectra obtained with the Slater-type orbitals, on the other hand, are practically identical to the results in [27]. This holds both for the minimum in the full $3\sigma_g$ spectrum [Fig. 4.4 d)], which, for parallel alignment, is close to $\Omega = 21\omega$, and for the patterns present in the s and p contributions [Fig. 4.4 e) and Fig. 4.4 f), respectively]. We have ruled out that this discrepancy is due to the slightly different ionization potentials employed in the two computations by performing a direct comparison for the same set of parameters (not shown). We have also found, employing GAMESS-UK and several types of basis sets, that the minimum at $\Omega = 25\omega$ is rather robust with respect to small variations of $E_{3\sigma_g}$ and R [1]. Hence, in comparison to our computations, it seems that the contributions of the s states to the spectra are slightly underestimated in [14].

4.2.4 Modified saddle-point equations

When modelling diatomic molecules within the framework of the strong-field approximation, the molecular structure can either be incorporated into the ionization and recombination prefactors or into the action. Incorporating the molecular structure into the

[1] Apart from the 6-31G basis set mentioned in this work, which has been used to compute the spectra in Figs. 1.(a)-(c), we have employed the following basis sets in GAMESS-UK: STO-3G (Slater-type orbitals, three Gaussians), and several split-valence basis sets, namely 3-21G, 4-21G, 4-31G, 5-31G, and 6-21G. For all cases we found that the two-center interference minimum of the $3\sigma_g$ spectrum agreed with Fig. 4.4 a). For more details on split valence basis sets see, e.g., J. Stephen Binkley, John A. Pople, Warren J. Hehre, J. Am. Chem. Soc. **102**, 939 (1980).

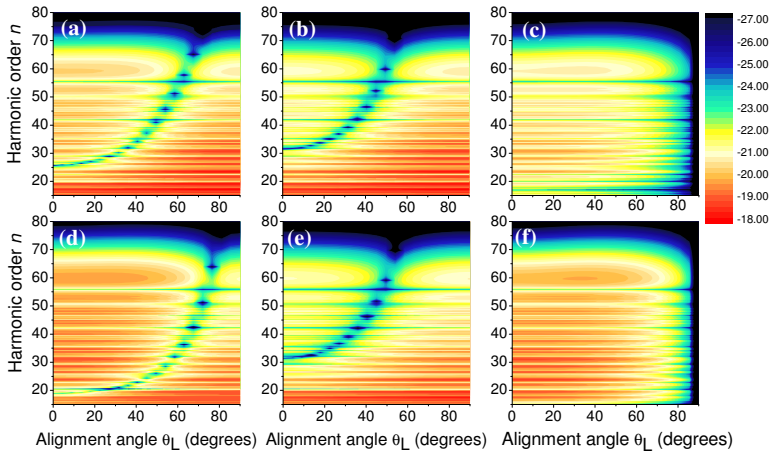

FIGURE 4.4: High-order harmonic spectra for the HOMO in N_2 subject to a linearly polarized laser field of frequency $\omega = 0.057$ a.u. and intensity $I = 4 \times 10^{14} W cm^{-2}$, as a function of the alignment angle θ_L between the molecular axis and the field. The spectra in the upper panels have been constructed using a gaussian basis set and coefficients obtained from GAMESS-UK [13], while those in the lower panels have been built using Slater-type orbitals, and the coefficients in [14]. From left to right, we display the spectra from the full $3\sigma_g$ orbital [panels (a) and (d)], the contributions from the s states [panels (b) and (e)], and those from the p states [panels (c) and (f)]. The bound-state energy of the HOMO and the equilibrium internuclear distance have been taken from the respective computations. For the upper panels, $E_{3\sigma_g} = 0.63485797$ a.u., while for the lower panels $E_{3\sigma_g} = 0.63495$ a.u. In both cases, $R = 2.068$ a.u.

prefactor amounts to inserting the momentum space wavefunction, Eq. (4.34), into the recombination prefactors Eq. (4.18) or Eq. (4.19), depending on whether we choose the length or velocity form. However the SPA assumes that the prefactors are slowly varying compared to the semi-classical action, which is not necessarily the case, especially for large internuclear distances [132]. Another, more accurate approach is therefore to incorporate the molecular structure into the action [49]. In this instance, the transition amplitude in Eq. (4.14) can be expressed as a summation,

$$M(\Omega) = \sum_{\mu,\nu} M_{\mu,\nu}, \tag{4.48}$$

where

$$\begin{aligned} M_{\mu,\nu}(\Omega) &= -i \int_{-\infty}^{\infty} dt \int_{-\infty}^{t} dt' \int d^3\mathbf{k} J_{\mu,\nu}(t,t',\mathbf{k}) \\ &\quad \times exp[iS(t,t',\Omega,\mathbf{k})] + c.c, \end{aligned} \tag{4.49}$$

and

$$J_{\mu,\nu}(t,t',\mathbf{k}) = \sum_{\alpha,\beta} \Xi_{\mu,\nu} c_\alpha^{*(\mu)} c_\beta^{(\nu)} \partial_{\mathbf{k(t)}} \phi_\alpha^{*\mu}(\mathbf{k}(t)) \partial_{\mathbf{k(t')}} \phi_\beta^{\nu}(\mathbf{k}(t')), \tag{4.50}$$

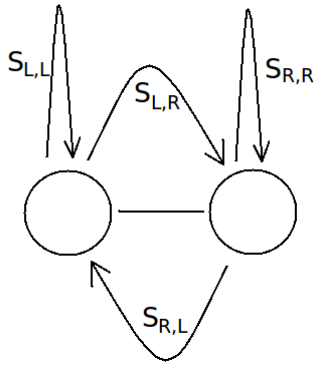

FIGURE 4.5: Schematic of contributions to the overall harmonic yield when incorporating the molecular structure of a diatomic molecule into the action. $S_{L,L}$ and $S_{R,R}$ are the direct harmonics, where the electron leaves and returns to the same center, whereas $S_{L,R}$ and $S_{R,L}$ are the exchange harmonics, where the electron leaves from one center and returns to the other.

where μ and ν represent the left and right ions with $\Xi_{L,L} = 1$, $\Xi_{L,R} = (-1)^{l_\beta - m_\beta + \lambda_\beta}$, $\Xi_{R,L} = (-1)^{l_\alpha - m_\alpha + \lambda_\alpha}$ and $\Xi_{R,R} = \Xi_{R,L}\Xi_{L,R}$. The action now takes two forms, one for $\mu = \nu$,

$$S_{\mu,\mu}(t, t', \Omega, \mathbf{k}) = S(t, t', \Omega, \mathbf{k}) \pm (\mathbf{A}(t) - \mathbf{A}(t')) \cdot \frac{\mathbf{R}}{2}, \tag{4.51}$$

which leads to the so called direct harmonics, where an electron ionizes and recombines to the same center, and the other for $\mu \neq \nu$,

$$S_{\mu,\nu}(t, t', \Omega, \mathbf{k}) = S(t, t', \Omega, \mathbf{k}) \pm \mathbf{k} \cdot \mathbf{R} \pm (\mathbf{A}(t) + \mathbf{A}(t')) \cdot \frac{\mathbf{R}}{2}, \tag{4.52}$$

which leads to the exchange harmonics, where ionization and recombination occur at different centers [49, 132]. These contributions are displayed in Fig. 4.5

If one now follows the same procedure as in Sec. 4.1.2 and employs the SPA one obtains,

$$\frac{[\mathbf{k} + \mathbf{A}(t')]^2}{2} + E_0 \pm \frac{\mathbf{E}(t') \cdot \mathbf{R}}{2} = 0, \tag{4.53}$$

when differentiating with respect to t', and

$$\frac{[\mathbf{k} + \mathbf{A}(t)]^2}{2} + E_0 \pm \frac{\mathbf{E}(t) \cdot \mathbf{R}}{2} = \Omega, \tag{4.54}$$

when differentiating with respect to t. An additional term appears on the left hand side of Eq. (4.53), in comparison to Eq. (4.20), which signifies a potential energy shift, depending on which side of the molecule ionization occurs from. The same is also apparent for recombination, which can be seen when comparing Eq. (4.21) and Eq. (4.54). These potential energy shifts have raised much debate [49, 132] and are

dependent on the form of the dipole operator and the choice of gauge when the SFA [2, 48, 108].

Finally, when differentiating with respect to $\mathbf{k}$ the two contributions from Eq. (4.51) will be the same as Eq. (4.22), with the only difference being that ionization and recombination will now occur to and from an atomic center, rather than the geometric center of the molecule. However, Eq. (4.52) will give rise to,

$$-\int_{t'}^{t} d\tau[\mathbf{k}+\mathbf{A}(\tau)] \pm \mathbf{R} = \mathbf{0}, \tag{4.55}$$

which corresponds to an electron, ionized from the left/right atom, travelling a distance $\mathbf{R}$ and then recombining with the right/left atom. The positive and negative signs in Eq. (4.55) correspond to $S_{R,L}$ and $S_{L,R}$ respectively. Interestingly, it can be seen that in this instance the momentum is no longer parallel to the field. This observation has been suggested as the origin of elliptical harmonics from linearly polarised laser fields [133].

We will investigate the importance of exchange harmonics when modelling the effect of nodal structures in molecular orbitals on the harmonic spectrum in Chapter 8.

Chapter 5

Multi-electron ground state wavefunction

Now the SFA formalism presented in the previous section, which considered a single active electron, as is usually taken for SFA calculations, is extended to multi-electron systems. Much of the work on harmonics from many electron diatomic systems assume that the highest occupied molecular orbital (HOMO) is sufficient in describing the phenomenon [7, 27, 81, 134]. The reason for this that the ionization probability of a system is exponentially dependent of the binding energy of the molecular orbital, making ionization from orbitals lying below the HOMO much less likely. However, after the observation of the contributions from the HOMO-1 to the harmonic spectrum in N_2 [23], it was recognized that the orbital geometry of the orbital from which ionization is occurring also plays a significant role in determining ionization probability, as discussed in Chapter 2. A particularly important feature in a molecular orbital is the presence of a nodal plane, which is a region of vanishing electron density ion the position space wavefunction. Experimentally aligning diatomic species N_2, O_2 and CO_2 prior to ionization [58], one observes that molecular orbitals with nodal structures aligned along the polarization axis of the driving field experience a substantial decrease in ionization relative to when these nodal structures are aligned perpendicular to the polarization axis [9, 23].

If the binding energies of the HOMO and HOMO-1 in a diatomic species are separated by only a few electron volts, such that to the first approximation the potential an electron has to overcome to ionize form either orbital is similar, one would anticipate orbital geometry will becoming extremely important in determining whether only one orbital dominates the harmonic spectrum or whether both contribute. This is especially true if either the HOMO or HOMO-1 contain any nodal structures, which, for example, is the

case in diatomic Nitrogen, N_2. In Fig. 4.3 b) we see that the HOMO-1 of N_2 exhibits a nodal plane along the internuclear axis, whereas the HOMO, displayed in Fig. 4.3 a) has most of its electron density located along the internuclear axis. Below we investigate the interplay of these two orbitals and the effect of this orbital geometry on the harmonic spectrum.

5.1 Theory

The SFA for an arbitrary single electron diatomic systems is now extended to a multi-level diatomic system. For a general n-electron Hartree-Fock wavefunction, the ground-state wavefunction which will be incorporated in the ionization and recombination prefactors may be written as,

$$\mid \Psi_0\rangle = \frac{1}{\sqrt{N!}}\hat{A} \mid \psi_0^{(1)}, \psi_0^{(2)}, ...\psi_0^{(N)}\rangle, \tag{5.1}$$

where $\hat{A}$ is the antisymmetrization operator, N is the number of active electrons and $\mid \psi_0^{(j)}\rangle$ represents the active orbitals one wishes to incorporate. Spin degrees of freedom are neglected. For this N-electron system the dipole operator, which is taken in the length form, reads,

$$\mathbf{r} = \sum_{j=1}^{N} \mathbf{r}^{(j)}, \tag{5.2}$$

and the time evolution operator becomes,

$$\begin{aligned} U_{SFA}(t,t') &= U_{SFA}^{(1)}(t,t') \otimes U_0^{(2)}(t,t') \otimes ...U_0^{(N-1)}(t,t') \otimes U_0^{(N)}(t,t') \\ &+U_0^{(1)}(t,t') \otimes U_{SFA}^{(2)}(t,t')...U_0^{(N-1)}(t,t') \otimes U_0^{(N)}(t,t') + ... \\ &+U_0^{(1)}(t,t') \otimes U_0^{(2)}(t,t')...U_0^{(N-1)}(t,t') \otimes U_{SFA}^{(N)}(t,t'). \end{aligned} \tag{5.3}$$

The Dyson equation, as displayed in Eq. (4.5), in the strong field approximation where the time evolution operator has been replaced by the Volkov time evolution operator, may be written for the electron j as,

$$U_{SFA}^{(j)}(t,t') = U_0^{(j)}(t,t') - i\int_{t'}^{t} dt'' U_V^{(j)}(t,t'') H_I(t'') U_0^{(j)}(t'',t'). \tag{5.4}$$

The evolution operator in Eq. (5.3) describes the physical process in which an electron is ionized and propagated in the continuum under the strong field approximation, $U_{(SFA)}$, while the remaining electrons remain bound and are propagated by the field free Hamiltonian, U_0. The processes corresponding to the propagating and the bound electrons have been decoupled, which means that effects such as core polarization, relaxation and

electron migration, for example, are not treated in this framework and the remaining core is treated statically.

We apply the method to N_2, with a HOMO of σ_g geometry and HOMO-1 of π_{ux} geometry, although the method itself is applicable to any multi-level level system. Initially only two dimensions and two active electrons are considered, which we take to be the x-z plane. However, this will then be extended to three dimensions, such that the degeneracy of the $\pi_{u,x}$ and $\pi_{u,y}$ orbitals in N_2 is fully accounted for. In this instance, three electrons are considered. The effects of orbital degeneracy have been shown to have a significant effect in HHG, for example, in organic molecules [135]. The derivation and corresponding results presented here have been published in [1].

The two electron ground state wavefunction of N_2, in the x-z plane, may be expressed as

$$\mid \Psi_0\rangle = \frac{1}{\sqrt{2}}(\mid 3\sigma_g^{(1)}\rangle \mid 1\pi_u^{(2)}\rangle - \mid 3\sigma_g^{(2)}\rangle \mid 1\pi_u^{(1)}\rangle), \tag{5.5}$$

where the index j=1,2 refers to the electron in question. In the length form, the dipole operator will read,

$$\mathbf{r} = \mathbf{r}^{(1)} + \mathbf{r}^{(2)}. \tag{5.6}$$

The multi-electron SFA time evolution operator is written as,

$$U_{(SFA)}(t,t') = U_{(SFA)}{}^{(1)}(t,t') \otimes U_0^{(2)}(t,t') + U_0^{(1)}(t,t') \otimes U_{(SFA)}^{(2)}(t,t'). \tag{5.7}$$

We now use the ground state wavefunction in Eq. (5.5) to calculate the expectation of the dipole moment, as in Eq. (4.2). This gives,

$$\mathbf{R}(t) = \mathbf{d}_1(t) + \mathbf{d}_2(t) + \mathbf{d}_3(t) + \mathbf{d}_4(t), \tag{5.8}$$

where,

$$\mathbf{d}_1(t) = \frac{1}{2}\langle 3\sigma_g^{(1)} \mid \langle 1\pi_u^{(2)} \mid [\mathbf{r}^{(1)} + \mathbf{r}^{(2)}] \mid 3\sigma_g^{(1)}\rangle \mid \pi_u^{(2)}\rangle \tag{5.9}$$

$$\mathbf{d}_2(t) = -\frac{1}{2}\langle 1\pi_u^{(1)} \mid \langle 3\sigma_g^{(2)} \mid [\mathbf{r}^{(1)} + \mathbf{r}^{(2)}] \mid 3\sigma_g^{(1)}\rangle \mid \pi_u^{(2)}\rangle \tag{5.10}$$

$$\mathbf{d}_3(t) = -\frac{1}{2}\langle 3\sigma_g^{(1)} \mid \langle 1\pi_u^{(2)} \mid [\mathbf{r}^{(1)} + \mathbf{r}^{(2)}] \mid 1\pi_u^{(1)}\rangle \mid \ 3\sigma_u^{(2)}\rangle \tag{5.11}$$

$$\mathbf{d}_4(t) = \frac{1}{2}\langle 1\pi_u^{(1)} \mid 3\sigma_g^{(2)}[\mathbf{r}^{(1)} + \mathbf{r}^{(2)}] \mid 1\pi_u^{(1)}\rangle \mid \ 3\sigma_u^{(2)}\rangle. \tag{5.12}$$

$$\tag{5.13}$$

Following the same procedure as in Chapter 4, except now utilising the two electron evolution operator in Eq. (5.7), one obtains,

$$\begin{aligned}\mathbf{d}_1(t) &= \langle 3\sigma_g^{(1)} \mid U_0^{\dagger(1)}\mathbf{r}^{(1)}U_{SFA}^{(1)} \mid 3\sigma_g^{(1)}\rangle \\ &+ \langle 1\pi_u^{(2)} \mid U_0^{\dagger(2)}\mathbf{r}^{(2)}U_{SFA}^{(2)} \mid 1\pi_u^{(2)}\rangle + c.c., \end{aligned} \tag{5.14}$$

where c.c. is the complex conjugate of the first term,

$$\mathbf{d}_2(t) = 0, \tag{5.15}$$

$$\mathbf{d}_3(t) = 0, \tag{5.16}$$

and

$$\begin{aligned}\mathbf{d}_4(t) &= \langle 1\pi_u^{(1)} \mid U_{SFA}^{\dagger(1)}\mathbf{r}^{(1)}U_0^{(1)} \mid 1\pi_u^{(1)}\rangle \\ &+ \langle 3\sigma_g^{(2)} \mid U_{SFA}^{\dagger(2)}\mathbf{r}^{(2)}U_0^{(2)} \mid 3\sigma_g^{(2)}\rangle + c.c.. \end{aligned} \tag{5.17}$$

The time dependence in the evolution operator and the orbitals has been dropped to make the notation more readable. Equations (5.14) and (5.17) indicate that the total transition amplitude for a two electron wavefunction is a summation of one-electron transition amplitudes. Consequently, within this formalism, it is not possible for an electron to leave one orbital and recombine with another orbital. This is due to the assumptions made upon the evolution operator which, physically, implies that once an electron is removed from a given orbital, j, the system remains frozen during the propagation of that electron, such that even if a hole is created, it remains in the same orbital. We insert the Dyson equation, Eq. (5.4), into the total transition amplitude, Eq. (5.8), which in two dimensions becomes,

$$\mathbf{M}(\Omega) = \left| \sum_{j,n} \mathbf{M}_{j,j}^{(n)} + c.c. \right|^2, \tag{5.18}$$

where,

$$\begin{aligned}\mathbf{M}_{j,j}^{(n)} &= -i\int_{-\infty}^{\infty} dt \int_{-\infty}^{t} dt' \int d^3\mathbf{k} a_{rec}^{*(j)}(\mathbf{k}_{(n)} + \mathbf{A}(t)) a_{ion}^{(j)}(\mathbf{k}_{(n)} + \mathbf{A}(t') \\ &\times \exp[iS_{j,j}(t, t', \mathbf{k}_{(n)})] + c.c., \end{aligned} \tag{5.19}$$

and j corresponds to the molecular orbital. The action, $S_{j,j}(t, t', \mathbf{k})$, where the molecular structure is incorporated in to the prefactor as in Sec. 4.1.2 and not into the action as

in Sec. 4.52, reads the same as in Eq. (4.17),

$$S_{j,j}(t,t',\mathbf{k}_{(n)}) = S(t,t',\mathbf{k}_{(n)}) - (t-t')E_j, \tag{5.20}$$

where E_j correspond to the ionization energies of orbital j and $S(t,t',\mathbf{k})$ is defined as

$$S(t,t',\mathbf{k}_{(n)}) = -\frac{1}{2}\int_{t'}^{t}[\mathbf{k}_{(n)} + \mathbf{A}(\tau)]^2 d\tau + \Omega t. \tag{5.21}$$

Taking the same approach as above, but in three dimensions, where the degeneracy of the π_{ux} and the π_{uy} orbitals is accounted for, results in the wavefunction,

$$\mid \psi_0\rangle = \frac{1}{\sqrt{6}}\begin{vmatrix} \mid 3\sigma_g^{(1)}\rangle & \mid 1\pi_{ux}^{(1)}\rangle & \mid 1\pi_{uy}^{(1)}\rangle \\ \mid 3\sigma_g^{(2)}\rangle & \mid 1\pi_{ux}^{(2)}\rangle & \mid 1\pi_{uy}^{(2)}\rangle \\ \mid 3\sigma_g^{(3)}\rangle & \mid 1\pi_{ux}^{(3)}\rangle & \mid 1\pi_{uy}^{(3)}\rangle \end{vmatrix},$$

with the three-electron dipole operator,

$$\mathbf{r} = \mathbf{r}^{(1)} + \mathbf{r}^{(2)} + \mathbf{r}^{(2)}, \tag{5.22}$$

and the three-electron evolution operator,

$$\begin{aligned} U_{(SFA)}(t,t') &= U_{(SFA)}^{(1)} \otimes U_0^{(1)} \otimes U_0^{(3)} + U_0^{(1)} \otimes U_{(SFA)}^{(2)} \otimes U_0^{(3)} \\ &\quad + U_0^{(1)} \otimes U_0^{(2)} \otimes U_{(SFA)}^{(3)}. \end{aligned} \tag{5.23}$$

Now, whereas for two dimensions the spectrum can be calculated by taking the modulus squared of the various transition amplitudes, as in Eq. (5.18), for three dimensions one must account for the fact that the azimuthal angle cannot be experimentally resolved. This is achieved by integrating over the azimuthal angle. The spectrum is then given by,

$$\mathbf{M}(\Omega) = \int_0^{2\pi}\left|\sum_{j,n}\mathbf{M}_{j,j}^{(n)} + c.c.\right|^2 d\phi_k, \tag{5.24}$$

In the case of a three-level system this will give rise to 81 terms, many of which will vanish due to symmetry considerations. Performing the integral, one obtains,

$$\mathbf{M}(\Omega) = \sum_{\alpha,\beta,i,\nu} W(\alpha,\beta,i,\nu) M_{\alpha,\beta}^*(\mathbf{k}+A(t),\theta_k) M_{i,\nu}(\mathbf{k}+A(t'),\theta_k), \tag{5.25}$$

where $W(\alpha,\beta,i,\nu)$ is given by Table 5.1.

	$M_{\sigma\sigma}$	$M_{\sigma\pi_x}$	$M_{\sigma\pi_y}$	$M_{\pi_x\sigma}$	$M_{\pi_x\pi_x}$	$M_{\pi_x\pi_y}$	$M_{\pi_y\sigma}$	$M_{\pi_y\pi_x}$	$M_{\pi_y\pi_y}$
$M_{\sigma\sigma}$	2π	0	0	0	π	0	0	0	π
$M_{\sigma\pi_x}$	0	π	0	π	0	0	0	0	0
$M_{\sigma\pi_y}$	0	0	π	0	0	0	π	0	0
$M_{\pi_x\sigma}$	0	π	0	π	0	0	0	0	0
$M_{\pi_x\pi_x}$	π	0	0	0	$3\pi/4$	0	0	0	$\pi/4$
$M_{\pi_x\pi_y}$	0	0	0	0	0	$\pi/4$	0	$\pi/4$	0
$M_{\pi_y\sigma}$	0	0	π	0	0	0	π	0	0
$M_{\pi_y\pi_x}$	0	0	0	0	0	$\pi/4$	0	$\pi/4$	0
$M_{\pi_y\pi_y}$	π	0	0	0	$\pi/4$	0	0	0	$3\pi/4$

TABLE 5.1: Weights $\mathcal{W}(\alpha, \beta, i, \nu)$, corresponding to Eq. (5.25), where the azimuthal the azimuthal angle ϕ_k has been integrated over.

5.2 Influence of the HOMO-1 on the harmonic spectra

We now use the multi-electron transition amplitude derived in the previous section to calculate the harmonic spectrum and investigate the effect of the HOMO-1. The N_2 molecular is aligned relative to the laser field polarization with an alignment angle θ_L. In our formalism, $\theta_L = 0°$ corresponds to parallel alignment and $\theta_L = 90°$ to perpendicular alignment.

The effect of multiple orbitals on the HHG spectra are initially considered in two dimensions, and the harmonic spectra are presented in Fig. 5.1. We compare Fig. 5.1 a) and 5.1 c), which correspond to the two-electron wavefunction, where the HOMO and HOMO-1 are considered, and the one electron case, which considers only the HOMO. We see that the main effect of the HOMO-1 orbital is to blur the interference minimum in the spectrum, with the blurring becoming more pronounced at higher harmonic orders. The lack of influence from the HOMO-1 at lower harmonic orders can be understood by observing Fig. 5.1 d), which shows harmonic spectrum when considering the HOMO-1 only. We see that the intensity of the spectrum is around two orders of magnitude lower than that of the spectrum from the HOMO only and that there is vanishing harmonic signal at $\theta = 0°$. The ionization potential of the $1\pi_u$ orbital is slightly higher than that of the $3\sigma_g$ orbital. This has the effect of reducing the overall ionization probability and therefore reducing the overall harmonic intensity compared to that of the HOMO. However, it is the orbital geometry of the π_u orbital, displayed in Fig. 4.3 b), which has the main effect on the harmonic spectrum. The HOMO-1 exhibits a nodal plane along the internuclear axis which means that when the molecule is aligned parallel to the laser

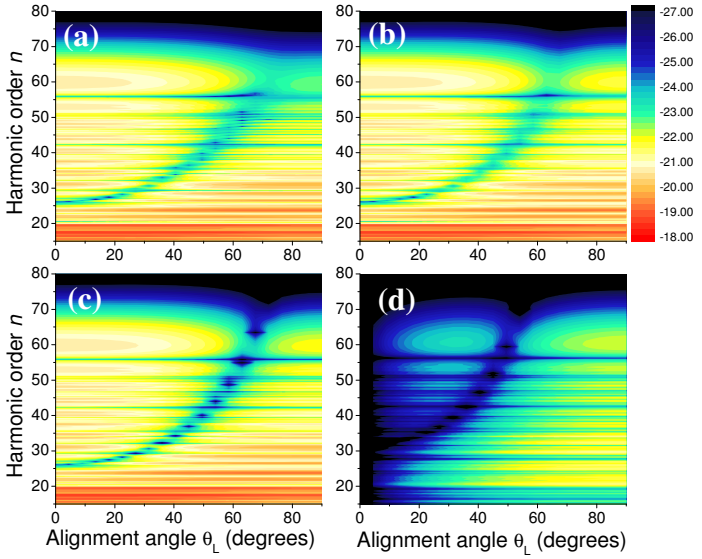

FIGURE 5.1: Contribution of different processes to the high-harmonic spectra, as functions of the alignment angle θ_L, for an N_2 molecule subject to a linearly polarized laser field of frequency $\omega = 0.057$ a.u. and intensity $I = 4 \times 10^{14} Wcm^{-2}$. We chose $\phi_p = 0$ so that the $1\pi_{uy}$ orbital does not contribute. The dipole matrix elements have been computed using a gaussian basis set and coefficients from GAMESS-UK [13]. The orbital energies are, $E_{3\sigma_g} = 0.63485797$ a.u and $E_{1\pi_u} = 0.65087981$ a.u. and the internuclear distance is $R = 2.068$ a.u. Panel (a): coherent sum $|M_{\sigma\sigma} + M_{\pi_x\pi_x}|^2$; panel (b): incoherent sum $|M_{\sigma\sigma}|^2 + |M_{\pi_x\pi_x}|^2$; panel (c): Processes involving the $3\sigma_g$ orbital, i.e., $|M_{\sigma\sigma}|^2$; panel (d): processes involving the $1\pi_{ux}$ orbital, i.e., $|M_{\pi_x\pi_x}|^2$. In order to facilitate a comparison with the next figure, the transition amplitudes have not been multiplied by a factor two to account for the two active electron and to ease comparison with the next figure, which considers three active electrons.

field, ionization is greatly reduced [9, 27, 38, 48, 49, 58, 61]. In contrast, the $3\sigma_g$ orbital is entirely localized along the internuclear axis. This implies that the overall harmonic yield from the HOMO will decrease with increasing alignment angle. The influence of the nodal plane in the $1\pi_u$ orbital however will give rise to the opposite behaviour, with the harmonic yield increasing with alignment angle and vanishing harmonic signal when $\theta_L = 0°$. Therefore, in the overall spectrum, comprised of contributions from all orbitals, displayed in Fig 5.1 a), the influence of the HOMO-1 would be expected to be more pronounced as the alignment angle increases.

The spectra resulting from the three-dimensional simulation, where three active electrons and the degeneracy of the HOMO-1 are considered, exhibits several similarities to the two-dimensional case. The resulting spectra are presented in Fig. 5.2. Once more, the contributions from the $1\pi_u$ orbitals to the harmonic spectrum, displayed in Fig. 5.2 b), are at least two orders of magnitude smaller than the contributions from the $3\sigma_g$ orbital, displayed in Fig 5.2 c). We see that the minimum in Fig. 5.2 a), which is the harmonic spectrum when considering all orbitals, becomes more blurred at increasing

alignment angles, as compared to its single active electron counterpart, displayed in Fig. 5.2 c). This is the same as the finding in the two-dimensional case. However, the blurring is slightly less pronounced than that in the two-dimensional figure. At first sight, this is a counterintuitive finding, as, in the three-dimensional case, there are two degenerate HOMO-1 orbitals so we would expect their contribution to the overall spectrum to be more pronounced. However, due to the presence of the nodal planes in the degenerate HOMO-1, for a broad range of alignment angles the contributions are strongly suppressed. In addition, the weights $\mathcal{W}(\alpha, \beta, \nu, j)$, displayed in Table 5.1, of the processes involving the $3\sigma_g$ orbital have less vanishing contributions and are larger than the ones for the $1\pi_u$ orbitals only. This will further reduce the influence of the HOMO-1.

We compare coherent and incoherent summations in Fig. 5.1 a) and b) and Fig. 5.2 a) and d). A coherent summation in the two-dimensional simulation, is described by Eq. (5.18), whereas an incoherent summation is of the form,

$$\mathbf{M}(\Omega) = \sum_{j,n} \left| \mathbf{M}_{j,j}^{(n)} + c.c. \right|^2 . \tag{5.26}$$

In the three-dimensional calculation, the coherent summation is given by Eq. (5.24), whereas an incoherent summation is

$$\mathbf{M}(\Omega) = \sum_{j,n} \int_0^{2\pi} \left| \mathbf{M}_{j,j}^{(n)} + c.c. \right|^2 d\phi_k. \tag{5.27}$$

Comparing the two types of summation allows one to assess the importance of interference between different contributions to the overall spectra, becase a coherent summation will couple different processes, whereas an incoherent summation will not. One sees that the additional terms one obtains in the coherent summation, which are of the form $M_{jj}^* M_{ii}$ where i and j represent different molecular orbitals, give rise to additional blurring in the spectra around the minima at higher harmonic orders and make the minimum less defined.

Finally, observing Fig. 5.1 d) and c) and Fig. 5.2 b) and c) which compare spectra from the HOMO and HOMO-1, one sees that the interference minima are located in very different regions. This is expected, based on the generalized interference condition Eq. (4.46), which predicts minima at different harmonic orders for orbitals of differing symmetry and s-p mixing.

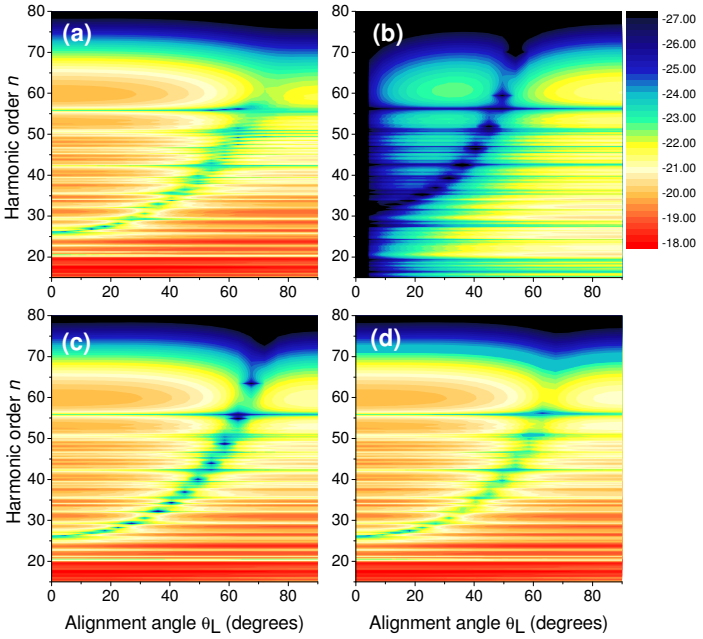

FIGURE 5.2: Contribution of different processes to the high-harmonic spectra, as functions of the alignment angle θ_L, for the same field parameters in the previous figure. We are considering a three-dimensional scenario, in which the azimuthal angular variable has been integrated over. The dipole matrix elements have been computed using a Gaussian basis set and GAMESS-UK [13]. In this case, $E_{3\sigma_g} = 0.63485797$ a.u, $E_{1\pi_u} = 0.65087981$ a.u. and $R = 2.068$ a.u. Panel (a): coherent sum $|M_{\sigma\sigma} + M_{\pi_x\pi_x} + M_{\pi_y\pi_y}|^2$; panel (b): processes involving the only $1\pi_u$ orbitals, i.e., $|M_{\pi_x\pi_x} + M_{\pi_y\pi_y}|^2$; panel (c): Processes involving the $3\sigma_g$ orbital, i.e., $|M_{\sigma\sigma}|^2$; panel (d): incoherent sum $|M_{\sigma\sigma}|^2 + |M_{\pi_x\pi_x}|^2 + |M_{\pi_y\pi_y}|^2$. In order to facilitate a comparison with the previous figure, the transition amplitudes have not been multiplied by a factor 3 to account for the three active electrons.

5.3 Conclusions

The results in this chapter show the importance of lower lying orbitals on the spectra, and that their main influence is seen in the interference minimum of multi-electron harmonic spectrum. We considered energetically close orbitals, exemplified by $3\sigma_g$ and $1\pi_u$ in N_2 and a simplified multielectron state incorporating three active electrons occupying the HOMO or HOMO-1 in N_2. The interplay between $3\sigma_g$ and $1\pi_u$ orbitals in the overall spectrum, with regard to the alignment angle between the molecule and the field-polarization direction has been investigated.

We observe that for these energetically close orbitals, the barrier through which the electron must tunnel and the maximum energy it may acquire upon recombination are almost the same. Hence, the shape in the spectrum will be mainly determined by the spatial properties of the orbitals involved. For instance, the shape and the two-center

interference patterns observed for the high-order harmonic spectra from N_2 are mainly determined by the $3\sigma_g$ orbital, even though the $1\pi_u$ orbitals are energetically very close.

Physically, this is due to the particular geometry of the $1\pi_u$ orbitals. Indeed, for small alignment angles θ_L, these orbitals exhibit a nodal plane close to the polarization axis, so that tunneling and recombination are strongly suppressed. We have verified that this dominance extends up to approximately $\theta_L = 45°$. For the parameters considered in this work, the two-center minimum occurs within this region, so that it is mainly determined by the $3\sigma_g$ orbital.

Furthermore, due to their nontrivial dependence on the azimuthal angle, the $1\pi_u$ orbitals carry less weight when this parameter is integrated over, as once done in the three-dimensional calculation. Despite the degeneracy of the $1\pi_u$ orbitals, this angular dependence outweighs the fact that there are more processes in which the electron recombines with one of the $1\pi_u$ orbitals. In this context, one should note that, in the literature, the dynamics of the problem is many times reduced to the $p_x p_z$ plane (see, e.g., [27] in which HHG from the π_g orbital of the O_2 molecule has been computed). Such models do not consider the degeneracy of π orbitals.

Chapter 6

Multi-electron Lewenstein ansatz

In the previous chapter the lower lying orbitals were incorporated into the SFA by expressing the ground state wavefunction as a Slater determinant of the HOMO and HOMO-1. In this chapter, we will adopt a slightly different approach based on the multi-electron ansatz proposed in the work of Santra and Gordon [64], which in the orginal work was applied to atomic Neon. A similar approach has been adopted by Patchkovskii et. al. [65] for molecules.

6.1 Theory

The multi-electron effects are incorporated into the dipole matrix element by making the ansatz,

$$\mid \Psi\rangle = \mid \Psi_0^N\rangle + \sum_k \frac{b_k(t)}{\sqrt{2}} \left(c_{k+}^\dagger \mid \Psi_{0-}^{N-1}\rangle + c_{k-}^\dagger \mid \Psi_{0+}^{N-1}\rangle \right), \tag{6.1}$$

which is the multi-electron extension of Eq. (3.26), where $c_{k\sigma}^\dagger$ creates an electron in a plane wave state with momentum $\mathbf{k}$ and spin $\sigma/2$ and $\mid \Psi_0^N\rangle$ is the N electron ground state wavefunction. This formalism includes exchange between the core and the continuum electron, and also includes the multi-electron N-1 core while the electron is in the continuum. By following the derivation presented in Appendix F and [64], one may write the recombination matrix element we obtained in Eq. (4.15) as,

$$a_{rec}(\mathbf{k}) = a_{rec}^{(0)}(\mathbf{k}) + a_{rec}^{(1)}(\mathbf{k}) + a_{rec}^{(2)}(\mathbf{k}) + O(H^2), \tag{6.2}$$

where,

$$a_{rec}^{(0)}(\mathbf{k}) = \langle \mathbf{k} \mid \hat{\mathbf{d}} \mid \Psi_0 \rangle, \tag{6.3}$$

which is the zeroth order prefactor corresponding to the uncorrected influence of the HOMO,

$$a_{rec}^{(1)}(\mathbf{k}) = \sum_i (\mathbf{d}_{ii}\langle \mathbf{k} \mid \Psi_0\rangle - \mathbf{d}_{i0}\langle \mathbf{k} \mid \Psi_i\rangle), \tag{6.4}$$

which is the first order correction, where,

$$\mathbf{d}_{ij} = \langle \Psi_i \mid \hat{\mathbf{d}} \mid \Psi_j\rangle \tag{6.5}$$

and,

$$\begin{aligned} a_{rec}^{(2)}(\mathbf{k}) &= \sum_i \langle \mathbf{k} \mid \Psi_i\rangle \sum_a \sum_j \mathbf{d}_{aj} \frac{v_{a0[ij]}}{\epsilon_i + \epsilon_j - \epsilon_0 - \epsilon_a} \\ &+ \sum_a \langle \mathbf{k} \mid \Psi_a\rangle \sum_b \sum_i \mathbf{d}_{ib} \frac{v_{ab[0j]}}{\epsilon_0 + \epsilon_i - \epsilon_a - \epsilon_b} \end{aligned} \tag{6.6}$$

which is the second order correction. The indicies a and b represent unoccupied orbitals and i and j represent occupied orbitals, whereas the indicie 0 represents the HOMO. The term

$$\mathbf{d}_{\nu\mu} = \langle \psi_\nu \mid \hat{\mathbf{d}} \mid \psi_\mu\rangle, \tag{6.7}$$

is the static dipole moment moment, of arbitrary form, between orbitals ν and μ,

$$v_{a0[i,j]} = \langle \Psi_i\Psi_j \mid v \mid \Psi_a\Psi_0\rangle - \langle \Psi_j\Psi_i \mid v \mid \Psi_a\Psi_0\rangle, \tag{6.8}$$

and

$$v_{ab[0,j]} = \langle \Psi_0\Psi_j \mid v \mid \Psi_a\Psi_b\rangle - \langle \Psi_j\Psi_0 \mid v \mid \Psi_a\Psi_b\rangle, \tag{6.9}$$

where v is 2 electron Coulomb operator, which may be written as,

$$v = \frac{1}{\mid \mathbf{r}_1 - \mathbf{r}_2 \mid}. \tag{6.10}$$

The above expressions are also applicable to the ionization matrix element in Eq. (4.16), with the difference that the dipole operator, $\hat{\mathbf{d}}$ should be replaced by the interaction Hamiltonian $H_I(t)$, as discussed in Sec. 4.1.1.

In the work of Santra and Gordon [64], the above approach was derived and applied to a multi-electron atomic system. It will now be extended to diatomic molecules. In [64, 65], only the recombination matrix element was considered, based on the premise that the recombination step is what is used to determine the structure of the system in tomographic imaging. However, here both the ionization $a_{ion}(\mathbf{k} + \mathbf{A}(t))$ and recombination $a_{rec}(\mathbf{k} + \mathbf{A}(t))$ matrix elements will be corrected. In the work that follows, we consider the multi-electron corrections up to the first order only, which means that we do not

	L	R
L	1	$(-1)^{l_\beta+\lambda_\beta}$
R	$(-1)^{l_\alpha+\lambda_\alpha}$	$(-1)^{l_\beta+\lambda_\beta+l_\alpha+\lambda\alpha}$

TABLE 6.1: Coefficients $\Xi_{\xi'\xi}(l_\alpha, l_\beta)$ found in Eq. (6.12) for the four possible values of the indices ξ', ξ related to the right and left ions.

employ Möller-Plesset perturbation theory, as the first order corrections will dominate. We also do not consider spin degrees of freedom, as these terms will only make a small quantitative difference.

To calculate the corrections we employ the wavefunctions for a diatomic molecule calculated using an LCAO as discussed in Sec. 4.2. One can see from Eq. (6.4) that for homonuclear molecules only the second term on the right hand side will contribute, due to the inversion symmetry of the system, such that only gerade and ungerade states are coupled. However, in the case of heteronuclear molecules, both terms will contribute, such that all orbitals are coupled, because the molecular orbitals are all asymmetric. Therefore, it is of interest, theoretically, to model both heteronuclear and homonuclear molecules. In Eq. (6.4), the momentum space wavefunction, $\langle \mathbf{k} \mid \Psi_0 \rangle$, will give rise to structural effects in the harmonic spectra whereas the dipole transition matrix elements, d_{ii} or d_{i0}, will determine the relative weighting only. This is because the dipole transition matrix element is simply a number.

The recombination matrix element for diatomic molecules, corresponding to the zeroth $a_{rec}^{(0)}(\mathbf{k} + \mathbf{A}(t'))$ order have already been presented in Sec. 4.2.2 for both the length and the velocity forms, along with the ionization matrix element $a_{ion}^{(0)}(\mathbf{k}+\mathbf{A}(t))$. This is now extended to the first order corrections for diatomic systems. The derivations and results presented here have been published in [2].

The dipole matrix element in Eq. (6.5) can be written as,

$$\mathbf{d}_{\nu,\mu} = \sum_{\alpha,l_\alpha} \sum_{\beta,l_\beta} \sum_{\varepsilon,\varepsilon'} \Xi_{\varepsilon,\varepsilon'}(l_\alpha, l_\beta) \Upsilon_{\varepsilon,\varepsilon'}^{\alpha,\beta}, \tag{6.11}$$

where,

$$\Upsilon_{\varepsilon,\varepsilon'}^{\alpha,\beta} = \int d^3r [c_{\alpha,\mu}^{(\varepsilon')}]^* c_{\beta,\mu}^{(\varepsilon)} \psi_{\alpha,\mu}^{(\varepsilon')}(\mathbf{r} + (-1)^A \mathbf{R}/2) d(\mathbf{r}) \psi_{\beta,\mu}^{(\varepsilon)}(\mathbf{r} + (-1)^B \mathbf{R}/2). \tag{6.12}$$

The superscripts A and B are 1 or 0 for $\varepsilon', \varepsilon = R$ or $\varepsilon', \varepsilon = L$ and the coefficients $\Xi_{\varepsilon,\varepsilon'}(l_\alpha, l_\beta)$ vary such that $\Xi_{L,L}(l_\alpha, l_\beta) = 1$, $\Xi_{L,R}(l_\alpha, l_\beta) = (-1)^{l_\beta+\lambda_\beta}$, $\Xi_{R,L}(l_\alpha, l_\beta) = (-1)^{l_\alpha+\lambda_\alpha}$ and $\Xi_{L,L}(l_\alpha, l_\beta) = (-1)^{l_\alpha+\lambda_\alpha+l_\beta+\lambda_\beta}$, as shown in Table 6.1. The dipole operator of arbitrary form is given by $d(\mathbf{r})$.

Equation (6.12) can be viewed as having two types of contributions, direct integrals,

$$\Upsilon^{\alpha,\beta}_{\varepsilon,\varepsilon} = \int d^3r [c^{(\varepsilon)}_{\alpha,\mu}]^* c^{(\varepsilon)}_{\beta,\mu} \psi^{(\varepsilon)}_{\alpha,\mu}(\mathbf{r} \pm \mathbf{R}/2) d(\mathbf{r}) \psi^{(\varepsilon)}_{\beta,\mu}(\mathbf{r} \pm \mathbf{R}/2), \tag{6.13}$$

where the wavefunctions are centered at the same ion and indirect integrals,

$$\Upsilon^{\alpha,\beta}_{\varepsilon,\varepsilon'} = \int d^3r [c^{(\varepsilon')}_{\alpha,\mu}]^* c^{(\varepsilon)}_{\beta,\mu} \psi^{(\varepsilon')}_{\alpha,\mu}(\mathbf{r} \mp \mathbf{R}/2) d(\mathbf{r}) \psi^{(\varepsilon)}_{\beta,\mu}(\mathbf{r} \pm \mathbf{R}/2). \tag{6.14}$$

where $\varepsilon \neq \varepsilon'$ and the wavefunctions are centered at different ions. Assuming that the overlap integrals are small and can be neglected, Eq. (6.11) can be written as,

$$\mathbf{d}_{\mu,\nu} = \sum_{\alpha,l_\alpha} \sum_{\beta,l_\beta} [c^{(L)}_{\alpha,\nu}]^* c^{(L)}_{\beta,\mu} \Upsilon^{\alpha,\beta}_{L,L} + (-1)^{l_\beta+\lambda_\beta+l_\alpha+\lambda_\alpha} [c^{(R)}_{\alpha,\nu}]^* c^{(R)}_{\beta,\mu} \Upsilon^{\alpha,\beta}_{R,R}. \tag{6.15}$$

The above integration for the direct integrals in Eq. (6.13) is now performed. The integration for the overlap integrals in Eq. (6.14) may be found in Appendix E. For a homonuclear molecule, where $c^{(L)}_{\alpha,\nu} = c^{(R)}_{\alpha,\nu} = c_{\alpha,\nu}$ and $c^{(L)}_{\beta,\mu} = c^{(R)}_{\beta,\mu} = c_{\beta,\mu}$ Eq. (6.15) may be written as,

$$\mathbf{d}_{\mu,\nu} = \sum_{\alpha,l_\alpha} \sum_{\beta,l_\beta} [c_{\alpha,\nu}]^* c_{\beta,\mu} \Upsilon^{\alpha,\beta}_{S,S} (1 + (-1)^{l_\beta+\lambda_\beta+l_\alpha+\lambda_\alpha}), \tag{6.16}$$

where $S = L = R$. For Eq. (6.16) to be non-vanishing, $l_\alpha + l_\beta + \lambda_\alpha + \lambda_\beta$ must be even. This implies that the dipole matrix element between molecular orbitals of the same symmetry, $\lambda_\alpha = \lambda_\beta$, couples atomic orbitals of the same parity, such that $l_\alpha = l_\beta$ and that the dipole matrix element between molecular orbitals of different symmetry couple atomic orbitals of different parity, such that $l_\alpha = l_\beta + 1$. Performing the integral in Eq. (6.13), taking the dipole operator to be in the length form and employing the Gaussian basis detailed in Sec. 4.2.1, one obtains,

$$\Upsilon^{\alpha,\beta}_{\varepsilon,\varepsilon}(\sigma,\sigma) = \sum_{j,j'} \frac{\pi b^{(\varepsilon)}_{j,\nu} b^{(\varepsilon)}_{j',\mu}}{\zeta^{(\varepsilon)}_{j,\nu} + \zeta^{(\varepsilon)}_{j',\mu}} \times [F(l_\alpha + l_\beta + 1) \mp \frac{R}{2} F(l_\alpha + l_\beta)], \tag{6.17}$$

for σ to σ transitions, where

$$F(l) = \frac{1}{2}[1 + (-1)^l](\zeta^{(\varepsilon)}_{j,\nu} + \zeta^{(\varepsilon')}_{j',\mu})^{-1/2-l/2} \Gamma\left[\frac{l+1}{2}\right]. \tag{6.18}$$

and the negative and positive signs correspond to $\varepsilon = L$ and $\varepsilon = R$, respectively.

The same expression as in Eq. (6.17) is obtained for π_χ to π_χ transitions, where $\chi = x$ or $\chi = y$. When coupling σ to π_χ one obtains,

$$\Upsilon^{\alpha,\beta}_{\varepsilon,\varepsilon}(\sigma,\pi_\chi) = \sum_{j,j'} \frac{\pi^{1/2} b^{(\varepsilon)}_{j,\nu} b^{(\varepsilon)}_{j',\mu}}{(\zeta^{(\varepsilon)}_{j,\nu} + \zeta^{(\varepsilon)}_{j',\mu})^{1/2}} \times [A(l_\alpha + 1, l_\beta) + A(l_\alpha, l_\beta + 1) \mp \frac{R}{2} A(l_\alpha, l_\beta)], \quad (6.19)$$

where,

$$A(l_\alpha, l_\beta) = F(l_\alpha)F(l_\beta). \quad (6.20)$$

Equation (6.19) can also be used when coupling different, π_x and π_y, orbitals. The expressions $F(l_\alpha + l_\beta + 1)$, $A(l_\alpha + 1, l_\beta)$ and $A(l_\alpha, l_\beta + 1)$ are non-vanishing only if l_α and l_β correspond to atomic orbitals of different parity. In the homonuclear case, based on the arguments for Eq. (6.16) to be non-vanishing, molecular orbitals of different symmetry $\lambda_\alpha = \lambda_\beta \pm 1$ are coupled. Physically, this implies zero static dipole moment between molecular orbitals of the same symmetry in the length form. One should note that the R dependent expressions in Eq. (6.17), which contain $F(l_\alpha + l_\beta)$ and $A(l_\alpha, l_\beta)$, couple states of the same parity, such that $l_\alpha = l_\beta$. Nonetheless, for a homonuclear molecule, when coupling molecular orbitals of the same symmetry, these terms vanishes in the summation in Eq. (6.15).

In a heteronuclear molecule, such symmetry arguments do not apply. This is because the factorization in Eq. (6.16) cannot be performed since $c^{(L)}_{\alpha,\nu} \neq c^{(R)}_{\alpha,\nu}$ and $c^{(L)}_{\beta,\mu} \neq c^{(R)}_{\beta,\mu}$, so that, as expected, all molecular orbitals will be coupled. Physically, this is because the symmetry is broken by the static dipole moment.

If the dipole operator is taken in the velocity form, and considering the dipole in Eq. (6.15), the coupling between orbitals of the same symmetry reads as,

$$\Upsilon^{\alpha,\beta}_{\varepsilon,\varepsilon}(\sigma,\sigma) = \sum_{j,j'} \frac{\pi b^{(\varepsilon)}_{j,\nu} b^{(\varepsilon)}_{j',\mu}}{\zeta^{(\varepsilon)}_{j,\nu} + \zeta^{(\varepsilon)}_{j',\mu}} \times [l_\beta F(l_\alpha + l_\beta - 1) - 2\zeta^{(\varepsilon)}_{j,\mu} F(l_\beta + l_\alpha + 1)], \quad (6.21)$$

whereas for coupling between σ and π_χ orbitals one obtains,

$$\Upsilon^{\alpha,\beta}_{\varepsilon,\varepsilon}(\sigma,\pi_\chi) = \sum_{j,j'} \frac{\pi^{1/2} b^{(\varepsilon)}_{j,\nu} b^{(\varepsilon)}_{j',\mu}}{(\zeta^{(\varepsilon)}_{j,\nu} + \zeta^{(\varepsilon)}_{j',\mu})^{1/2}} \times [B(l_\alpha, l_\beta) - 2\zeta^{(\varepsilon)}_{j,\mu} A(l_\alpha + 1, l_\beta)], \quad (6.22)$$

where,

$$B(l_\alpha, l_\beta) = F(l_\alpha)[l_\beta F(l_\beta - 1) - 2\zeta^{(\varepsilon)}_{j',\mu} F(l_\beta + 1)]. \quad (6.23)$$

As is the case for the length form, Eq. (6.21) also describes coupling of π_x to π_y. Noting again the condition for $F(l_\alpha+1, l_\beta)$, one sees that Eq. (6.21) is only non-vanishing if s and p type atomic orbitals are coupled. For homonuclear molecules, the only contribution

from Eq. (6.16) that is non-vanishing will arise if $\lambda_\alpha = \lambda_\beta \pm 1$. Therefore only states of different symmetry are coupled. This is physically to be expected as the dipole operator is an odd operator.

However, interestingly, Eq. (6.21) gives zero static dipole moment for heteronuclear moelcules, contrary to the result in the length form, Eq. (6.19). This implies that for heteronuclear molecules there is no coupling between the σ and π orbitals in this framework, which demonstrates the limitation of using this form of the dipole operator in this framework. This finding can be verified by using the properties of Gamma functions.

6.2 Harmonic spectra including multi-electron effects

Now the formalism outlined in Sec. 6.1 is employed when computing the harmonic spectra from diatomic molecules. The full three-dimensional problem is considered, which, as shown in Sec. 5.1, requires us to an integrate over the azimuthal angle ϕ_k. This is performed, in the particular case for the multi-electron corrections, in Appendix D. The isoelectronic homonuclear and heteronuclear molecules of diatomic molecular Nitrogen, N_2, and Carbon Monoxide, CO, are compared as the relative importance of the static dipole moment in CO can be assessed for different forms of the dipole operator. This is because, in principle, for heteronuclear molecules, the second term on the right hand side of Eq. (6.4) will not vanish. However, as we have just seen, the velocity form of the dipole operator finds zero static dipole moment in heteronuclear molecules.

The position and momentum space wavefunctions of the HOMO of both molecules are presented in Fig. 6.1. The position space wavefunction of N_2, displayed in Fig. 6.1 b) is symmetric about a reflection in the plane bisecting the internuclear axis, whereas the static dipole moment in the CO molecule means that this symmetry is broken. Therefore, as expected, the position space wavefunction of CO, present in Fig. 6.1 a), is asymmetric. The momentum space wavefunction of CO and N_2 are presented in Fig. 6.1 c) and d), respectively. It can be seen from Fig. 6.1 c) that even though the position space wavefunction of CO is asymmetric, its momentum space counterpart is symmetric. This observation and the influence of particular features of the momentum space wavefunction on the harmonic spectrum is analysed in more detail when looking at the effects of nodal structures on harmonic spectra in Chapter 8.

All of the bound molecular orbitals for N_2 and CO are displayed also in Fig. 6.2 and 6.3, respectively. These orbitals will be used when calculating the first order corrections in Eq. (6.4), which is a summation over all contributing bound orbitals.

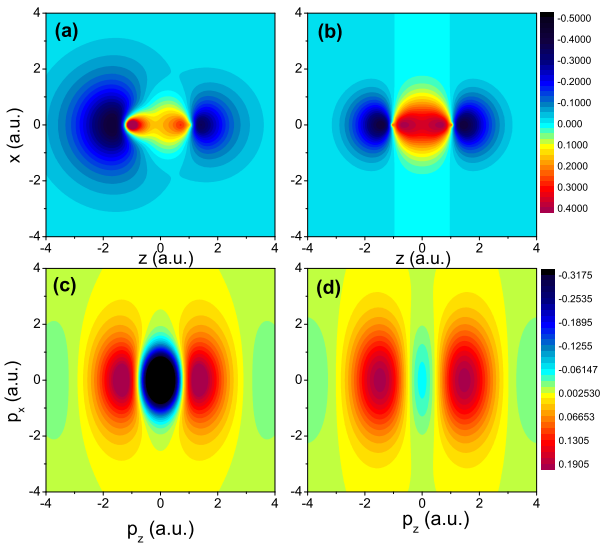

FIGURE 6.1: Highest occupied molecular orbitals for CO (panels (a) and (c)) and N2 (panels (b) and (d)), in the position and momentum space (upper and lower panels, respectively). The absolute value of the momentum space wavefunctions of the HOMO is taken. The internuclear separation for CO is taken as R=2.1283 a.u. and for N_2 as R=2.068 a.u., and the internuclear axis is along the z-axis. The orbitals are constructed using the LCAO procedure detailed in Sec. 4.2 and coefficients from GAMESS-UK [13]

The harmonic spectra from these molecules and the effects of the multi-electron corrections arising from the multi-electron ansatz are now investigated. The spectra from an N_2 molecule aligned relative to the polarization of the field, using the length and velocity forms of the dipole operator, are displayed in Fig. 6.4. Comparing Fig. 6.4 a) and b), which show the harmonic spectra in the length and velocity forms including the multi-electron corrections derived in the previous section, one sees a discrepancy in the position of the minima, with the minima in the length form at harmonic n=25 for $\theta_L = 0$ and in the velocity the minima being at approximately n=20. It can also be seen that the minima increases to higher harmonic orders much more rapidly with alignment and in the length form. We attribute this to the different s-p mixing when using different forms of the dipole operator.

We note the difference in magnitude of the length and velocity forms in Fig. (6.4) a) and b) is due to neglecting the ω term when performing the integral in Eq. (3.15). This affects the results quantitatively and is irrelevant for a qualitative analysis, but within each form, we are consistent with regard to the zeroth-order and first-order corrections.

Comparing Fig. 6.4 a) and c) and Fig. 6.4 b) and d), which corresponds to the full harmonic spectrum with the multi-electron corrections and the corrections alone, in the

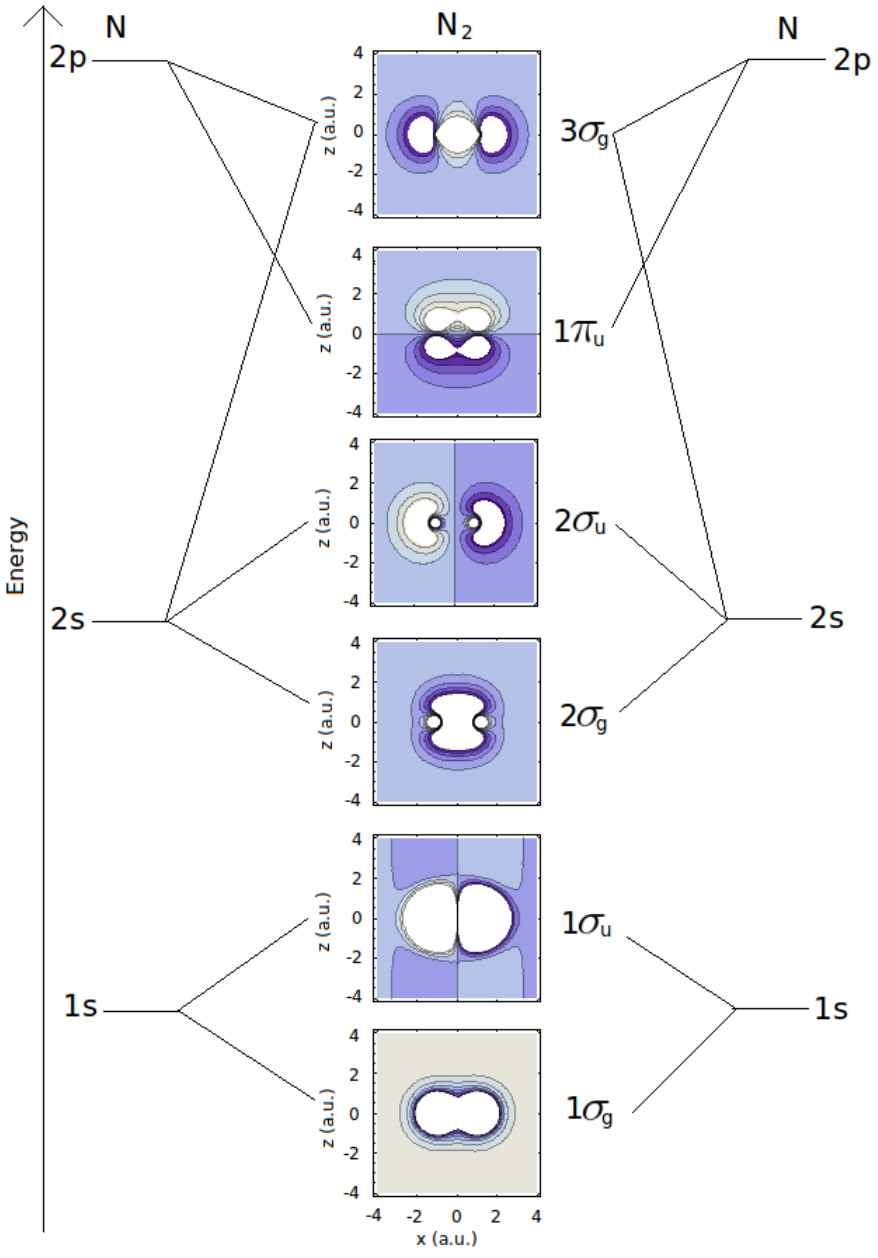

FIGURE 6.2: Schematic representation of atomic orbital contributions to bound molecular orbitals of N_2. The molecular orbitals are the position space wavefunctions, constructed using the LCAO procedure in the same way as the previous figure. The lines connecting the atomic and molecular orbitals symbolise the contribution of the former to the latter.

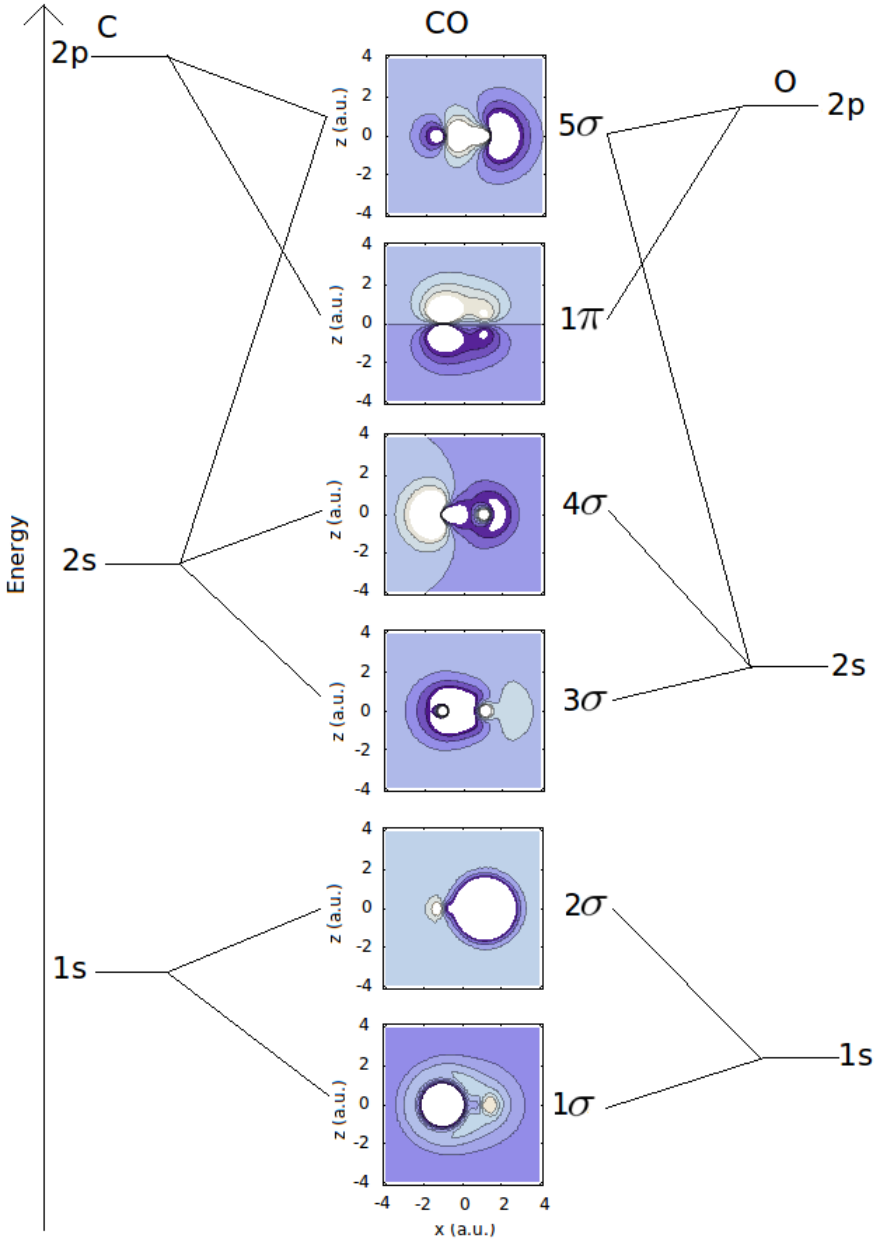

FIGURE 6.3: Schematic representation of atomic orbital contributions to bound molecular orbitals of CO. The molecular orbitals are presented in the position space representation. The figure demonstrates the relative difference in energy of the C and O atomic orbitals. As in previous figures, the LCAO procedure has been used with coefficients found from GAMESS-UK [13].

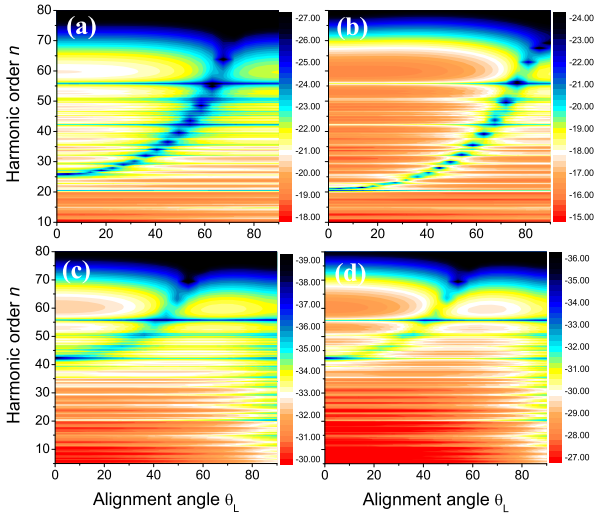

FIGURE 6.4: Harmonic spectra for N_2 subject to a linearly polarized laser field of frequency $\omega = 0.057$ a.u. and intensity $I = 4 \times 10^{14} Wcm^{-2}$. We display the harmonic spectra calculated using the length form, with the multi-electron corrections incorporated, and the harmonic spectra considering the corrections alone, a) and c), respectively. The harmonic spectra calculated using the velocity form, with the multi-electron corrections included, and from the corrections alone, are presented in panels b) and d), respectively. The angle θ_L is the angle between the internuclear axis and the laser field polarization.

length and velocity forms, it is seen that the corrections are many orders of magnitude smaller than the full spectra, which justifies neglecting the second order corrections. This is especially apparent when including the corrections in both the ionization and the recombination prefactor, where one observes a very large decrease in the yield, as displayed in Fig. 6.5. One observes that if the multi-electron corrections are included in the recombination prefactor only, and the ionization prefactor is set to unity, the corrections are always around four orders of magnitude smaller than the full spectrum. Interestingly, the only region where the multi-electron corrections are even close to the same order as the zeroth order term are at the harmonic minimum, occurring at approximately harmonic order $n = 27$ in the velocity form and harmonic order $n = 35$ in the length. However, to be consistent, the corrections should be included in both the ionization and recombination prefactors and in this instance they are completely negligible.

One should also note the suppression of the harmonic yield in the corrections at perpendicular alignment, $\theta_L = 90°$, as can be seen in Fig. 6.4 c) and d). This is due to the nodal structure in the lower lying σ_u orbitals, which are displayed in Fig. 6.2. There is not a complete suppression because the correction contains contributions from all of the lower lying orbitals of ungerade symmetry, including also the HOMO-1, $1\pi_u$ orbital.

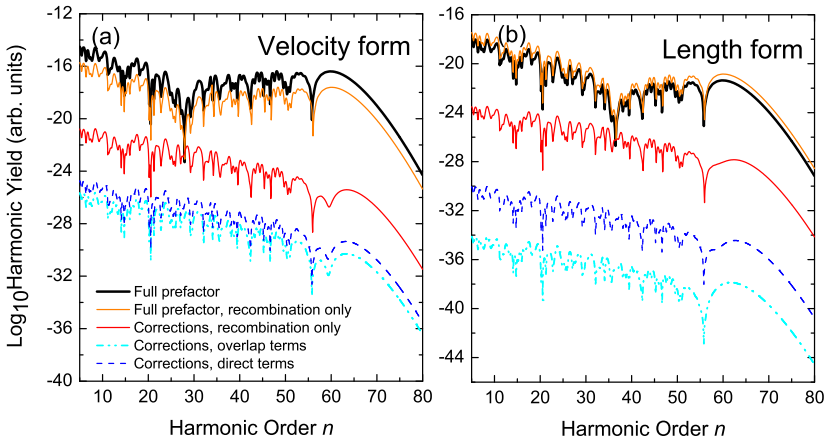

FIGURE 6.5: High-order harmonic spectra for N_2 in a driving field with the same parameters as in the previous figure, and an alignment angle $\theta_L = \pi/4$. The figure shows the overall spectra together with the first-order corrections taking into account only the direct or both the direct and overlap integrals. We consider both the ionization and recombination prefactors, or the recombination prefactor only (orange and red lines in the figure). Panels (a) and (b) give the velocity and length forms of the dipole operator, respectively.

The latter orbital does not have a nodal plane aligned with the field at these angles.

Fig. 6.5 also shows a comparison between the direct integrals, in Eq. (6.13), and overlap integrals, in Eq. (6.14) for the corrections. The two types of integral are compared when including the multi-electron corrections in both the ionization and recombination prefactors. We note that the overlap integrals are neglected in Fig. 6.4. It can be seen from the figure that this is justified because the overlap integrals are much smaller than the direct integrals in the length form and almost an order of magnitude smaller than the direct integrals in the velocity form.

The multi-electron first order corrections are also considered for a heteronuclear molecule, CO, where the static dipole moment will cause the second term on the right hand side of Eq. (6.4) to be non-zero. The harmonic spectrum obtained from an oriented CO molecule is shown in Fig. 6.6. Figure 6.6 a) and b) exhibit the full spectra, including corrections in the recombination prefactor, in the length and velocity forms, and Fig. 6.6 c) and d) display the spectra resulting from the corrections only in the length and velocity forms. There is a stark contrast in the overall spectrum from CO, compared to the overall spectrum of N_2. Most importantly, there is no visible two-center interference in either form. This is due to the ϑ term in Eq. (4.45), which is the equation that determines the two-center interference, based on the momentum space wavefunction. For homonuclear molecules, the atomic wavefunctions at each wavefunction cancel exactly, because $c^{(L)} = c^{(R)}$, such that $\vartheta = 0$ for p-type atomic orbitals and $\vartheta = \pi/2$ for s-type

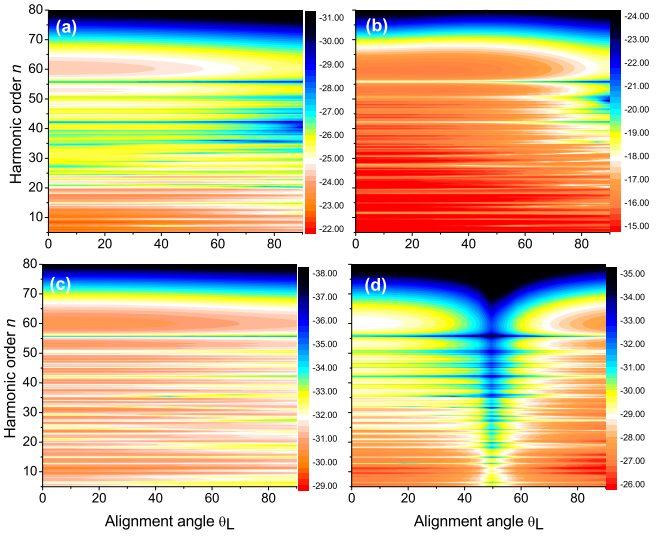

FIGURE 6.6: Harmonic spectra for CO with the same laser parameters as in Fig. 5.1. Presented are the harmonic spectra calculated using the length form, with the multi-electron corrections incorporated, and the harmonic spectra considering the corrections alone, a) and c), respectively. We also present the harmonic spectra calculated using the velocity form, with the multi-electron corrections included, and from the corrections alone, panels b) and d), respectively.

ortbitals. However, in heteronuclear molecules there are no such cancelations. Hence, the summation over α in Eq. (4.34) results in a variety of values of ϑ depending on the LCAO. This means there is no clear interference condition. Physically, this can be interpreted as the returning electron wavepacket recombining with unequal sized slits, resulting in a less distinct minimum.

Again, one sees that the contribution of the multi-electron effects in the length and velocity forms, Fig. 6.6 c) and d) respectively, are several orders of magnitude of smaller than those of the full harmonic spectrum, such that the zeroth order contribution in Eq. (6.3) is sufficient to model the spectra. However, in the velocity form corrections, in Fig. 6.6 d) there is a clear minimum located at an orientation angle of $\theta = 50°$ for all harmonics, which is, surprisingly, not present in the length form. This arises due to the lower lying σ_u molecular orbitals. Whereas the molecular orbital structure of the σ_u exhibits a nodal plane perpendicular to the internuclear axis in N_2, in CO, due to the static dipole moment, this molecular orbital does not have a definite symmetry and the nodal structure is distorted so that it is not a plane perpendicular to the axis. Instead, the minimum in the wavefunction forms a different angle to the axis. We do not see this minimum in the length spectrum for the corrections because they are dominated by the term which depends on the static dipole moment. However, in the velocity form, this term is vanishing.

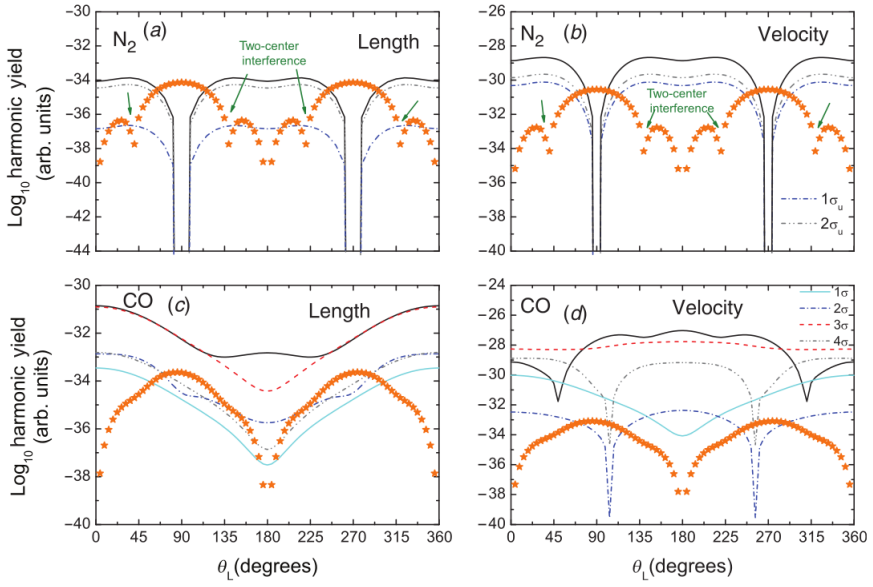

FIGURE 6.7: Contributions of the first order corrections to the 45th harmonic versus orientation angle θ_L for N_2 in the length and velocity form, a) and b), respectively, and CO in the length and velocity forms, c) and d), respectively. The two-center interference is labelled by the green arrows. The thick black line represents the contributions of the σ orbitals and the orange stars the contribution of the π orbital.

To understand the presence of lower lying orbitals on the corrections in more detail their individual contributions for a mid plateau harmonic, the 45th, are presented in Fig. 6.7. The spectra for N_2 in the length and velocity forms are presented in Fig. 6.7 a) and 6.7 b), respectively. The spectra exhibit inversion symmetry upon $\theta_L \rightarrow \theta_L + \pi$, as expected from the position space wavefunction symmetry. This is no longer the case for the CO spectra, in length and velocity forms, displayed in Fig. 6.7 c) and 6.7 d), respectively. This is because CO, unlike N_2, does not possesses inversion symmetry.

The presence of lower lying σ_u orbitals in the N_2 spectrum from the corrections leads to vanishing harmonic signal at angles $\theta = 90°$ and $\theta = 270°$ for both length and velocity forms. However, in the length form corrections for CO these cuts have completely disappeared. This is due to the static dipole moment in Eq. (6.4), which has the effect of washing out such features. In the velocity form, because the static dipole moment vanishes, the structures are not washed out. In fact, the minimum in the overall corrections, which includes the contribution of all orbitals, has been shifted from that occuring at $\theta_L = 90°$ and $\theta_L = 270°$ occuring in N_2, as we have seen in Fig. 6.6 d). These effects will be examined in more detail in Chapter 8.

6.3 Conclusions

The main conclusion to be drawn from this Chapter is that, if multielectron effects are considered statically by employing multi-electron ansatz, they lead to corrections which are several orders of magnitude smaller than the zeroth-order spectrum. This is observed regardless of whether the length or the velocity form of the dipole operator is used, or whether the corrections are embedded in both $a_{rec}(\mathbf{k}+\mathbf{A}(t))$ and $a_{ion}(\mathbf{k}+\mathbf{A}(t))$, or only in the recombination prefactor.

Hence, in order to incorporate multielectron effects in SFA-like models in an appropriate way, one must consider the dynamics of the target. Concrete examples are excitation, relaxation, electron orbits starting or finishing at different molecular orbitals, or the motion of the bound electrons [9, 24, 26, 68]. This chapter has shown that this holds for both homonuclear and heteronuclear molecules. This is very unexpected, especially when compared to the results in [64]. In this reference, far larger corrections have been observed for single atoms when multielectron effects has been introduced perturbatively in a static framework. This may be due to the fact that, therein, the acceleration form of the dipole operator is taken. This form emphasises spatial regions near the core.

The importance of dynamical effects in molecular high-harmonic generation is confirmed by results in which excitation or relaxation have been incorporated numerically. Therein, larger corrections have been observed [9, 24]. However, especially for N_2 these corrections still turned out to be only of a few percent as compared to the single-active electron results.

The importance of dynamic effects have also been shown in [24, 26, 68, 114], in the context of the multiconfiguration time-dependent HartreeFock (MCTDHF) theory for hypothetic molecules with two and four active electrons. Apart from that, ab initio methods also include strong couplings and quantum interference between energetically close orbitals. This has been, for instance, reported in [25] for N_2. Such couplings are not included in the present model.

On a more technical level, our results show that for the many-body perturbative corrections around the single-active-electron strong-field approximation, it is not really clear what form of the dipole operator one should take. In contrast, in the single-active-electron approximation, enough evidence has been provided in [48] that the velocity form yields the best agreement with the double-slit physical picture. In the present situation, however, the latter form exhibits a vanishing static dipole moment when considering the multi-electron corrections for heteronuclear molecules. Throughout the literature, it has been argued that overlap integrals are small and may be neglected without loss of information. In the velocity form we find they are around an order of magnitude smaller

than the direct integrals. In contrast, the length-form of the dipole operator leads to a non-vanishing static dipole moment for a heteronuclear molecule, and very small overlap integrals, in comparison to their direct counterparts.

Finally, even though the harmonic spectra due to the corrections are somewhat smaller than the spectra observed from the HOMO, one would expect to see their effect at molecular alignment angles where no harmonic signal is expected to be observed, such as when nodal planes are aligned parallel to the laser field polarization.

Chapter 7

Coherent superposition of molecular orbitals

In this Chapter, choosing the initial state of the molecule as a coherent superposition of orbitals is investigated as a method of imaging molecular orbital structure in the harmonic spectrum. Coherent superpositions have been used in high-order harmonic generation since the 1990s. In [136] a coherent superposition in H^+ was shown numerically to give rise to two distinct plateaus in the harmonic spectra. In [94], such a method was used for increasing the overall yield of the harmonic spectrum, as ionization procedes more easily from an excited state. Additionally, coherent superpositions have been proposed as a way of increasing the harmonic cutoff [97].

7.1 Theory

In the single-active-electron approximation, the wavefunction of a general multi-orbital system may be written as,

$$\mid \Psi_0\rangle = \sum_j C_j \mid \Psi_0^{(j)}\rangle \tag{7.1}$$

where C_j is the relative weight of each contributing orbital. Physically, this implies that the active electron is in either of the orbitals of our choice/ Following the formalism presented in Chapter 4 one obtains,

$$\mathbf{M}(\Omega) = \left| \sum_{j,\nu} \mathbf{M}_{j,\nu} + c.c. \right|^2 , \tag{7.2}$$

where,

$$\begin{aligned}\mathbf{M}_{j,\nu} &= -iC_j^* C_\nu \int_{-\infty}^{\infty} dt \int_{-\infty}^{t} dt' \int d^3\mathbf{k} a_{rec}^{*(j)}(\mathbf{k}+\mathbf{A}(t)) a_{ion}^{(\nu)}(\mathbf{k}+\mathbf{A}(t') \\ &\quad \times exp[iS_{j,\nu}(t,t',\mathbf{k})] + \mathbf{c.c.}, \end{aligned} \tag{7.3}$$

and the action reads,

$$S_{j,\nu}(t,t',\mathbf{k}) = S(t,t',\mathbf{k}) - E_j t + E_\nu t', \tag{7.4}$$

where E_j and E_ν correspond to the ionization energies of orbitals j and ν and $S(t,t',\mathbf{k})$ is defined in Eq. (5.21). In the above equations j and ν represent the initial and final orbitals respectively. Equation (7.3) represents a single electron multi-channel transition amplitude and gives rise to the possibility of ionization and recombination to different orbitals. This is also clear in Eq. (7.4), which is the multi-channel equivalent of the action in Eq. (5.20). The difference between the two actions is that in Eq. (5.20), the energy of the initial and final state are the same, whereas in Eq. (7.4) they may be different. The results presented in this Chapter have been published in [1].

7.2 Imprints of orbital structure

We employ a coherent superposition between the HOMO and the LUMO as the the initial state for an N_2^+ molecule. Ions are desirable as a target in harmonic generation because of the higher ionization potential which gives rise to a higher cutoff energy. However, the overall yield is reduced because the ionization step of the three step process is results in a lower transition probability, although this drawback has been shown to be overcome in atoms by using a coherent superposition of states [136]. One should also note that the LUMO of N_2^+, which is a π_g orbital, similar to that presented in Fig. 4.3 c), is negatively bound. This implies that ionization occurs by tunneling, which is the first step in the three step model. It is not possible to model over the barrier ionization within the three-step model formalism presented here.

Taking the weights C_j in Eq. (7.1) to be equal, the wavefunction for N_2^+ reads,

$$\mid \Psi_0\rangle = \frac{1}{\sqrt{2}} \left(\mid 3\sigma_g\rangle + \mid 1\pi_g\rangle\right) \tag{7.5}$$

in two dimensions and

$$\mid \Psi_0\rangle = \frac{1}{\sqrt{3}} \left(\mid 3\sigma_g\rangle + \mid 1\pi_{gx}\rangle + \mid 1\pi_{gy}\rangle\right) \tag{7.6}$$

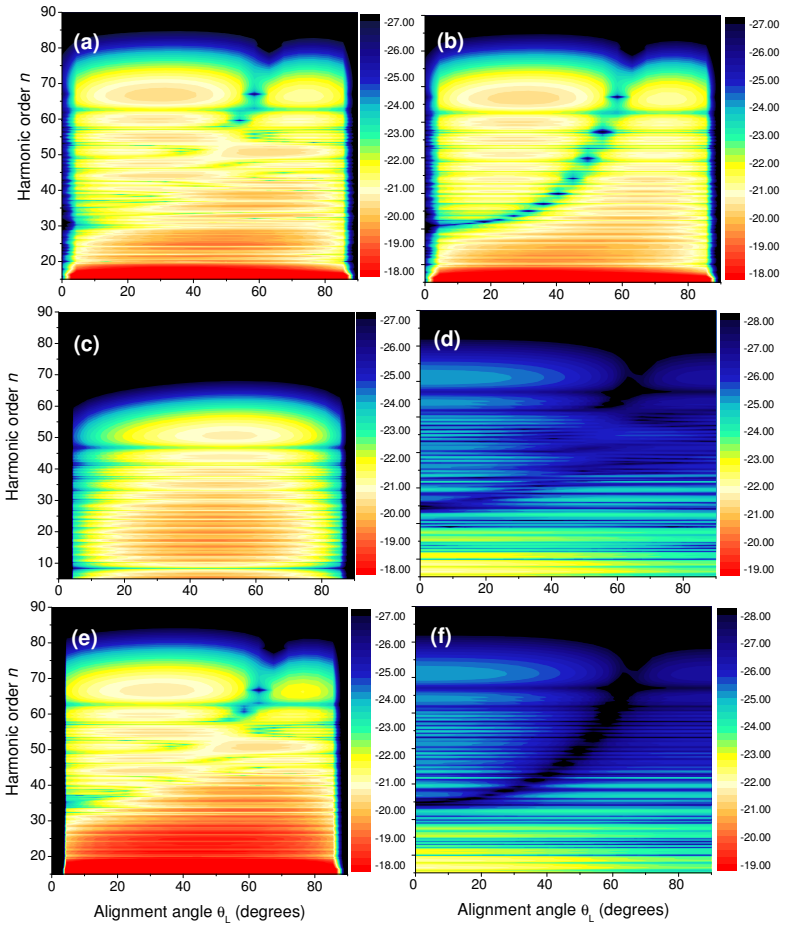

FIGURE 7.1: Harmonic spectrum as a function of alignment angle from an N_2^+ molecule prepared in a coherent superposition of the $3\sigma_g$ HOMO and $1\pi_g$ LUMO, subject to a linearly polarized laser field of frequency $\omega = 0.057$ a.u. and intensity $I = 4 \times 10^{14} W cm^{-2}$. The energies of the orbitals are $E_{3\sigma_g} = 1.12657012$ a.u. and $E_{1\pi_g} = 0.26871290$ a.u., respectively, with the internuclear distance taken as R=2.113 a.u. The results presented are for a two-dimensional calculation such that the $1\pi_{uy}$ orbital is neglected. a) Coherent sum of all contributions to the harmonic spectrum $\left|M_{3\sigma_g 3\sigma_g} + M_{1\pi_{gx} 1\pi_{gx}} + M_{1\pi_{gx} 3\sigma_g} + M_{3\sigma_g 1\pi_{gx}}\right|^2$, b) Contributions finishing at the $3\sigma_g$ orbital $\left|M_{3\sigma_g 3\sigma_g} + M_{3\sigma_g 1\pi_{gx}}\right|^2$, c) Contributions finishing at the $1\pi_g$ orbital $\left|M_{1\pi_{gx} 1\pi_{gx}} + M_{1\pi_{gx} 3\sigma_g}\right|^2$, d) Contributions starting at the $3\sigma_g$ orbital $\left|M_{3\sigma_g 3\sigma_g} + M_{1\pi_{gx} 3\sigma_g}\right|^2$, e) Contributions starting from the $1\pi_{gx}$ orbital $\left|M_{1\pi_{gx} 1\pi_{gx}} + M_{3\sigma_g 1\pi_{gx}}\right|^2$ and f) Considering the HOMO only $\left|M_{3\sigma_g 3\sigma_g}\right|^2$

in three dimensions. The LUMO of N_2^+ is degenerate, as we have seen for the HOMO-1 of N_2 in Chapter 5.

The harmonic spectrum obtained utilizing the two-dimensional coherent superposition is displayed in Fig. 7.1. The full spectrum containing all contributing channels as well as the spectra resulting from particular contributions are presented. Immediately, one

observes dramatic differences in the overall harmonic spectrum (Fig. 7.1 a)), which considers all contributing channels, compared to Fig. 7.1 f), which considers the $3\sigma_g$ molecular orbital only. The two-center interference in the spectrum expected when considering the $3\sigma_g$ orbital (Fig. 7.1 f)), is completely washed out, up to around harmonic $\Omega = 60\omega$, after which it is visible again. The physical mechanism leading to this interesting feature becomes apparent after observing the spectra from other contributions.

Figure 7.1 b) shows the spectra arising from processes which return to the $3\sigma_g$ orbital, but may ionize from either the $3\sigma_g$ orbital or the $1\pi_g$ orbital. A clear interference minimum is seen over all angles and harmonics up to the cutoff, and as the recombination step determines the interference, one can conclude that the blurring seen in Fig. 7.1 a) is due to the contribution of channels which return to the $1\pi_g$ orbital. At angles $\theta_L = 0°$ and $\theta_L = 90°$, there is a strong suppression in the HHG yield. This is due ionization from the $1\pi_g$ orbital, which has nodal planes aligned along the laser field polarization at these angles. Thus, as a consequence of the geometry of the orbital, tunnel ionization is greatly reduced. However, because the potential barrier of the $1\pi_g$ orbital is smaller than that of the $3\sigma_g$ orbital, at other angles the harmonic yield is higher. In comparison to Fig. 7.1 c), which considers processes which return to the $1\pi_g$ orbital, the cutoff is higher in Fig. 7.1 a), at around $\Omega = 80\omega$. This is due to recombination to the $3\sigma_g$ orbital, which has a higher ionization potential and therefore results in a higher cutoff harmonic in the spectrum. As the $1\pi_g$ orbital has a lower ionization potential, we see a lower cutoff in Fig. 7.1 c), in agreement with the cutoff law in Eq. (3.23). There is also no interference minimum in the spectrum from channels which return to the $1\pi_g$ orbital. This is because this minimum occurs at a harmonic frequency beyond the cutoff.

When observing Fig. 7.1 d), which displays processes starting at the $3\sigma_g$ molecular orbital, one immediately sees a drop in yield. This is due to the higher ionization potential in comparison to the $1\pi_g$ orbital. There is also an interference minimum occurring after $\Omega = 60\omega$, which has been washed out at lower harmonics due to recombination to the $1\pi_g$ orbital. Here we note that we have no cuts at $\theta = 0°$ rad and $\theta = 180°$ rad due to the process of ionization and recombination to the $3\sigma_g$ orbital. This washes out the cuts in the spectrum due to ionization from the $3\sigma_g$ orbital and recombination to the $1\pi_g$, which one would expect to see these angles due to the nodal planes in the $1\pi_g$ orbital.

Finally in Fig. 7.1 e), where processes starting at the $1\pi_g$ orbital only are considered, we see a spectrum which is very similar to Fig. 7.1 a). Thus, we conclude that in the overall spectrum, ionization from the $1\pi_g$ orbital is dominant, as expected due to the lower ionization potential. The main difference is that at angles $\theta_L = 0°$ and $\theta_L = 90°$ there is a slight distortion when all orbits are considered, which is due to the lack of nodal structure aligned along the field polarization direction in the $3\sigma_g$ orbital.

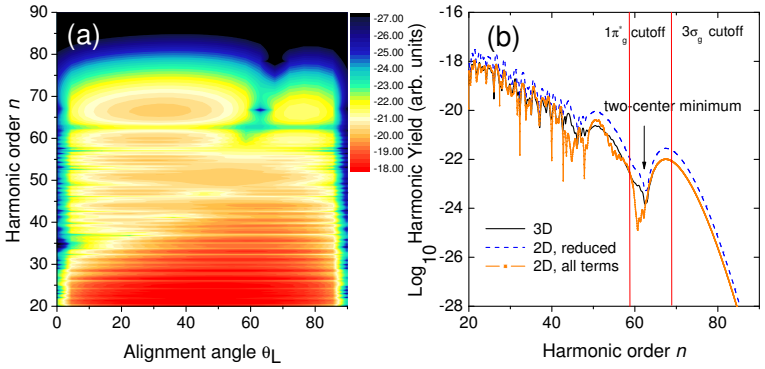

FIGURE 7.2: Harmonic spectrum from an N_2^+ molecule prepared in a coherent superposition of the $3\sigma_g$ HOMO and the degenerate $1\pi_{gx}$ and $1\pi_{gy}$ LUMO. The orbital energies are $|E_{3\sigma_g}| = 1.12657012$ a.u. and $|E_{1\pi_g}| = 0.26871290$ a.u., respectively, and an internuclear distance of R=2.113 a.u. is taken. a) Coherent sum of all contributions to the harmonic spectrum as a function of alignment angle, where the full three-dimensional calculation has been performed. b) Spectra for alignment and $\theta_L = \pi/3$ in where the signal has been calculated in 3D (black line), 2D (orange line) and reduced 2D (dashed line)[1]. For more details see text.

Three-dimensional calculations were also performed, for which the full spectrum is presented in Fig. 7.2 a). Some of the substructure present in the two dimensional spectrum, Fig. 7.1 a), is missing in the three-dimensional spectrum, Fig 7.2 a). This is due to the integration over the azimuthal angle, which causes many of the interfering contributions to vanish. This is investigated in more detail in Fig. 7.2 b), where the three-dimensional calculation is compared with its two-dimensional counterpart for an alignment angle of $\theta_L = 60°$. In the figure, the reduced two-dimensional spectrum is also presented. This is where the quantum coupling of the processes starting and returning to the HOMO or LUMO with those in which the electron is freed at one orbital and returns to the other are not included in the two-dimensional calculation. This coupling arises when taking a coherent summation to calculate the spectrum as in Eq. (5.18). This reduced spectrum exhibits less substructure than the two-dimensional spectrum, similar to that of the three-dimensional computation, indicating that integration over the azimuthal angle removes these interfering terms in the three-dimensional calculation.

7.3 Conclusions

In this Chapter, we investigated the interplay between the $3\sigma_g$ orbital and the $1\pi_g$ orbital by taking a coherent superposition of one electron states in N_2^+. We find that if the binding energies of the orbitals are far apart, as is the case in this investigation,

there will be different maximal kinetic energies associated with the processes in which the electron, upon return, recombines with each orbital. Recombination to the most loosely or deeply bound orbital will lead to a lower or higher cutoff energy, respectively. Apart from that, the potential barriers through which the electron tunnels in order to reach the continuum will be quite different for each orbital. In fact, ionization from the most loosely bound orbital implies a considerably narrower potential barrier. Hence, the contributions from the processes in which the electron starts at such an orbital will dominate.

One should note that, by taking a coherent superposition of states, we are allowing processes in which the electron ionizes from the LUMO and recombines to the HOMO, or vice versa. This coupling manifests itself in the spectrum as a group of high-frequency harmonics, beyond $= 60\omega$, for which the two-center interference pattern characteristic of the $3\sigma_g$ state is present. Below this frequency range, the spectrum exhibits a pattern which can be traced back to recombination with the $1\pi_g$ orbital. In contrast, if such processes were not allowed, the high-frequency harmonics would be much weaker, as they would be the result of ionization and recombination to the HOMO. Hence, they would play no important role in the spectrum.

Finally, in the three-dimensional computation, some substructure in the harmonic spectrum is lost. This is due to the integration over the azimuthal angle washing out some of the interfering processes. Specifically, this includes interference between trajectories starting and returning to the HOMO or LUMO, and those starting at one orbital and returning to the other.

Chapter 8

Asymmetry and nodal structures in heteronuclear molecules

So far, the influence of lower lying orbitals on the overall harmonic spectrum have been considered by a variety of methods. We have also seen interesting effects in the harmonic spectrum which depend ion the orbital geometry of the target system, such as nodal structures. Specifically, in Chapter 5 and chapter 6, the effect of nodal planes in $1\pi_u$ and $1\pi_g$ orbitals were seen at particular alignment angles in the harmonic spectrum. In Chapter 6 the nodal structure in the N_2 σ_u orbitals gave rise to a reduction in the harmonic signal at an alignment angle of $\theta_L = 90^\circ$. However, in CO, this suppression was shifted to an alignment angle of $\theta_L = 50^\circ$, as seen in Sec. 6.2. This suggests that if we can compare isoelectronic heteronuclear and homonuclear molecules the effects of nodal structures on the harmonic spectrum will be different. Additionally, two-center interference effects seen in N_2 are not visible in its isoelectronic heteronuclear counterpart, CO. Physically, this is due unequal contributions from each atom in the diatomic molecule.

These observations are now extended to other isoelectronic homonuclear and heteronuclear molecules. We consider the effects of the static dipole moment in heteronuclear molecules and the corresponding distortion of the molecular orbital on the harmonic spectrum, and in particular two-center interference effects and nodal structures. As well as this, the importance of incorporating the molecular structure into the action is investigated. This approach has been shown to reduce the definition of two-center interference [49], such that the minimum is not so pronounced. So far, in this thesis, this approach has not been applied to molecular systems with nodal structures. This work has been published in [3].

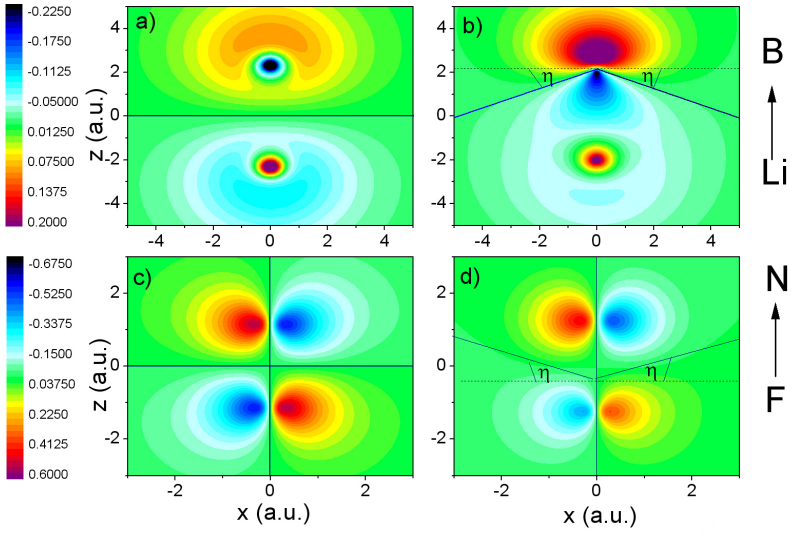

FIGURE 8.1: Position space wavefunctions of a) Be_2, b) LiB, c) O_2 and d) NF. The orbital wavefunstions are $2\sigma_u$, 4σ, $1\pi_g$ and 2π, respectively, with internuclear distances R^{Be_2}=4.642 a.u. R^{LiB}=4.642 a.u. R^{O_2}=2.280 a.u. and R^{NF}=2.485 a.u.. On the right hand side the direction of the static dipole moment is marked. Considering the HOMO only this is $d_{LiB}^{(HOMO)}$=0.9461 a.u. for LiB and $d_{NF}^{(HOMO)}$=0.1164 a.u. for NF

We take two isoelectronic pairs which exhibit at least one nodal structure in their HOMO. Taking Be_2 and LiB one sees the HOMO of Be_2 is a $2\sigma_u$, as shown in Fig. 8.1 a) and that of LiB is a 4σ, as shown in Fig. 8.1 b). The distortion of the nodal plane in Fig. 8.1 a) is displayed by the solid line in Fig 8.1 b) and forms an angle η with a line that bisects the internuclear axis at 90°. The static dipole moment in the LiB has distorted the nodal plane into a conical type structure. A molecule with two nodal planes, O_2, is displayed in Fig. 8.1 c) and its corresponding heteronuclear counterpart, NF, is exhibited in Fig. 8.1 d). The nodal plane along the z-axis in NF is unaffected by the static dipole moment, whereas along the x-axis the plane has been distorted into a nodal structure, forming an angle, η with the line perpendicular to the internuclear axis.

We also present the momentum space wavefunction which is used to calculate the ionization and recombination matrix elements in Fig. 8.2. It has already been seen, in Fig. 6.1 c), that despite the asymmetry of the position space wavefunction the absolute value of the momentum space wavefunction is symmetric. The same behaviour is seen from Fig. 8.2, where all panels are symmetric. However, the asymmetry of the position space wavefunctions in the position space wavefunctions of LiB and NF manifests itself in another way. First, recognising that the Fourier transform of a real odd function, such as the position space wavefunction of Be_2, will give a purely imaginary momentum

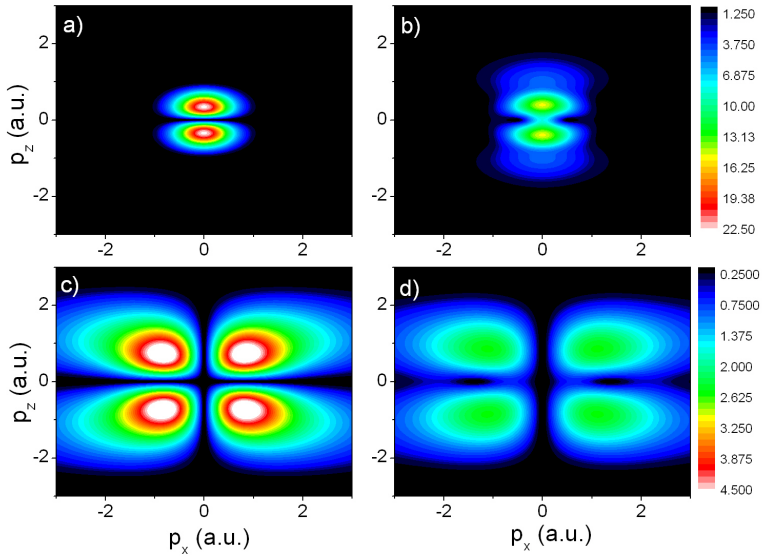

FIGURE 8.2: Absolute momentum space wavefunctions of a) Be_2, b) LiB, c) O_2 and d) NF. All other parameters are the same as those in the previous figure.

space wavefunction, one finds that the asymmetry of the wavefunction of LiB gives rise to a real component in the momentum space wavefunction. This real component is what causes the blurring along the p_x axis of the momentum space wavefunction of LiB, as shown in Fig. 8.2 b), which is not present in the homonuclear counterpart Be_2, shown in Fig 8.2 a). A similar argument holds when comparing the wavefunctions of O_2 and NF, as shown in Fig 8.2 c) and d), respectively. The position space wavefunction of O_2 is purely real and even, such that the Fourier transform will give a purely real momentum space wavefunction. However, an imaginary component, due to the asymmetry of the NF position space wavefunction will cause a blurring along the p_x axis. One should note the lack of blurring along the p_z axis of NF. This is because the symmetry upon reflection in the x-axis in the position space wavefunction is preserved as the static dipole moment only acts in the direction of the z-axis.

8.1 Signatures of nodal structures in high-order harmonic generation

We now compare the two approaches to incorporating the molecular structure into the transition amplitude. As discussed in Chapter 4 the structure may be incorporated into the prefactors or into the action. The first approach we call the standard SFA and the second approach the modified SFA. We will investigate the effect the different approaches

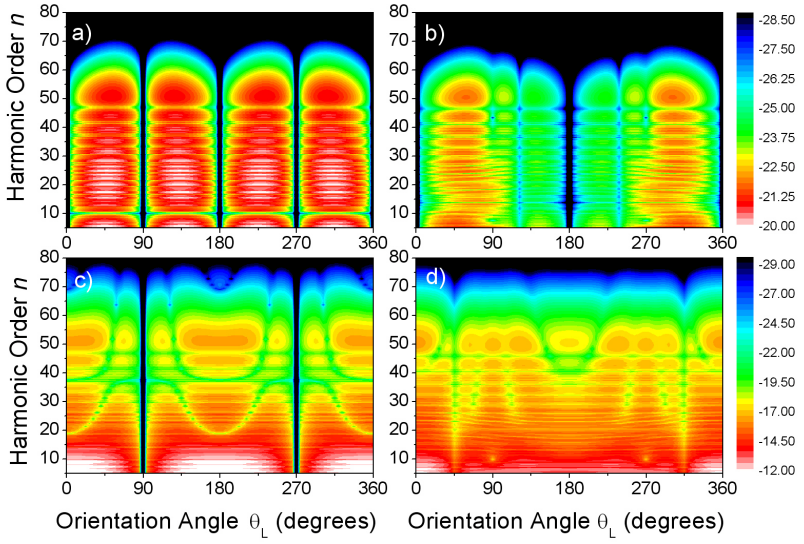

FIGURE 8.3: Harmonic spectra calculated using the HOMO of a) O_2, b) NF, c) Be_2 and d) LiB using a linearly polarized continuous wave laser field of frequency $\omega = 0.057$ a.u. and intensity I=$4 \times 10^{14} W cm^{-2}$, as a function of the orientation angle, θ_L. The orbital energis are $E_{1\pi_g}$=0.2446 a.u., $E_{2\pi}$=0.2246 a.u., $E_{2\sigma_u}$=0.2390 a.u. and $E_{4\sigma}$=0.1942 a.u., respectively.

will have on the suppression in the harmonic spectrum due to nodal strucutres in the molecular orbitals.

8.1.1 Standard SFA

The wavefunctions presented previously are employed when calculating the harmonic spectra from oriented moelcules in a linearly polarised laser field. For the moment we consider the standard SFA transition amplitude, as in Eq. (4.14), where the molecular structure is contained in the prefators. This implies that, physically, the ionized electron propagates from the geometric center of the molecule and returns to the geometric center. All results are calculated using the length gauge and the length form of the dipole operator. These results are presented in Fig. 8.3.

Immediately, one sees a series of cuts, that is, at certain alignment angles the intensity of the harmonic signal is vanishing. These are most prevalent for the homonuclear molecules, displayed in Fig. 8.3 a), which is the spectra from O_2, where they occur every $\theta_L = 90°$ and Fig. 8.3 c), which is the spectrum from Be_2, where they occur at $\theta_L = 90°$ and $\theta_L = 270°$. This can be related to the nodal planes present in the position space wavefunctions in Fig. 8.1 c) and Fig. 8.1 a), respectively. Whenever such a nodal plane is aligned with the field the harmonic signal is vanishing. Physically, this

is because, as we consider direct harmonics, where ionization and recombination occur at the center of the molecule, there is no electron density when such a nodal plane is parallel to the laser field polarization direction. Therefore, no ionization occurs, and as this is the first step of the three step process, which determines the harmonic yield, no harmonic signal is recorded.

Also, in the case of homonuclear molecules, clear interference minima are observed. In O_2 one sees zeroth order interference, which is angle independent interference occurring at the harmonic order n=10. This zeroth order interference arises due to the fact that the O_2 HOMO, which is a π_g orbital, is constructed entirely of p-type atomic orbitals, which causes the second term in Eq. (4.47) to vanish for zeroth order interference. However, one should note that effects in the low energy regions of the plateau are not well described because the strong-field approximation (SFA) is applicable to the higher energy regions. In Be_2, three orders of interference are observed, corresponding to κ= 0, 1 and 2. Such a large number of interference minima are observed due to the relatively large internuclear distance in Be_2

The situation in the case of NF, however, is modified, as shown in Fig. 8.3 b). The harmonic signal completely vanishes at orientation angles $\theta_L = 0°$, $180°$ and $360°$, because at these angles the nodal planes in the HOMO are the same as for O_2. However, due to the polar nature of these heteronuclear molecules, and an LCAO which no longer cancels out, the nodal planes at orientation angles $\theta_L = 90°$ and $270°$ are no longer present.

In fact, several differences with regard to the homonuclear case are observed. Firstly, the signal is no longer completely suppressed, but there is a distinct minimum which occurs at orientation angles $\theta_L = 123°$ and $238°$. There is also a second minimum, but not a cut, beyond harmonic n = 35, which occurs at the orientation angles $\theta_L = 90°$ and $270°$, that is, where the nodes were in the homonuclear molecule. We attribute this to the remnants of the nodal plane in its heteronuclear counterpart. Inspection of the position and momentum space wavefunction suggests that the polar nature of the heteronuclear molecules deforms the nodal plane such that, although there is no longer a node, there is a suppression which occurs at the angle to which the plane has been deformed, relative to the nodal plane in the homonuclear molecule. Hence, the probability density associated with the wavefunction is small, but nonvanishing. This leads to a minimum, but not a complete suppression in the spectrum. As the molecule is rotated the new minimum in the wavefunction is first experienced after $\theta_L = 90°$ but then occurs at the same angle before $\theta_L = 270°$. Therefore the spectra has reflectional symmetry about an orientation angle of $180°$.

There are in fact two types of nodal structures in the bound-state orbitals of molecules, which will lead to a strong suppression in the harmonic yield when such structures are parallel to the laser field polarization. The first type is caused by the nodes in the atomic orbitals at *each* ion, and is present at the same location for homonuclear molecules and their heteronuclear counterparts. The second type is due to the sum or subtraction of atomic orbitals at *different* centers within the linear combination of atomic orbital (LCAO) approximation. Both types of minima are present for homonuclear molecules. For their heteronuclear counterparts, however, the asymmetry of the molecule eliminates the latter nodes. This implies that the imprints of the first type of nodes in the harmonic spectra are common to isoelectronic homonuclear and heteronuclear molecules, and could in principle be observed in both cases.

Now observing the spectrum for Be_2 , displayed in Fig. 8.3 c), one may identify nodes at $\theta_L = 90°$ and 270°, as one would expect by observing the position and momentum space wavefunctions. In the spectrum from the heteronuclear counterpart LiB, presented in Fig. 8.3 d), these nodes have been replaced by minima at $\theta_L = 45°$ and 315° , for the same reasons as described above.

The two-center interference minima in the heteronucelar molecules is also much less distinct than that of the homonucelar moelcules. The angular independent zeroth order suppression in O_2 is lost in NF, whereas comparing the two-center interference patterns in the spectrum from Be_2 and LiB one observes that, in the heteronucelar case, the patterns are blurred and vanish completely at certain angles. This is to be expected and, as explained in Sec. 6.2, is due to the asymmetry of the HOMO. Also, one should note that in the case of LiB there are only two orders of interference minima, $\kappa = 0, 1$, compared to three orders in Be_2. This is due to the slightly lower ionization potential and therefore lower cutoff energy, implying that the $\kappa = 2$ interference will occur beyond the cutoff, as well as the different s-p mixing, arising from the asymmetric nature of the molecule. This can be seen in more detail from Fig. 8.4.

We also compare the spectra arising from s-type orbitals and p-type orbitals of Be_2, displayed in Fig. 8.4 a) and b). It can be seen that the contribution from p-type orbitals is significantly less than that of the s-type orbitals. However, they are still important, as can be seen by the more defined minima in Fig. 8.3 c) compared to Fig. 8.4 a). However, in LiB, the p-type orbitals are of a similar magnitude, as can be seen comparing harmonic spectra from s and p-type orbitals in Fig. 8.4 c) and d), respectively, and have a more pronounced effect on the overall spectrum in Fig. 8.3 d). The relative prominence of the p-type molecular orbial is also clear in the position space wavefunction in Fig. 8.1 b). When considering only the s-type atomic orbitals in

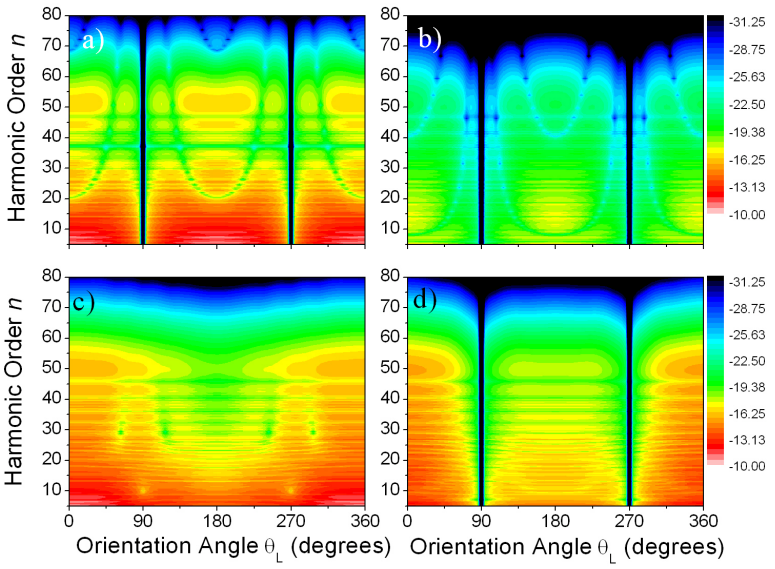

FIGURE 8.4: Harmonic spectra for Be_2 and LiB considering s-type atomic orbitals, a) and c) respectively, and p-type orbitals, b) and d) respectively, using the same laser and molecular parameters as in the previous figure.

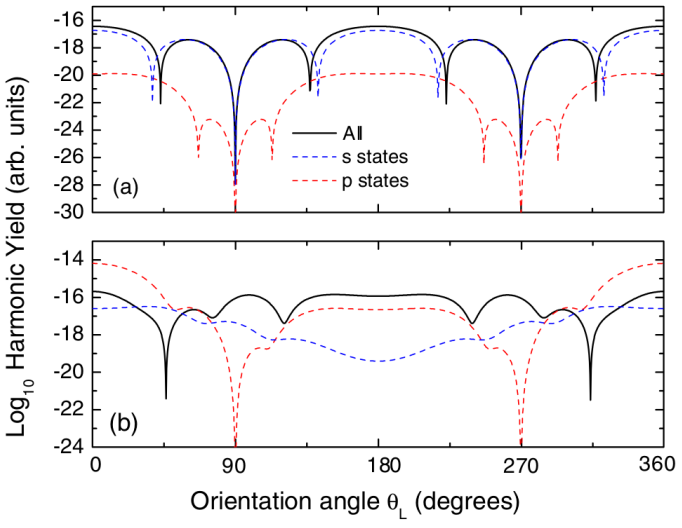

FIGURE 8.5: Contributions of the s, p and all atomic orbitals to the yield of the 25th harmonic of a) Be2 and b) LiB as functions of the orientation angle θ_L. All parameters are the same as in the previous figure.

a homonuclear molecule Eq. (4.47) takes the more simple form,

$$n_s = \frac{E_0}{\omega} + \frac{2\kappa^2\pi^2}{\omega R^2 cos^2(\theta_L)}, \tag{8.1}$$

and for p-type atomic orbitals,

$$n_p = \frac{E_0}{\omega} + \frac{(2\kappa+1)^2\pi^2}{\omega R^2 cos^2(\theta_L)}, \tag{8.2}$$

The effects of s-p mixing are also displayed in Fig. 8.5 a) and b) for a fixed mid-plateau harmonic. The figure clearly shows that, for Be_2 , the s-type orbitals dominate and the main effect of the p-type orbitals is to introduce a small shift in the interference minima. On the other hand, for LiB, the overall maxima and minima are considerably altered by s p mixing. In the figure, one can also see that the nodal planes occurring at orientation angles $\theta_L = 90^\circ$ and 270° in $Be2$, are shifted by the contribution of the s-type orbitals in LiB.

8.1.2 Importance of exchange harmonics

So far, the molecular structure has been incorporated into the ionization and recombination prefactors. However, as discussed in Sec. 4.52, when using saddle point methods, the assumption that the prefactors are slowly varying may not be valid. Hence, a more accurate approach is to incorporate the molecular structure into the action. The differences in the two approaches can be seen in Fig. 8.6. Considering first Fig. 8.6 a), which compares the two approaches for N_2, one observes that qualitatively there is very little difference between the results. The features due to the nodal structures occur at the same angles and at these angles the contribution is vanishing. Quantitatively, the contribution of the harmonics arising from incorporating the molecular structure into the action, is slightly less. Nonetheless, the interpretation of the physical mechanism giving rise to the suppression is different. When the molecular structure is incorporated into the prefactors, at the angles where the suppression occurs, these prefactors are vanishing, implying that reduced harmonic signal is because of the vanishing electron density. However, when considering the modified action, there are four contributions to the overall harmonic spectrum. It is the quantum interference of all of these processes which gives rise to the nodal structure. The phase accumulated from different nodes of the π_g orbital are different, due to the opposite parity of the nodes in the wavefunction, giving rise to a π phase shift, resulting in the cancellation, which is also given as the reason for the suppression in the N_2 π_u molecular orbital [23]. In fact, one finds that if

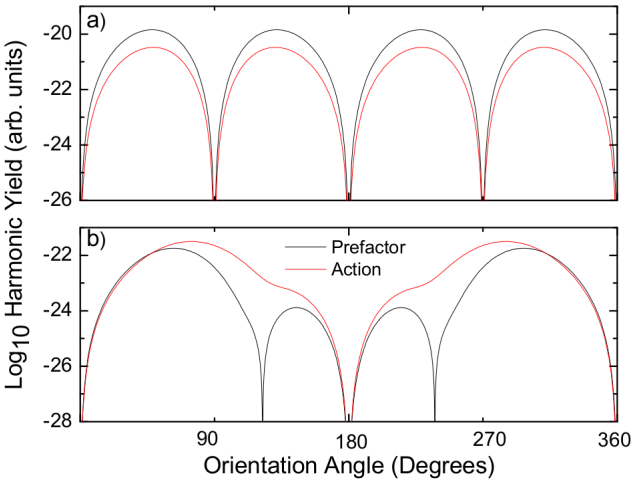

FIGURE 8.6: Comparison of the harmonics calcualted where the molecular structure is incorporated into the prefactors, and where the molecular structure is incorporated into the action, for N_2 and NF, displayed in a) and b) respectively. We consider the intensity of the 25th harmonic versus the orientation angle. The laser and molecular parameters are the same as those in the previous figure.

the exchange harmonics are removed from the computation the minima at orientation angles $\theta_L = 90°$ and $\theta_L = 270°$ are no longer present.

The two approaches to calculating the harmonic spectrum for NF, shown in Fig. 8.6, give qualitatively different results. Most significantly, one sees that the harmonics calculated by incorporating the molecular structure into the action have a much less distinct suppression. The lack of suppression in the modified action case can be viewed as the result of slightly amplitudes between contributing trajectories. For the homonuclear case, at the orientation angles where such nodal features occur, trajectories are exactly out of phase, and have exactly the same amplitude, giving rise to a complete suppression, but in the heteronuclear case, due to the asymmetry of the HOMO, there is no longer an exact cancellation.

8.2 Conclusions

In this Chapter, we investigated the dependence of the high-order harmonic spectra on the orientation angle between the diatomic molecules and the laser field polarization, for isoelectronic pairs consisting of a homonuclear and a heteronuclear molecule. We employed a single active electron approximation, using the HOMO as the active orbital, within the strong-field approximation.

We find that nodal structures in a heteronuclear molecule can be related to the nodal planes in an isoelectronic homonuclear molecule. The distorted wavefunction in the

heteronuclear molecules will cause suppression in the spectrum, due to nodal structures, to occur at different angles compared to those from a homonuclear molecule. Hence, in principle, the latter can be used as a reference point in order to understand the behavior of the former, by using high-order harmonic generation. The shifts in the nodal planes present for homonuclear molecules due to the distortions in the wavefunctions, or the absence thereof, can be mapped into features in the high-harmonic spectra. This is a very good example of how symmetry breaking in a molecule reflects itself in the harmonic spectra, and may shed some light in the imaging of heteronuclear molecules. Another example of this are the even harmonics, which are present in oriented heteronuclear molecules (for a recent example see [77]).

In general, the asymmetry of the heteronuclear molecular orbitals also leads to some blurring in the interference patterns caused by high-harmonic emission at spatially separated centers in the molecule. Furthermore, depending on the molecule, s-p mixing will be different. This will lead to shifts in the energy positions of the two-center patterns. On a more technical level, we have also been able to map the symmetry or asymmetry of the molecular orbitals in position space to properties of their momentum-space counterparts.

Finally, we would like to comment on the fact that, throughout this Chapter, the Stark shifts in the ionization potentials of the molecules have been neglected in the strong-field approximation. The first-order shifts lead to binding energies which depend on the alignment angle. In fact, if the static dipole moment is oriented parallel or antiparallel to the laser-field polarization, the bound-state energies will decrease, or increase, respectively. This would imply a shift in the cutoff towards higher energies in the antiparallel case. The second-order shifts are much smaller and do not depend on the alignment angle. For homonuclear molecules, the first-order Stark shift is vanishing, so that orientation effects can be neglected. For heteronuclear molecules such as NF, for which the static dipole moment is small, the Stark shift is expected to be negligable. For LiB, however, the static dipole moment is much larger. Hence, further distortions in the spectra due to the above-mentioned effect are expected.

Chapter 9

Coupled coherent states

The work presented up to this stage has been based upon the strong-field approximation (SFA), which is a very powerful approach and allows an almost entirely analytic treatment of strong field phenomena. It also provides a transparent interpretation of such phenomena in terms of interfering trajectories. However, as we have seen, in many cases needs to be modified to include, for example, multi-electron effects. Previous Chapters have modified the SFA in a variety of ways in order to incorporate multi-electron effects, as well as investigating the importance of nodal structures on the harmonic spectrum. However, the SFA makes a series of physical approximations that are not always well justified. These issues include,

- The SFA neglects the binding potential when the electron is in the continuum, which means that the field-dressed momentum is conserved in the SFA. This leads to some important electron trajectories not being incorporated into SFA calculations [84], causing the SFA to misinterpret certain experimental features where such trajectories are important [82, 83].
- The orthogonality of the ground state and the continuum state is destroyed because of approximations imposed upon the continuum states. The continuum state has been replaced by a field dressed plane wave. In the context of high harmonic generation (HHG), this leads to translational variance and artifacts in the harmonic spectrum when using the length form of the dipole operator [2, 49, 108].
- The SFA is not gauge invariant. This means that when modeling interference effects in HHG from diatomic molecules the length gauge must be chosen because such interference patterns are not present in the velocity gauge [27, 49, 108].
- The bound state within the SFA is static and also field free. Therefore important effects such as core hole dynamics are neglected. Therefore, modeling dynamic

multi-electron effects requires the use of TDDFT or MCTDH, where much of the physical interpretation is lost.

We require a trajectory based method, which has the potential to include all of the above effects, but which is not numerically too expensive. Classical trajectory based methods, although useful when looking at NSDI, cannot reproduce HHG spectra very well as they contain no phase information. Semi-classical approaches, such as Herman-Kluk [88], have been shown to accurately reproduce the HHG cutoff and plateau, and fully include the Coulomb potential. However, so far they do not simulate the recollision picture, because ionisation is neglected [89, 121]. In addition, Herman-Kluk only includes local quantum coupling between a semi-classical trajectory and its nearest neighbour and also cannot describe tunneling ionisation.

In this Chapter, a method is proposed which is somewhere between the semi-analytical SFA and the highly numerical approaches of TDDFT and MCTDH. Recently, Shalashilin and Child developed the coupled coherent state (CCS) approach [122, 137–141]. The method exploits the properties of Gaussian wavepackets, which are guided by classical trajectories governed by Hamilton's equations, as a basis for solving quantum mechanical equations. The initial state may be chosen by randomly selecting trajectories in phase space using Monte-Carlo sampling. This facilitates very favourable scaling with dimensionality, such that, rather than the exponential scaling $N = l^M$, where N is the number of grid points, M is the number of degrees of freedom and l is the number of grid points per degree of freedom, seen when solving the TDSE numerically, the CCS method scales as $N \propto M^2$. Therefore this scheme is suitable for the modeling large systems. In addition to this, the coherent state basis set may be chosen such that it is in the dynamically most important regions, simplifying computations by reducing the number of trajectories required.

The work presented here is still in preparation [142]. We will now give an overview of the main theory behind the CCS method. For a review see [139].

9.1 Model

A coherent state, is an eigenstate of the annihilation operator, such that,

$$\hat{a} \mid \mathbf{z}\rangle = z \mid \mathbf{z}\rangle, \tag{9.1}$$

and

$$\langle \mathbf{z} \mid \hat{a}^\dagger = \langle \mathbf{z} \mid \mathbf{z}^*, \tag{9.2}$$

where the annihilation and creation operators, in terms of position and momentum operators, are given by,

$$\hat{a} = \left(\frac{\gamma}{2}\right)^{1/2} \hat{q} + \frac{i}{\hbar}\left(\frac{1}{2\gamma}\right)^{1/2} \hat{p}, \tag{9.3}$$

and

$$\hat{a}^{\dagger} = \left(\frac{\gamma}{2}\right)^{1/2} \hat{q} - \frac{i}{\hbar}\left(\frac{1}{2\gamma}\right)^{1/2} \hat{p}, \tag{9.4}$$

respectively, where γ is a width parameter.

A coherent state expressed in phase space, where $\mathbf{q}$ and $\mathbf{p}$, represent the position and momentum, is given by,

$$\mathbf{z} = \left(\frac{\gamma}{2}\right)^{1/2} \mathbf{q} - \frac{i}{\hbar}\left(\frac{1}{2\gamma}\right)^{1/2} \mathbf{p}, \tag{9.5}$$

and its complex conjugate by,

$$\mathbf{z}^{*} = \left(\frac{\gamma}{2}\right) \mathbf{q} + \frac{i}{\hbar}\left(\frac{1}{2\gamma}\right)^{1/2} \mathbf{p}. \tag{9.6}$$

In coordinate representation, the coherent state $\mid \mathbf{z}\rangle$, is a Gaussian wavepacket centered at $\mathbf{q}$, with momentum $\mathbf{p}$, reads,

$$\langle \mathbf{x} \mid \mathbf{z}\rangle = \left(\frac{\gamma}{\pi}\right)^{3/4} \exp\left(\frac{\gamma}{2}(\mathbf{x}-\mathbf{q})^2 + i\mathbf{p}\cdot(\mathbf{x}-\mathbf{q}) + \frac{i\mathbf{p}\cdot\mathbf{q}}{2}\right). \tag{9.7}$$

9.1.1 Static basis representation

We wish to solve the time dependent Schrödinger equation (TDSE),

$$i\frac{d \mid \Psi(t)\rangle}{dt} = \hat{H}(t) \mid \Psi(t)\rangle \tag{9.8}$$

in a coherent state basis, where $\hat{H}$ is the Hamiltonian of the system. Using the identity operator,

$$\hat{I} = \frac{1}{\pi}\int d^2 z \mid \mathbf{z}\rangle\langle \mathbf{z} \mid, \tag{9.9}$$

where the state $\mid \mathbf{z}\rangle$ is static, the TDSE may be written as,

$$\frac{d\langle \mathbf{z} \mid \Psi(t)\rangle}{dt} = -i\int \langle \mathbf{z} \mid \hat{H}(t) \mid \mathbf{z}'\rangle\langle \mathbf{z}' \mid \Psi(t)\rangle \frac{d^2\mathbf{z}}{\pi}. \tag{9.10}$$

In order to establish a numerically solvable scheme, one may use a discretized form of the identity operator,

$$\hat{I} = \sum_j \mid \mathbf{z}_j\rangle\langle \mathbf{z}_j \mid \frac{\Delta^2 \mathbf{z}}{\pi}, \tag{9.11}$$

or, an alternative identity operator which preserves the norm, $\langle \Psi \mid \Psi \rangle$, much more consistently,

$$\hat{I} = \sum_{j,k} \mid \mathbf{z}_j \rangle (\Omega^{-1})_{j,k} \langle \mathbf{z}_k \mid \tag{9.12}$$

where $\Omega_{j,k} = \langle z_j \mid z_k \rangle$. This leads to the discrete form of Eq. (9.10)

$$\frac{d\langle \mathbf{z}_i \mid \Psi(t) \rangle}{dt} = -i \sum_{j,k} \langle \mathbf{z}_i \mid \hat{H}(t) \mid \mathbf{z}_j \rangle (\Omega^{-1})_{j,k} \langle \mathbf{z}_k \mid \Psi(t) \rangle \tag{9.13}$$

9.1.2 Dynamic basis representation

A more sophisticated approach than the static scheme detailed in the previous section, is to use a dynamic basis. This facilitates the use of Monte-Carlo sampling which greatly reduces the numerical cost from exponential scaling with dimensionality.

The coherent states are allowed to move along classical trajectories determined by Hamilton's equations,

$$\frac{d\mathbf{z}}{dt} = -\frac{i}{\hbar} \frac{d\mathbf{H}_{ord}(\mathbf{z}, \mathbf{z}^*)}{d\mathbf{z}^*} \tag{9.14}$$

and,

$$\frac{d\mathbf{z}^*}{dt} = -\frac{i}{\hbar} \frac{d\mathbf{H}_{ord}(\mathbf{z}, \mathbf{z}^*)}{d\mathbf{z}}, \tag{9.15}$$

where $\mathbf{H}_{ord}$ is ordered Hamiltonian, in which the position and momentum co-ordinates have been rewritten in terms of annihilation operators and then reordered, $\mathbf{H}(\mathbf{p}, \mathbf{q}) \equiv \mathbf{H}(\hat{a}, \hat{a}^\dagger) = \mathbf{H}_{ord}(\hat{a}^\dagger, \hat{a})$, such that,

$$\langle \mathbf{z}_j \mid \mathbf{H} \mid \mathbf{z}_k \rangle = \Omega_{j,k} H_{ord}(z_j, z_k). \tag{9.16}$$

It can be seen that Eq. (9.14) and Eq. (9.15) are diagonal, which means that there is no interference between different coherent states and that the equations are classical. By restricting the motion of the coherent states to move along the classical trajectories defined in Eq. (9.14) and Eq. (9.15), as well as expressing the coefficients as

$$\langle \mathbf{z} \mid \Psi \rangle = C(\mathbf{z}, t) \exp[\frac{i}{\hbar} S_z], \tag{9.17}$$

where,

$$S_z = \int \left(\frac{i\hbar}{2} (z^* \frac{d\mathbf{z}}{dt} - \frac{d(\mathbf{z})^*}{dt} \mathbf{z}) - H_{ord}(\mathbf{z}, (\mathbf{z})^*) \right) dt, \tag{9.18}$$

the coefficients $C(\mathbf{z}, t)$ can be calculated by solving,

$$\frac{dC(\mathbf{z}, t)}{dt} = -\frac{i}{\hbar} \int \langle \mathbf{z} \mid \mathbf{z}' \rangle \delta^2 \mathbf{H}_{ord}(\mathbf{z}^*, \mathbf{z}') C(\mathbf{z}'(t)) \exp[\frac{i}{\hbar} (S_{z'} - S_z)] \frac{d^2\mathbf{z}'}{\pi} \tag{9.19}$$

FIGURE 9.1: Figure representing the evolution of the coherent state basis. A wavefunction at time $t = 0$, $\Psi(0)$, is constructed from the coherent states with position and momentum $q_i(0)$ and $p_i(0)$ and with an initial coefficient $C_i(0)$. The coherent state basis moves along classical trajectories, governed by Hamilton's equations, with positions $q_i(t)$ and momentum $p_i(t)$ and enables us to construct a wavefunction at time t with a coefficient $C_i(t)e^{iS/\hbar}$. From reference [15]

.

where,

$$\delta^2 H_{ord}(\mathbf{z}^*, \mathbf{z}') = \frac{1}{2}\frac{\delta^2 \mathbf{H}_{ord}}{\delta \mathbf{z}^2}(\mathbf{z} - \mathbf{z}')^2 + ... \tag{9.20}$$

Equation (9.19) is the working equation of the coupled coherent state (CCS) method and includes coupling between different coherent states. One sees from Eq. (9.20) that for coherent states that are close, $\mathbf{z} = \mathbf{z}'$, Eq. (9.19) will vanish whereas for coherent states which are far apart the overlap $\langle z \mid z' \rangle$ will also cause Eq. (9.19) to be vanishing which means that coupling between coherent states is always sparse, which makes the method numerically less expensive. The dynamic nature of the coherent states is presented in Fig. 9.1.

To obtain the discrete formalism, using the identity operator in Eq. (9.12) one obtains,

$$\frac{dC_k}{dt} = -\frac{i}{\hbar}\sum_{i,j}\Omega_{i,j}\delta^2 \mathbf{H}_{ord}((\mathbf{z})^*_k, \mathbf{z}_i)(\Omega^{-1})_{i,j}C_j \exp[\frac{i}{\hbar}(S_j - S_k)], \tag{9.21}$$

with the coefficient,

$$\langle \mathbf{z}_k \mid \Psi \rangle = C_k \exp(\frac{i}{\hbar}S_k) \tag{9.22}$$

In this work, a Hydrogen atom is considered, in an intense electric field $\mathbf{E}(t)$. The Hamiltonian is taken in the length gauge. In this instance the ordered Hamiltonian will read as,

$$\mathbf{H}_{ord} = \frac{m\omega}{4}((\mathbf{z})^2 - 2(\mathbf{z})^*\mathbf{z} + ((\mathbf{z}^*)^2)) + \mathbf{E}(t)\rho - \frac{1}{\rho}erf(\rho), \tag{9.23}$$

where

$$\rho = \frac{\mathbf{z}_i + \mathbf{z}_j^*}{2\gamma}. \tag{9.24}$$

9.1.3 Assessing the dipole operator

As detailed in Sec. 3.2, in order to calculate the harmonic spectrum we must calculate the expectation value of the dipole moment. This can take either the length, velocity or acceleration form. Using the identity operator in Eq. (9.12) to calculate the expectation value of the dipole moment of arbitrary form in the coherent state basis gives,

$$\langle \Psi(t) \mid \hat{d} \mid \Psi(t) \rangle = \sum_{j,k,l,m} \langle \Psi(t) \mid \mathbf{z}_j \rangle (\Omega^{-1})_{j,k} \langle \mathbf{z}_k \mid \hat{d} \mid \mathbf{z}_l \rangle (\Omega^{-1})_{l,m} \langle \mathbf{z}_m \mid \Psi(t) \rangle \tag{9.25}$$

Therefore, one must calculate the matrix element,

$$d_{k,l} = \langle \mathbf{z}_k \mid \hat{d} \mid \mathbf{z}_l \rangle, \tag{9.26}$$

where in the length form,

$$\hat{d} = \hat{q}, \tag{9.27}$$

in the velocity form

$$\hat{d} = \hat{p}, \tag{9.28}$$

and in the acceleration form

$$\hat{d} = d\hat{V}/d\hat{q}, \tag{9.29}$$

In the length form, Eq. (9.26) then becomes

$$d^l_{k,l} = (\mathbf{z}_k^* + \mathbf{z}_l) \langle \mathbf{z}_k \mid \mathbf{z}_l \rangle, \tag{9.30}$$

in the velocity form it becomes,

$$d^v_{k,l} = (-\gamma(\rho - \mathbf{q}_l) + i\mathbf{p}_l) \langle \mathbf{z}_k \mid \mathbf{z}_l \rangle, \tag{9.31}$$

and in the acceleration form,

$$d^a_{k,l} = \left(2\sqrt{\frac{\gamma}{\pi}} \frac{e^{-\gamma\rho^2}}{\rho} - \frac{1}{\rho^2} erf(\sqrt{\gamma}\rho) \right) \langle \mathbf{z}_k \mid \mathbf{z}_l \rangle. \tag{9.32}$$

The derivations for the above expressions are presented in Appendix G.

9.2 Sampling

An accurate choice of initial conditions is extremely important in obtaining reliable converged results. Popular approaches are to use a Wigner distribution, or to choose the initial conditions based on the Bohr model of the Hydrogen atom. In classical trajectory Monte Carlo (CTMC) simulations, the importance of averaging over many ensembles is paramount. Unphysical features, not reproduced by quantum simulations or experiment, appear in the harmonic spectrum if only a single ensemble is taken, whereas the ensemble average reproduces the correct features [143]. Much semi-classical work has placed the initial wavepacket at the quiver distance, thus neglecting the ionization step of the harmonic generation process [89, 90, 121], because modelling tunneling semi-classically is not possible. In terms of reproducing the universal features of harmonic spectra this procedure is legitimate, although not modelling the ionization step will affect the yield of the emitted harmonics and the cutoff harmonic order. Although in principle tunneling can be modelled by the CCS approach starting trajectories at the quiver distance allows us to study the recombination step in detail and compare to published results.

9.3 Results

We present results for atomic hydrogen, of ionization potential $I_p = 0.5$ a.u., exposed to a trapezoidal laser field of the form,

$$\mathbf{E}(t) = \begin{cases} E_0 \frac{t}{T} \sin(\omega t) & \text{if } t \leq T\hat{e}_z \\ E_0 \sin(\omega t) & \text{if } T < t \leq (N-1)T\hat{e}_z \\ E_0 \left(1 - (\frac{t}{T} - (N-1)\right) \sin(\omega t) & \text{if } (N-1)T < t \leq NT\hat{e}_z \end{cases}$$

This pulse has a period of T, is $N = 5$ cycles long, and has a one cycle ramp up and one cycle ramp down.

To begin with, we placed all trajectories around the nucleus using a Gaussian distribution and compared results to a one-electron TDSE solver in the Qprop package [144]. We found that in the CCS calculation a large 'drift' in the dipole moment, when taken in the length form, was observed compared to that of Qprop result (not shown). This is due to trajectories which irreversibly ionize in the CCS calculation. In the length form of the dipole operator, regions far from the core are over emphasised. In addition, the Qprop TDSE solver has an imaginary absorbing potential boundary, such that charge density far from the boundary is removed. Based on numerical studies, we know that

this drift in the dipole moment will lead to noise in the harmonic spectrum and we do not see a cutoff [104]. An example of this is shown in Fig. **??**.

We also found that bound trajectories which do not leave the vicinity of the atom increase the harmonic cutoff and lead to a lot of numerical noise. One option is to therefore discard these highly oscillatory bound trajectories and the irreversibly ionized trajectories from the calculation should they arrise. Physically, this would imply that only trajectories which ionize and return to the core are included, in the spirit of the three step model. However, we still encountered a lot of numerical noise, and we found that as more trajectories are added to the simulation the cutoff increases.

Starting the trajectories away from the nucleus, around the quiver distance, which is the maximum electron excursion during one field cycle, simplifies the problem considerably. This is because accurate modelling of the initial bound state, and tunneling, may be neglected [89, 90, 121]. Using this approach, we expect the cutoff not to follow the usual law, in Eq. (3.23), but for the cutoff harmonic to be located at,

$$n_{max} = \frac{I_p + 2U_p}{\omega}. \tag{9.33}$$

Using only five trajectories, from a batch of 3000, and starting with a one-dimensional calcultion, we obtain the spectrum in Fig. 9.2. The electron is started from an unbound location, situated approximately at the quiver distance in the z-direction, which is the direction of the polarization of the laser field. Trajectories are selected such that they travel less than 150 a.u. from the core. In other words, there must be a significant interaction with the core. We see a clear cutoff and plateau, with odd harmonic peaks. There is even splitting in the lower order harmonic peaks, which occurs due to interferecne between many contributing trajectories. This is not seen at higher orders. The limitation of this approach is that as the number of trajectories is increased the interference between trajectories increases very quickly, as this is a one-dimensional calculation. We find that this effect results in increasing the cutoff harmonic order. The effects of interference between trajectories on the harmonic spectrum are still not well understood.

Previous work using the Herman-Kluk semi-classical approach finds that the plateau arises due to interference between particular types of trajectory, indicating that increasing cutoff harmonic order with increasing numbers of trajectories is due to this effect. We examine this finding with the CCS method by removing the off-diagonal terms in the dipole matrix element Eq. (9.26) and comparing to the full martrix element. Considering only the diagonal terms removes quantum interference between trajectories. Figure 9.3 shows a comparison between the full dipole matrix element and the diagonal matrix element. We see that when including the interference, or in other words using the full

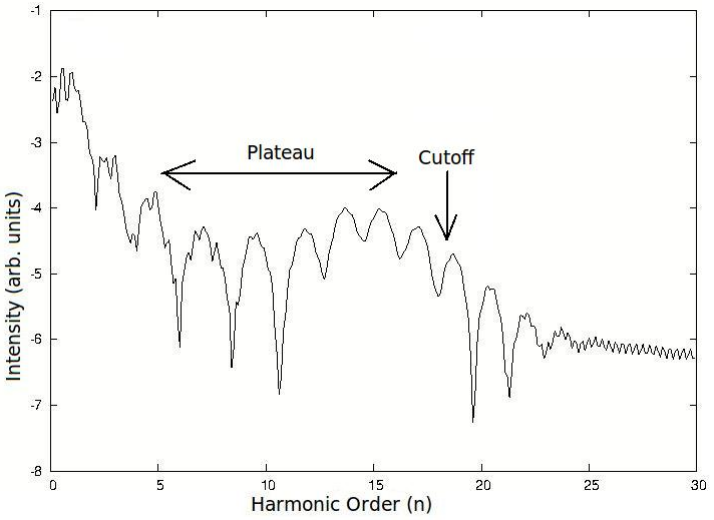

FIGURE 9.2: Harmonic spectra from a sample of CCS trajectories distributed at the quiver distance using the acceleration form of the dipole operator with an electric field with a maximum strength of $E_0 = 0.5$ a.u. and frequency $\omega = 0.05$ a.u.. We consider a trapezium shaped pulse with one cycle ramp up, one cycle ramp down and three cycles of constant intensity.

dipole matrix element, there is a clear plateau and cutoff in the spectrum, as presented in Fig. 9.3 b). The interference in the dipole acceleration is also clear in Fig. 9.3 a), compared to the dipole acceleration without off diagonal terms, Fig. 9.3 c). The presence of off diadonal terms leads to highly oscillatory contributions, which in turn leads to the plateau in the spectrum in Fig. 9.3 b). The corresponding spectrum for which the off diagonal terms have been neglected, Fig. 9.3 d), one sees a very sharp decrease in the harmonic spectrum, with no plateau or cutoff.

In Fig. 9.4 we use the same approach to sampling, with 50 trajectories, and examine the harmonic spectrum using different forms of the dipole operator. Focussing initially on the dipole moment for the length, acceleration and velocity forms a), c) and e), respectively, it can be seen that in the length form, the starting value of the dipole moment is around 60 a.u., which corresponds approximately to the quiver distance. This is not the case in the velocity and acceleration forms, where the initial value is zero a.u. This immediately indicats that the length form includes contributions from static dipoles, unlike the velcotiy and acceleration forms. For the laser field strength and frequency used in the figure, the cutoff harmonic, corresponding to Eq. (9.33), is around a harmonic order of n=105. For the spectrum in Fig. 9.4 b), we indeed observe a spectrum without a cutoff, although after n=105 the spectrum becomes more periodic, compared to the more irregular spectrum before n=105. There is no clear cutoff when employing the velocity form, although one sees no oscillation in the signal approximately

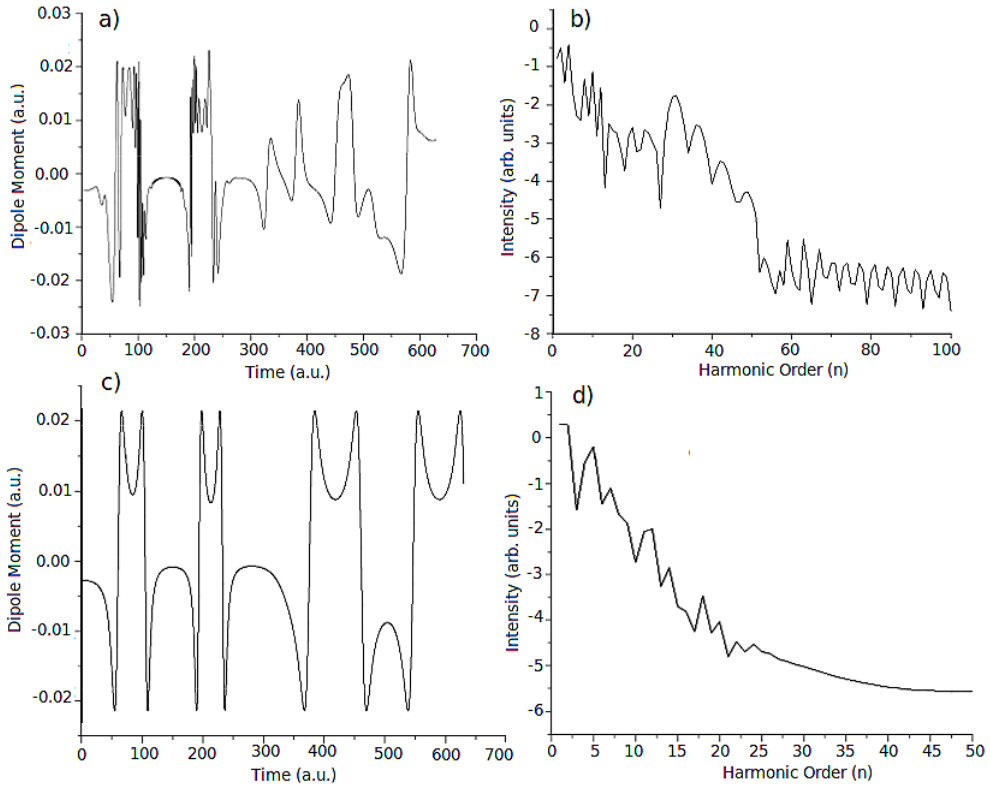

FIGURE 9.3: Comparison of the acceleration form of the dipole operator including the off diagonal terms and neglecting them, a) and b), respectively, and the harmonic spectra calculated using the dipole acceleration with and without off diagonal terms, c) and d), respectively. We consider a laser pulse with the same parameters as the previous figure.

after the cutoff harmonic. The cutoff is clearest and most pronounced in the acceleration form, suggesting that this is the most appropriate form of the dipole operator to use.

9.4 Conclusions and outlook

This chapter presents the first ever computation of HHG spectra using the CCS method. We find that the method is able to reproduce the main features of the harmonic spectrum, such as the plateau and the cutoff. We find that these features are dependent on quantum interference of electron trajectories. Our results agree with the results in the literature obtained for reduced-dimensionality models employing other semi-classical propagators in phase space, which characterize the plateau as a quantum-interference effect [89, 90].

There are two main issues with regard to Monte-Carlo sampling of the initial wavepacket. Firstly, we find that placing the initial wave packet at the core gives rise to highly oscillatory bound trajectories, that lead to spurious high-order harmonics. Secondly, the lack of an absorbing binding potential results in a large drift in the expectation

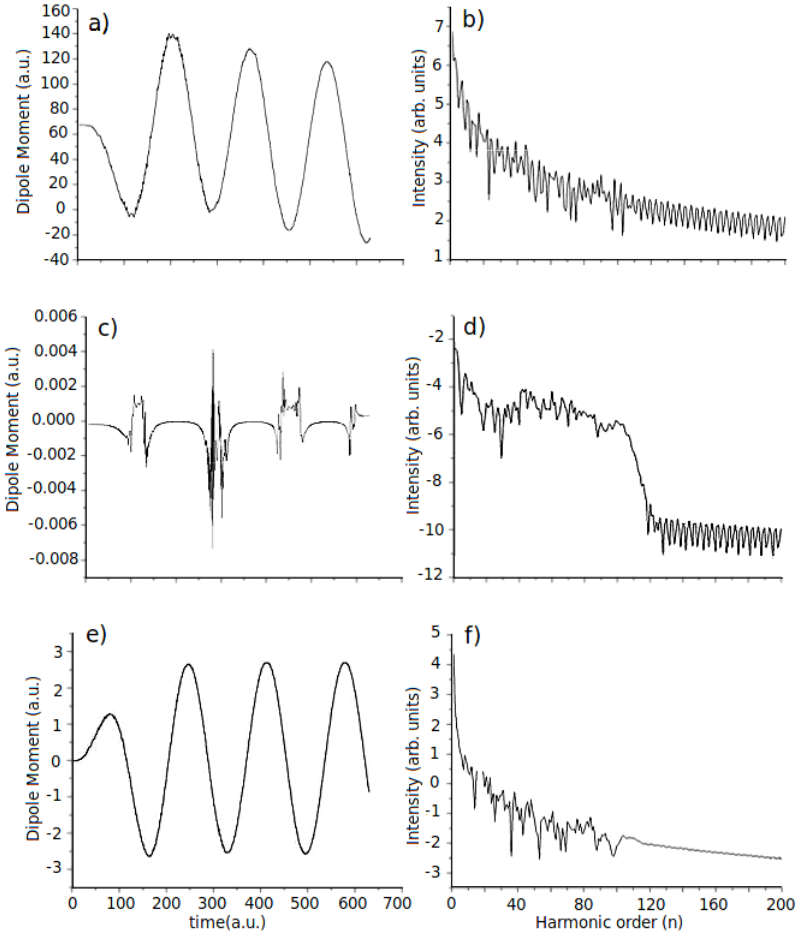

FIGURE 9.4: The dipole moment and corresponding harmonic spectrum in the length form, a) and b), respectively, the acceleration form, c) and d) respectively, and the velocity form, e) and f) respectively. The laser field has a strength of $E_0 = 0.1$ a.u. and $\omega = 0.0378$ a.u., and a pulse shape the same as that in previous figures.

value of the dipole moment in the length form, which is related to irreversible ionization. Both issues can be eliminated by discarding such trajectories or by placing the initial electronic wavepacket at the quiver amplitude. In addition, the drift can be overcome by using a more appropriate form of the dipole operator, the acceleration form.

We note that because HHG is a coherent process, in which quantum interference is extremely important, it is very difficult to achieve converged results with regard to the initial sampling. At present, we are seeking more robust sampling methods in order to overcome this problem.

Chapter 10

Summary

This thesis addresses quantum interference in the context of high harmonic generation (HHG) from atomic and diatomic molecular systems in strong laser fields. These processes are modelled both with the strong field approximation (SFA) and the recently developed coupled coherent state (CCS) approach.

By using the strong field approximation we analyse the influence of multiple orbitals on the high harmonic spectra in Chapters 5, 6 and 7 and find geometric orbital features are mapped onto the harmonic spectrum as well as two-center interference from diatomic molecules. Specifically, in Chapter 5 we analyse the influence of the HOMO-1 by using a multi-electron ground state wavefunction. By making specific assumptions upon the time evolution operator we find that the electron can only ionize and recombine to the same orbital. This is attributed to the static nature of the molecular core, which in our calculations does not evolve during the electron propagation in the continuum. In this approach, the effect of lower lying orbitals is seen in the two-center interference minimum, which becomes more blurred compared when such orbitals are not included. In Chapter 6 we use a multi-electron Lewenstein ansatz which leads to corrections to the standard SFA. We assess the relative importance of these corrections on the form of the dipole operator. We find that, irrespective of the form, the corrections have almost no influence on the overall harmonic spectra. However, we see that in modelling multi-electron effects the velocity form may not be the best choice as it does not allow the inclusion of a static dipole moment for heteronuclear molecules.

In Chapter 7, a slightly different approach is taken. Here, the ground state wavefunction is modelled as a coherent superposition of molecular orbitals. Specifically, the HOMO and the lowest unoccupied molecular orbital (LUMO). Using this formalism on N_2^+ we find the spectrum exhibits specific contributions from different interfering processes, where an electron may ionize from one orbital and recombine with another. Based on

this interpretation, features from different orbitals are mapped onto different regions of the harmonic spectrum.

We extend our analysis to systems with specific geometric orbital features in Chapter 8. By comparing isoelectronic homonuclear and heteronuclear diatomic molecules we relate shifts in the minima in the harmonic spectrum, which occur due to nodal features, to the orbital geometry. In addition, we find that the importance of exchange harmonics is paramount when modelling these features. Comparing modified and unmodified SFA calculations we see that the influence of exchange harmonics is to reduce the definition of minima resulting from harmonic structures in the harmonic spectrum.

We go beyond SFA calculations in Chapter 9 and apply the CCS approach to HHG from atomic Hydrogen. We report developments made in sampling criterium, the importance of the correct choice of form of the dipole operator and asses the influence of interference between trajectories on the harmonic spectrum. We find the most accurate results are obtained by starting the electron wavepacket from the quiver distance and using the acceleration form of the dipole operator. As well as this, we see that the plateau in the harmonic spectrum arises from interference between contributing trajectories and that the trajectories are treated completely classically the plateau is no longer present in the spectrum.

Appendix A

List of abbreviations

AO - Atomic Orbital
ATI - Above Threshold Ionization
CCS - Coupled Coherent States
GTO - Gaussian Type Orbital
HHG - High Harmonic Generation
HK - Herman-Kluk
HF - Hartree-Fock
HOMO - Highest Occupied Molecular Orbital
LCAO - Linear Combination of Atomic Orbitals
MCTDH - Multi-Configurational Time Dependent Hartree
MPI - Multi-Photon Ionization
NSDI - Non Sequential Double Ionization
RESI - Recollision Excitation followed by Subsequent Ionization
SAE - Single Active Electron
SFA - Strong-Field Approximation
SPA - Saddle-Point Approximation
STO - Slater Type Orbital
TDDFT - Time-Dependent Density Functional Theory
TSM - Three Step Model
UA - Uniform Approximation
XUV - Extreme Ultra Violet

Appendix B

Atomic units

In this appendix, we provide the relation between atomic units (a.u.) and the internation system of units (SI). Atomic units are widely used throughout this thesis and the strong laser field community. Defining,

- Mass(Electron mass): m_e=1 a.u.=$9.110\times10^{-31}kg$
- Charge(Electron charge): e=1 a.u.=$1.602\times10^{-19}C$
- Action : $\hbar$=1 a.u.=$1.055\times10^{-34}J\cdot s$
- Length(Bohr radius): r_0=1 a.u.=$0.529\times10^{-10}m$

In the Bohr model of the atom $r_0 = \hbar^2 4\pi\epsilon_0/me^2$ implying that $4\pi\epsilon_0 = 1$. Therefore,

- Electric Field: E_0=$e/4\pi\epsilon_0 a_0^2$=1 a.u.=5.142×10^{11}
- Energy(Hartree energy): E_h=eE_0a_0=1 a.u.=$27.2eV$
- Frequency: ω_0=$E_h/\hbar$=1 a.u.=$4.134\times10^{-16}s^{-1}$
- Time: t_0=$\hbar/E_h$=1 a.u.=$0.0243fs$
- Intensity: 1a.u.=$\epsilon_0 ce^2/2r_0^2$=$3.51\times10^{16}Wcm^{-2}$

Appendix C

Gauge transformations

This appendix provides details on diffeferent gauge formulations used when modelling atoms and molecules in strong laser fields. The material presented here is based on [145]. As well as the length and velocity gauge Hamiltonians in Eq. (3.9) and Eq. (3.7) the time-dependent Schrödinger equation may also be expressed in the so called Kramers-Henneberger [146] frame where it reads

$$i\frac{\partial}{\partial t} \mid \Psi^{KH}(t)\rangle = H^{KH}(t) \mid \Psi(t)\rangle, \tag{C.1}$$

where

$$H^{KH} = \frac{p^2}{2} + V(\mathbf{r} - \int_0^t d\tau \mathbf{A}(\tau)). \tag{C.2}$$

Defining an unitary operator $O_{j\leftarrow i}(t)$ we can move from the gauge equivalent Hamiltonian $H^j(t)$ to $H^i(t)$ using the relation,

$$H^i(t) = i\partial_t O_{j\leftarrow i}(t) O_{j\leftarrow i}(t)^{-1} + O_{j\leftarrow i}(t)^{-1} H^j(t) O_{j\leftarrow i}(t). \tag{C.3}$$

To move between the length, velocity and Krammers-Henneberger gauges we use the relations,

$$O_{V\leftarrow L}(t) = \exp(i\mathbf{r}\cdot\mathbf{A}(t')) \tag{C.4}$$

$$O_{V\leftarrow KH}(t) = \exp(i\int_{t'}^{t} \frac{\mathbf{A}^2(\tau)}{2} d\tau) \exp(-i\int_{t'}^{t} \mathbf{A}(\tau) d\tau \cdot \mathbf{k}) \tag{C.5}$$

$$O_{L\leftarrow KH}(t) = \exp(i\int_{t'}^{t} \frac{\mathbf{A}^2(\tau)}{2} d\tau) \exp(i\mathbf{r}\cdot\mathbf{A}(t')) \exp(-i\int_{t'}^{t} \mathbf{A}(\tau) d\tau \cdot \mathbf{k}), \tag{C.6}$$

Appendix D

Azimuthal angular integration

In this Appendix, expressions for the dipole matrix elements, including the multi-electron corrections, as discussed in Sec. 6.1, are presented in three dimensions. Because the azimuthal angle cannot be resolved we must integrate over it. If one considers a homonuclear molecule, such as N_2, this will result in the HOMO, which in this case is a $3\sigma_g$ molecular orbital, being coupled with $1\pi_{u\chi}$, $1\pi_{u\chi}$, where $\chi = x, y$, $2\sigma_u$ and $1\sigma_u$ orbitals only, due to the symmetry of the wavefunctions. Therefore, the dipole matrix element, including the multi-electron corrections up to the first order, in Eq. (6.2), may be written as,

$$a_\eta(\mathbf{k}+\mathbf{A}(\tau)) = a^{(0)}(\mathbf{k}+\mathbf{A}(\tau)) + d^{(1)}_{\sigma\sigma} + d^{(1)}_{\sigma\pi_x} + d^{(1)}_{\sigma\pi_y}, \tag{D.1}$$

where,

$$d^{(1)}_{\sigma\sigma} = -\sum_{n=1}^{2} d_{3\sigma_g, n\sigma_u}\psi_{n\sigma_u}(\mathbf{k}+\mathbf{A}(\tau)) \tag{D.2}$$

and

$$d^{(1)}_{\sigma\pi_{u\chi}} = -\sum_{n=1}^{2} d_{3\sigma_g, 1\pi_{u\chi}}\psi_{1\pi_{u\chi}}(\mathbf{k}+\mathbf{A}(\tau)), \tag{D.3}$$

are the coupling between the HOMO and the lower lying orbitals of ungerard parity, and $\tau = t', t$, depending on whether the ionization or recombination prefactor is being corrected. Rewriting Eq. (D.1) as,

$$a_\eta(\mathbf{k}+\mathbf{A}(\tau)) = D_\sigma(k,\tau,\theta_k) + D_{\pi_{ux}}(k,\tau,\theta_k)\cos(\phi_k) + D_{\pi_{ux}}(k,\tau,\theta_k)\sin(\phi_k), \tag{D.4}$$

where the dependence of the azimuthal angle has been seperated from the $D(k,\tau,\theta_k)$, then defining

$$\tilde{D}(k,t,t',\theta_k) = \int_0^{2\pi} [a_{rec}(\mathbf{k}+\mathbf{A}(t))]^* a_{ion}(\mathbf{k}+\mathbf{A}(t'))d\phi_k, \tag{D.5}$$

and performing the integration over the azimuthal coordinate, leads to the prefactor,

$$\begin{aligned}\tilde{D}(k,t,t',\theta_k) &= 2\pi\Delta_1(k,t,t',\theta_k) + \pi\Delta_2(k,t,t',\theta_k) \\ &+ \frac{3\pi}{4}\Delta_3(k,t,t',\theta_k) + \frac{\pi}{4}\Delta_4(k,t,t',\theta_k).\end{aligned} \tag{D.6}$$

The constants before the functions $\Delta_N(k,t,t',\theta_k)$ arise from integrals of the form $\int \sin^m(\phi_k)\cos^n(\phi_k)d\phi_k$, where m and n are even integer numbers, and the functions $\Delta_N(k,t,t',\theta_k)$ are defined by,

$$\Delta_1(k,t,t',\theta_k) = |D_{\sigma\sigma}(k,t,t',\theta_k)|^2, \tag{D.7}$$

$$\begin{aligned}\Delta_2(k,t,t',\theta_k) &= |D_{\sigma\pi_x}(k,t,t',\theta_k)|^2 + |D_{\sigma\pi_y}(k,t,t',\theta_k)|^2 \\ &+D_{\sigma\sigma}(k,t,t',\theta_k)(D^*_{\pi_x\pi_x}(k,t,t',\theta_k) + D^*_{\pi_y\pi_y}(k,t,t',\theta_k)) \\ &+D^*_{\sigma\sigma}(k,t,t',\theta_k)(D_{\pi_x\pi_x}(k,t,t',\theta_k) + D_{\pi_y\pi_y}(k,t,t',\theta_k)),\end{aligned} \tag{D.8}$$

$$\Delta_3 = |D_{\pi_x\pi_x}(k,t,t',\theta_k)|^2 + |D_{\pi_y\pi_y}(k,t,t',\theta_k)|^2, \tag{D.9}$$

and

$$\begin{aligned}\Delta_4 &= |D_{\pi_x\pi_y}(k,t,t',\theta_k)|^2 \\ &+D^*_{\pi_x\pi_x}(k,t,t',\theta_k)D_{\pi_y\pi_y}(k,t,t',\theta_k) \\ &+D_{\pi_x\pi_x}(k,t,t',\theta_k)D^*_{\pi_y\pi_y}(k,t,t',\theta_k).\end{aligned} \tag{D.10}$$

where,

$$D_{i,i}(k,t,t',\theta_k) = D^*_i(k,t,\theta_k)D_i(k,t',\theta_k) \tag{D.11}$$

and

$$D_{i,j}(k,t,t',\theta_k) = D^*_i(k,t,\theta_k)D_j(k,t',\theta_k) + D^*_j(k,t,\theta_k)D_i(k,t',\theta_k) \tag{D.12}$$

for $i \neq j$.

Considering now a heteronuclear molecule, and taking CO as an example, all of the orbitals are coupled to the HOMO, due to the asymmetry of the molecular orbital. This leads to additional terms in Eq. (D.2), which will read as,

$$d^{(1)}_{\sigma\sigma} = -\sum_{n=1}^{4} d_{5\sigma,n\sigma_u}\psi_{n\sigma}(\mathbf{k} + \mathbf{A}(\tau)) + d_{static} \tag{D.13}$$

where,

$$d_{static} = \sum_{n=1}^{4} d_{\sigma,n\sigma_u} \psi_{5\sigma}(\mathbf{k} + \mathbf{A}(\tau)). \tag{D.14}$$

We note that due to the asymmetry, the HOMO is now referred to as a 5σ orbital because lower lying orbitals do not have gerade or ungerade symmetry. However, the remaining terms from the integration over the azimuthal angle will remain the same.

Appendix E

Overalp integrals for multi-electron corrections

In this appendix, we provide explicit expressions for the overlap integrals, which are solutions to Eq. (6.14). These expressions have been derived for the direct integrals in the main body of the text.

E.0.1 Length form

Calculating the overlap integrals in the length form, for σ to σ orbital transitions, one obtains,

$$\Upsilon^{\alpha,\beta}_{\varepsilon,\varepsilon}(\sigma,\sigma) = \sum_{j,j'} \frac{\pi b^{(\varepsilon)}_{j,\nu} b^{(\varepsilon)}_{j',\mu}}{\zeta^{(\varepsilon)}_{j,\nu} + \zeta^{(\varepsilon')}_{j',\mu}} \exp\left(-\frac{\zeta^{(\varepsilon)}_{j,\nu}\zeta^{(\varepsilon')}_{j',\mu}}{\zeta^{(\varepsilon)}_{j,\nu} + \zeta^{(\varepsilon')}_{j',\mu}} R^2\right) K(l_\alpha, l_\beta) \tag{E.1}$$

where R is the internuclear distance and where,

$$\begin{aligned} K(l_\alpha, l_\beta) \;=\; & \int_{-\infty}^{\infty} \left[u \pm \frac{\rho^{(\varepsilon)}_{j',j,\mu,\nu}}{2} R\right]^{l_\beta} \left[u \mp \frac{\rho^{(\varepsilon')}_{j,j',\nu,\mu}}{2} R\right]^{l_\alpha} \\ & \times \left[u \mp \frac{\zeta^{(\varepsilon)}_{j,\nu} - \zeta^{(\varepsilon')}_{j',\mu}}{2\zeta^{(\varepsilon)}_{j,\nu} + \zeta^{(\varepsilon')}_{j',\mu}} R\right] \exp[-(\zeta^{(\varepsilon)}_{j,\nu} + \zeta^{(\varepsilon')}_{j',\mu})u^2] du, \end{aligned} \tag{E.2}$$

with

$$\rho^{(\varepsilon)}_{j,j'\nu,\mu} = \frac{-2\zeta^{(\varepsilon)}_{j',\mu}}{\zeta^{(\varepsilon)}_{j,\nu} + \zeta^{(\varepsilon)}_{j',\mu}}, \tag{E.3}$$

and,

$$u = z \pm \frac{\zeta^{(\varepsilon)}_{j,\nu} - \zeta^{(\varepsilon')}_{j',\mu}}{2(\zeta^{(\varepsilon)}_{j,\nu} + \zeta^{(\varepsilon')}_{j',\mu})} R. \tag{E.4}$$

For σ to π_χ transitions, where $\chi = x, y$, the overalp integrals read,

$$\begin{aligned}\Upsilon^{\alpha,\beta}_{\varepsilon,\varepsilon}(\sigma,\sigma) &= \sum_{j,j'} \frac{\pi^{1/2} b^{(\varepsilon)}_{j,\nu} b^{(\varepsilon)}_{j',\mu}}{(\zeta^{(\varepsilon)}_{j,\nu} + \zeta^{(\varepsilon')}_{j',\mu})^{1/2}} \exp\left(-\frac{\zeta^{(\varepsilon)}_{j,\nu}\zeta^{(\varepsilon')}_{j',\mu}}{\zeta^{(\varepsilon)}_{j,\nu} + \zeta^{(\varepsilon')}_{j',\mu}} R^2\right) \\ &\quad \times [F(l_\alpha + 1) J(0, l_\beta) + F(l_\alpha) K(0, l_\beta)],\end{aligned} \tag{E.5}$$

where $F(l)$ has been defined in Eq. (6.18) and ,

$$\begin{aligned}J(l_\alpha, l_\beta) &= \int_{-\infty}^{\infty} \left[u \pm \frac{\rho^{(\varepsilon)}_{j',j,\mu,\nu}}{2} r\right]^{l_\beta} \left[u \mp \frac{\rho^{(\varepsilon')}_{j,j',\nu,\mu}}{2} r\right]^{l_\alpha} \\ &\quad \times \exp[-(\zeta^{(\varepsilon)}_{j,\nu} + \zeta^{(\varepsilon')}_{j',\mu}) u^2] du.\end{aligned} \tag{E.6}$$

Considering π_χ to π_χ transitions, one obtains,

$$\begin{aligned}\Upsilon^{\alpha,\beta}_{\varepsilon,\varepsilon}(\sigma,\sigma) &= \sum_{j,j'} \frac{\pi^{1/2} b^{(\varepsilon)}_{j,\nu} b^{(\varepsilon)}_{j',\mu}}{(\zeta^{(\varepsilon)}_{j,\nu} + \zeta^{(\varepsilon')}_{j',\mu})^{1/2}} \exp\left(-\frac{\zeta^{(\varepsilon)}_{j,\nu}\zeta^{(\varepsilon')}_{j',\mu}}{\zeta^{(\varepsilon)}_{j,\nu} + \zeta^{(\varepsilon')}_{j',\mu}} R^2\right) \\ &\quad \times [F(l_\alpha + l_\beta + 1) J(0,0) + F(l_\alpha + l_\beta) K(0,0)],\end{aligned} \tag{E.7}$$

and finally, for π_χ to π_λ transitions, where $\pi \neq \lambda$,

$$\begin{aligned}\Upsilon^{\alpha,\beta}_{\varepsilon,\varepsilon}(\sigma,\sigma) &= \sum_{j,j'} \frac{\pi^{1/2} b^{(\varepsilon)}_{j,\nu} b^{(\varepsilon)}_{j',\mu}}{(\zeta^{(\varepsilon)}_{j,\nu} + \zeta^{(\varepsilon')}_{j',\mu})^{1/2}} \exp\left(-\frac{\zeta^{(\varepsilon)}_{j,\nu}\zeta^{(\varepsilon')}_{j',\mu}}{\zeta^{(\varepsilon)}_{j,\nu} + \zeta^{(\varepsilon')}_{j',\mu}} R^2\right) \\ &\quad \times [E(l_\alpha, l_\beta) J(0,0) + A(l_\alpha, l_\beta) K(0,0)],\end{aligned} \tag{E.8}$$

where $A(l_\alpha, l_\beta)$ has been defined in Eq. (6.20) and $E(l_\alpha, l_\beta) = A(l_\alpha, l_\beta + 1) + A(l_\alpha, l_\beta + 1)$.

E.0.2 Velocity form

In the velocity form, Eq. (6.14), the overlap integrals for σ to σ transitions, read,

$$\begin{aligned}\Upsilon^{\alpha,\beta}_{\varepsilon,\varepsilon}(\sigma,\sigma) &= \sum_{j,j'} \frac{\pi b^{(\varepsilon)}_{j,\nu} b^{(\varepsilon)}_{j',\mu}}{\zeta^{(\varepsilon)}_{j,\nu} + \zeta^{(\varepsilon')}_{j',\mu}} \exp\left(-\frac{\zeta^{(\varepsilon)}_{j,\nu}\zeta^{(\varepsilon')}_{j',\mu}}{\zeta^{(\varepsilon)}_{j,\nu} + \zeta^{(\varepsilon')}_{j',\mu}} R^2\right) \\ &\quad \times [l_\beta J(l_\alpha, l_\beta - 1) - 2\zeta^{(\varepsilon')}_{j',\mu} J(l_\alpha, l_\beta + 1)].\end{aligned} \tag{E.9}$$

The σ to π_χ, where $\chi = x, y$, overlap integrals read,

$$\begin{aligned}\Upsilon^{\alpha,\beta}_{\varepsilon,\varepsilon}(\sigma,\sigma) &= \sum_{j,j'} \frac{\pi^{1/2} b^{(\varepsilon)}_{j,\nu} b^{(\varepsilon)}_{j',\mu}}{(\zeta^{(\varepsilon)}_{j,\nu} + \zeta^{(\varepsilon')}_{j',\mu})^{1/2}} \exp\left(-\frac{\zeta^{(\varepsilon)}_{j,\nu}\zeta^{(\varepsilon')}_{j',\mu}}{\zeta^{(\varepsilon)}_{j,\nu} + \zeta^{(\varepsilon')}_{j',\mu}} R^2\right) \\ &\quad \times [l_\beta C(l_\beta - 1, l_\alpha, 0) - 2\zeta^{(\varepsilon')}_{j',\mu}(C(l_\beta, l_\alpha, 1) + C(l_\beta - 1, l_\alpha, 0)],\end{aligned} \tag{E.10}$$

where $C(l_\alpha, l_\beta, l_\gamma) = F(l_\alpha)J(l_\beta, l_\gamma)$, and $F(l)$ and $J(l_\alpha, l_\beta)$ are defined in Eq. (6.18) and Eq. (E.7) respectively. For π_χ to π_χ transitions one obtains,

$$\begin{aligned}\Upsilon^{\alpha,\beta}_{\varepsilon,\varepsilon}(\sigma,\sigma) &= \sum_{j,j'} \frac{\pi^{1/2} b^{(\varepsilon)}_{j,\nu} b^{(\varepsilon)}_{j',\mu}}{(\zeta^{(\varepsilon)}_{j,\nu} + \zeta^{(\varepsilon')}_{j',\mu})^{1/2}} \exp\left(-\frac{\zeta^{(\varepsilon)}_{j,\nu}\zeta^{(\varepsilon')}_{j',\mu}}{\zeta^{(\varepsilon)}_{j,\nu} + \zeta^{(\varepsilon')}_{j',\mu}} R^2\right) \\ &\quad \times [l_\beta C(l_\beta + l_\alpha - 1, 0, 0) \\ &\quad -2\zeta^{(\varepsilon')}_{j',\mu}(C(l_\beta + l_\alpha, 0, 1) + C(l_\beta + l_\alpha + 1, 0, 0)],\end{aligned} \tag{E.11}$$

and for π_χ to π_λ transitions, where $\chi \neq \lambda$, the overlap integrals read as,

$$\begin{aligned}\Upsilon^{\alpha,\beta}_{\varepsilon,\varepsilon}(\sigma,\sigma) &= \sum_{j,j'} \frac{\pi^{1/2} b^{(\varepsilon)}_{j,\nu} b^{(\varepsilon)}_{j',\mu}}{(\zeta^{(\varepsilon)}_{j,\nu} + \zeta^{(\varepsilon')}_{j',\mu})^{1/2}} \exp\left(-\frac{\zeta^{(\varepsilon)}_{j,\nu}\zeta^{(\varepsilon')}_{j',\mu}}{\zeta^{(\varepsilon)}_{j,\nu} + \zeta^{(\varepsilon')}_{j',\mu}} R^2\right) \\ &\quad \times [-2\zeta^{(\varepsilon')}_{j',\mu} G(l_\alpha, l_\beta) + l_\beta H(l_\alpha, l_\beta - 1, 0, 0)],\end{aligned} \tag{E.12}$$

where,

$$G(l_\alpha, l_\beta) = H(l_\alpha, l_\beta, 0, 1) + H(l_\alpha + 1, l_\beta, 0, 0) + H(l_\alpha, l_\beta + 1, 0, 0) \tag{E.13}$$

and $H(l_\alpha, l_\beta, l_\gamma, l_\delta) = A(l_\alpha, l_\beta)J(l_\gamma, l_\delta)$, with $A(l_\alpha, l_\beta)$ defined in Eq. (6.20).

E.0.3 Specific integrals for J and K

For the 6-31G basis set employed in the multi-electron perturbative corrections, which include s and p-type atomic orbitals, the particular values for J read,

$$J(0,0) = \left(\frac{\pi}{\zeta^{(\varepsilon)}_{j,\nu} + \zeta^{(\varepsilon')}_{j,\mu}}\right)^{1/2}, \tag{E.14}$$

$$J(0,1) = \pm\frac{\pi^{1/2}\zeta^{(\varepsilon)}_{j,\nu} R}{(\zeta^{(\varepsilon)}_{j,\nu} + \zeta^{(\varepsilon')}_{j,\mu})^{3/2}}, \tag{E.15}$$

$$J(1,1) = \frac{\pi^{1/2}}{2(\zeta_{j,\nu}^{(\varepsilon)} + \zeta_{j,\mu}^{(\varepsilon')})^{3/2}} \left[1 - \frac{2\zeta_{j,\nu}^{(\varepsilon)}\zeta_{j',\mu}^{(\varepsilon')}}{\zeta_{j,\nu}^{(\varepsilon)} + \zeta_{j',\mu}^{(\varepsilon')}} R^2 \right], \tag{E.16}$$

and

$$J(0,2) = \frac{\pi^{1/2}}{2(\zeta_{j,\nu}^{(\varepsilon)} + \zeta_{j,\mu}^{(\varepsilon')})^{3/2}} \left[1 + \frac{2(\zeta_{j,\nu}^{(\varepsilon)})^2}{\zeta_{j,\nu}^{(\varepsilon)} + \zeta_{j',\mu}^{(\varepsilon')}} R^2 \right], \tag{E.17}$$

$$J(1,2) = \pm \frac{\pi^{1/2}}{2(\zeta_{j,\nu}^{(\varepsilon)} + \zeta_{j,\mu}^{(\varepsilon')})^{5/2}} \left[(\zeta_{j',\mu}^{(\varepsilon')} - 2\zeta_{j,\nu}^{(\varepsilon)})R + \frac{2\zeta_{j',\mu}^{(\varepsilon')}(\zeta_{j,\nu}^{(\varepsilon)})^2}{\zeta_{j,\nu}^{(\varepsilon)} + \zeta_{j',\mu}^{(\varepsilon')}} R^3 \right], \tag{E.18}$$

For the K integrals, in Eq. (E.3), one obtains,

$$K(0,0) = \mp \left(\frac{\pi}{\zeta_{j,\nu}^{(\varepsilon)} + \zeta_{j,\mu}^{(\varepsilon')}} \right)^{1/2} \frac{\zeta_{j,\nu}^{(\varepsilon)} - \zeta_{j,\mu}^{(\varepsilon')}}{2(\zeta_{j,\nu}^{(\varepsilon)} + \zeta_{j,\mu}^{(\varepsilon')})} R \tag{E.19}$$

$$K(0,1) = \frac{\pi^{1/2}}{2(\zeta_{j,\nu}^{(\varepsilon)} + \zeta_{j,\mu}^{(\varepsilon')})^{3/2}} \left[1 + \frac{\zeta_{j,\nu}^{(\varepsilon)}(\zeta_{j,\nu}^{(\varepsilon)} - \zeta_{j,\mu}^{(\varepsilon')})}{2(\zeta_{j,\nu}^{(\varepsilon)} + \zeta_{j,\mu}^{(\varepsilon')})} R^2 \right], \tag{E.20}$$

$$K(1,0) = \frac{\pi^{1/2}}{2(\zeta_{j,\nu}^{(\varepsilon)} + \zeta_{j,\mu}^{(\varepsilon')})^{3/2}} \left[1 - \frac{\zeta_{j,\nu}^{(\varepsilon)}(\zeta_{j,\nu}^{(\varepsilon)} - \zeta_{j,\mu}^{(\varepsilon')})}{2(\zeta_{j,\nu}^{(\varepsilon)} + \zeta_{j,\mu}^{(\varepsilon')})} R^2 \right], \tag{E.21}$$

and

$$K(1,1) = \mp \frac{\pi^{1/2}(\zeta_{j,\nu}^{(\varepsilon)} - \zeta_{j,\mu}^{(\varepsilon')})}{2(\zeta_{j,\nu}^{(\varepsilon)} + \zeta_{j,\mu}^{(\varepsilon')})^{5/2}} \left[\frac{3R}{2} - \frac{\zeta_{j,\nu}^{(\varepsilon)}\zeta_{j,\mu}^{(\varepsilon')}}{\zeta_{j,\nu}^{(\varepsilon)} + \zeta_{j,\mu}^{(\varepsilon')}} R^3 \right]. \tag{E.22}$$

We note that for transitions between an arbitrary orbital with an arbitrary form of the dipole operator, will result in a term proportional to $\exp(-R^2)$. This exponential dependance will cause the overlap integrals to be insignificant compared to the direct integrals, as can be seen from Fig. 6.5 in Sec. 6.2.

Appendix F

Derivation of the multi-electron dipole matrix element

In this appendix, the most important steps leading to Eq. (6.4) and Eq. (6.7) are presented which was first derived in [64]. The multi-electron extension of Eq. (3.26) may be written as,

$$\mid \Psi\rangle = \mid \Psi_0^N\rangle + \sum_k \frac{b_k(t)}{\sqrt{2}} \left(c_{k+}^\dagger \mid \Psi_{0-}^{N-1}\rangle + c_{k-}^\dagger \mid \Psi_{0+}^{N-1}\rangle \right) \tag{F.1}$$

where $c_{k\sigma}^\dagger$ creates an electron in a plane wave state with momentum $\mathbf{k}$ and spin $\sigma/2$ and $\mid \Psi_0^N\rangle$ is the N electron ground state wavefunction. The recombination matrix element may then be written as,

$$a_{rec}(\mathbf{k}) = \frac{1}{\sqrt{2}} \sum_\sigma a_{rec}^\sigma(\mathbf{k}) \tag{F.2}$$

where,

$$a_{rec}^\sigma(\mathbf{k}) = \langle \Psi_0^N \mid \hat{D} c_{k\sigma}^\dagger \mid \Psi_{\overline{\sigma}}^{N-1}\rangle, \tag{F.3}$$

with

$$\hat{D} = \sum_{k'\sigma'} \sum_{k''\sigma''} \langle \mathbf{k}'\sigma' \mid d \mid \mathbf{k}''\sigma''\rangle c_{k'\sigma'}^\dagger c_{k''\sigma''}, \tag{F.4}$$

where d is the dipole operator and $\overline{\sigma}$ represents the opposite spin to σ. Considering

$$\hat{D} c_{k\sigma}^\dagger = c_{k\sigma}^\dagger \hat{D} + [\hat{D}, c_{k\sigma}^\dagger] \tag{F.5}$$

along with,

$$[c_{k'\sigma'}^\dagger c_{k''\sigma''}, c_{k\sigma}^\dagger] = -[c_{k\sigma}^\dagger, c_{k'\sigma'}^\dagger]_\dagger c_{k''\sigma''} + c_{k'\sigma'}^\dagger [c_{k\sigma}^\dagger, c_{k''\sigma''}]_\dagger, \tag{F.6}$$

where, $[]_\dagger$ indicates the anti-commutator. Noting that

$$[c^\dagger_{k\sigma}, c^\dagger_{k'\sigma'}]_\dagger = 0 \tag{F.7}$$

and

$$[c^\dagger_{k\sigma}, c_{k''\sigma''}]_\dagger = \delta_{k\sigma,k''\sigma''} \tag{F.8}$$

one obtains

$$\begin{aligned} \hat{D}c^\dagger_{k\sigma} &= c^\dagger_{k\sigma}\hat{D} + \sum_{k'\sigma'}\sum_{k''\sigma''} c^\dagger_{k'\sigma'}\delta_{k\sigma,k''\sigma''}\langle \mathbf{k}'\sigma' \mid d \mid \mathbf{k}''\sigma''\rangle & \text{(F.9)} \\ &= c^\dagger_{k\sigma}\hat{D} + \sum_{k'\sigma'} c^\dagger_{k'\sigma'}\langle \mathbf{k}'\sigma' \mid d \mid \mathbf{k}\sigma\rangle. & \text{(F.10)} \end{aligned}$$

Therefore, the recombination dipole matrix element becomes,

$$a^\sigma_{rec}(\mathbf{k}) = \langle \Psi^N_0 \mid c^\dagger_{k\sigma}\hat{D} \mid \Psi^{N-1}_{0\overline{\sigma}}\rangle + \sum_{k'\sigma'}\langle \Psi^N_0 \mid c^\dagger_{k'\sigma'} \mid \Psi^{N-1}_{0\overline{\sigma}}\rangle\langle \mathbf{k}'\sigma' \mid d \mid \mathbf{k}\sigma\rangle \tag{F.11}$$

Defining a Dyson orbital as,

$$\mid \Psi^{(D)}_{0\sigma}\rangle = \sum_{k'\sigma'}\langle \Psi^{N-1}_{0\overline{\sigma}} \mid c^\dagger_{k'\sigma'} \mid \Psi^N_0\rangle \mid \mathbf{k}'\sigma'\rangle \tag{F.12}$$

the recombination dipole matrix element becomes,

$$a^\sigma_{rec} = \langle \Psi^N_0 \mid c^\dagger_{k\sigma}\hat{D} \mid \Psi^{N-1}_{0\overline{\sigma}}\rangle + \langle \Psi^{(D)}_{0\sigma} \mid d \mid \mathbf{k}\sigma\rangle \tag{F.13}$$

Using the canonical Hartree-Fock orbitals we may write,

$$\langle \Psi^{(D)}_0 \mid d \mid \mathbf{k}\rangle = \sum_p \langle \Psi^N_0 \mid c^\dagger_p \mid \Psi^{N-1}_0\rangle\langle \psi_p \mid d \mid \mathbf{k}\rangle, \tag{F.14}$$

and

$$\langle \Psi^N_0 \mid c^\dagger_k\hat{D} \mid \Psi^{N-1}_0\rangle = \sum_p \langle \Psi^N_0 \mid c^\dagger_k\hat{D} \mid \Psi^{N-1}_0\rangle\langle \psi_p \mid \mathbf{k}\rangle, \tag{F.15}$$

where ψ_p is a HF spin orbital and the σ indicie has been dropped for convenience. The exact multi-electron wavefunction may be replaced by the Hartree-Fock (HF) wavefunction. In [64], Möller-Plesset perturbation theory was used up to the second order. Here, we do not include second order corrections and simply write,

$$\mid \Psi^N_0\rangle = \mid \Phi^N_0\rangle, \tag{F.16}$$

and

$$\mid \Psi_0^{N-1}\rangle = c_0 \mid \Phi_0^N\rangle, \tag{F.17}$$

where the HF wavefunction satisfies,

$$\mid \Psi_0^N\rangle = \prod_{i=1}^{N} c_i^\dagger \mid\rangle, \tag{F.18}$$

with $|\rangle$ representing the vacuum. Inserting Eq. (F.16) and Eq. (F.17) into Eq. (F.14) and using Eq. (F.8), one obtains Eq. (6.3),

$$\langle \Psi_0^{(D)} \mid d \mid \mathbf{k}\rangle = \langle \Phi_0 \mid d \mid \mathbf{k}\rangle, \tag{F.19}$$

indicating that we do not distinguish between the Dyson orbital and the HF orbital. Applying the same procedure to Eq. (F.15), one obtains Eq. (6.4),

$$\langle \Psi_0^N \mid c_k^\dagger \hat{D} \mid \Psi_0^{N-1}\rangle = \sum_i \langle i \mid d \mid i\rangle\langle \phi_0 \mid \mathbf{k}\rangle - \langle 0 \mid d \mid i\rangle\langle \phi_0 \mid \mathbf{k}\rangle. \tag{F.20}$$

Appendix G

Derivation of the dipole matrix elements in the CCS basis

In this appendix we perform the derivations to express the dipole matrix elements in the coupled coherent state (CCS) basis in the three forms of the dipole operator, as presented in Chapter 9.

G.1 Length form

In the length form, this derivation is immediate as the dipole matrix element can be expressed as,

$$d^l_{k,m} = \langle \mathbf{z}_k \mid \hat{r} \mid \mathbf{z}_m \rangle = \sqrt{\frac{1}{2\omega}} \langle \mathbf{z}_k \mid (\hat{a}^\dagger + \hat{a}) \mid \mathbf{z}_m \rangle \tag{G.1}$$

giving,

$$d_{k,m} = \sqrt{\frac{1}{2\omega}} (\mathbf{z}^*_k + \mathbf{z}_m) \langle \mathbf{z}_k \mid \mathbf{z}_m \rangle. \tag{G.2}$$

G.2 Velocity form

In the velocity form, we must calculate,

$$\begin{aligned} d^v_{k,m} &= \langle \mathbf{z}_k \mid \hat{p} \mid \mathbf{z}_m \rangle & \text{(G.3)} \\ &= i \int d^3\mathbf{r} \langle \mathbf{z}_k \mid \mathbf{r} \rangle \nabla_r (\langle \mathbf{r} \mid \mathbf{z}_m \rangle). & \text{(G.4)} \end{aligned}$$

Using,

$$\langle \mathbf{r} \mid \mathbf{z} \rangle = \left(\frac{\gamma}{\pi}\right)^{3/4} exp[-\frac{\gamma}{2}(\mathbf{r} - \mathbf{q}')^2 + i\mathbf{p}' \cdot (\mathbf{r} - \mathbf{q}') + i\frac{\mathbf{p}' \cdot \mathbf{q}'}{2}], \tag{G.5}$$

which is the coherent state in the position basis, in three dimensions, and

$$\nabla_r(\langle \mathbf{r} \mid \mathbf{z}' \rangle) = (-\gamma(\mathbf{r} - \mathbf{q}) + i\mathbf{p})\langle \mathbf{r} \mid \mathbf{z}' \rangle, \tag{G.6}$$

as well as the relation

$$\langle \mathbf{z}_k \mid \mathbf{r} \rangle \langle \mathbf{r} \mid \mathbf{z}_m \rangle = \left(\frac{\gamma}{\pi}\right)^{3/2} \langle \mathbf{z}_k \mid \mathbf{z}_m \rangle e^{-\frac{\gamma}{2}(\mathbf{r}-\rho)^2} \tag{G.7}$$

where ρ is defined in Eq. (9.24), one obtains

$$d^v_{k,m} = i\left(\frac{\gamma}{\pi}\right)^{3/2} \langle \mathbf{z}_k \mid \mathbf{z}_m \rangle \int d^3\mathbf{r}[-\gamma(\mathbf{r} - \mathbf{q}') + i\mathbf{p}']e^{-\frac{\gamma}{2}(\mathbf{r}-\rho)^2}. \tag{G.8}$$

Performing the integral gives

$$d^v_{k,m} = i\langle \mathbf{z} \mid \mathbf{z}' \rangle \left(-\gamma(\rho - \mathbf{q}') + i\mathbf{p}'\right). \tag{G.9}$$

G.3 Acceleration form

Finally, we calculate the dipole matrix element in the coherent state basis for the acceleration form,

$$\begin{aligned} d^a_{k,m} &= \langle \mathbf{z}_k \mid \nabla\frac{1}{r} \mid \mathbf{z}_m \rangle & \text{(G.10)} \\ &= \langle \mathbf{z}_k \mid \mathbf{z}_m \rangle \left(\frac{\gamma}{\pi}\right)^{3/2} \int d^3\mathbf{r}(\nabla\frac{1}{r})e^{-\gamma(\mathbf{r}-\rho)^2}, & \text{(G.11)} \end{aligned}$$

where Eq. (G.7) has been used. Expressing the integral in spherical co-ordinates, and restricting r to the z direction such that $\mathbf{z} = r\cos(\theta)\hat{e}_z$ on obtains,

$$d^a_{k,m} = -2\pi\left(\frac{\gamma}{\pi}\right)^{3/2} \int_{-1}^{1} d\cos(\theta) \int_0^\infty dr\cos(\theta)e^{-\gamma(r^2+\rho^2-2r\rho\cos(\theta))}\hat{e}_z, \tag{G.12}$$

The integration over $\cos(\theta)$ is performed using,

$$\int d\cos(\theta)\cos(\theta)e^{-\gamma(r^2+\rho^2-2r\rho\cos(\theta)} = \frac{e^{-\gamma(\rho^2-2\rho r\cos(\theta)+r^2)}(2\gamma\rho r\cos(\theta) - 1)}{4\gamma^2\rho^2r^2}, \tag{G.13}$$

which yields,

$$d^a_{k,m} = -2\pi\left(\frac{\gamma}{\pi}\right)^{3/2} \int_0^\infty dr\frac{e^{-\gamma(r-\rho)^2}(2\gamma\rho r - 1) + e^{-\gamma(r+\rho)^2}(2\gamma\rho r + 1)}{4\gamma^2\rho^2r^2}. \tag{G.14}$$

The integral over r reads

$$\int \frac{e^{-\gamma(r\pm\rho)^2}(2\gamma r\rho \pm 1)}{4\gamma^2\rho^2 r^2} dr = \frac{-\sqrt{\pi\gamma} erf(\sqrt{\gamma}(r \pm \rho)) - \frac{e^{-\gamma(\rho\pm r)^2}}{r}}{4\gamma^2\rho^2}. \tag{G.15}$$

Hence,

$$\begin{aligned} d^a_{k,m} &= -\frac{1}{2\rho^2\sqrt{\pi\gamma}} \left[\sqrt{\pi\gamma}(erf(\sqrt{\gamma}(r-\rho)) - erf(\sqrt{\gamma}(r+\rho)))\right]_0^\infty \hat{e}_z \\ &\quad -\frac{1}{2\rho^2\sqrt{\pi\gamma}} \left[\frac{e^{-\gamma(r-\rho)^2}\hat{e}_z - e^{-\gamma(r+\rho)^2}}{r}\right]_0^\infty \hat{e}_z, \end{aligned} \tag{G.16}$$

$$d^a_{k,m} = -\frac{1}{\rho^2} erf(\rho\sqrt{\gamma})\hat{e}_z \tag{G.17}$$

$$\begin{aligned} &\quad -\frac{1}{2\rho^2\sqrt{\pi\gamma}} lim_{r\to 0} \frac{e^{-\gamma(r+\rho)^2} - e^{-\gamma(r-\rho)^2}}{r} \\ &= -\frac{1}{\rho^2} erf(\rho\sqrt{\gamma})\hat{e}_z + \frac{1}{2\rho^2\sqrt{\pi\gamma}} 4\gamma\rho e^{-\gamma\rho^2}\hat{e}_z, \end{aligned} \tag{G.18}$$

which finally leads to the expression

$$d_{k,m} = -\frac{1}{\rho^2} erf(\rho\sqrt{\gamma})\hat{e}_z + 2\sqrt{\frac{\gamma}{\pi}} \frac{e^{-\gamma\rho^2}}{\rho}\hat{e}_z \tag{G.19}$$

Bibliography

[1] C. Figueira de Morisson Faria and B. B. Augstein, "Molecular high-order harmonic generation with more than one active electron: Quantum-interference effects," *Phys. Rev. A.*, vol. 81, p. 043409, 2010.

[2] B. B. Augstein and C. Figueira de Morisson Faria, "Multi-electron corrections in molecular high harmonic generation for different formulations of the strong-field approximation," *J. Mod. Opt.*, vol. 58, p. 1173, 2011.

[3] B. B. Augstein and C. Figueira de Morisson Faria, "Influence of asymmetry and nodal structures on high-order harmonic generation in heteronuclear molecules," *J. Phys. B*, vol. 44, p. 055601, 2011.

[4] T. Shaaran and B. B. Augstein and C. Figueira de Morisson Faria, "Excitation, two-center interference and the orbital geometry in laser-induced nonsequential double ionization of diatomic molecules," *Phys. Rev. A*, vol. 84, p. 013429, 2011.

[5] B. B. Augstein and C. Figueira de Morisson Faria, "High-order harmonic generation in diatomic molecules: Quantum interference, nodal structures and multiple orbitals," *Mod. Phys. Lett. (accepted)*, vol. xx, p. xxx, 2011.

[6] X. F. Li, A. L'Huillier, M. Ferray, L. A. Lompré, and G. Mainfray, "Multiple-harmonic generation in rare gases at high laser intensity," *Phys. Rev. A.*, vol. 39, p. 5751, 1989.

[7] J. Itatani, J. Levesque, D. Zeidler, H. Niikura, H. Pépin, J. Keiffer, P. Corkum, and D. Villeneuve, "Tomographic imaging of molecular orbitals," *Nature*, vol. 432, p. 867, 2004.

[8] E. Goulielmakis, M. Uiberacker, R. Kienberger, A. Baltuska, V. Yakovlev, A. Scrinzi, T. Westerwalbesloh, U. Kleinberg, U. Heinzmann, M. Drescher, and F. Krausz, "Direct measurement of light waves," *Science*, vol. 305, p. 1267, 2004.

[9] O. Smirnova, Y. Mairesse, S. Patchkovskii, N. Dudovich, D. Villeneuve, P. Corkum, and M. Y. Ivanov, "High harmonic interferometry of multi-electron dynamics in molecules," *Nature*, vol. 460, p. 972, 2009.

[10] M. Kling and M. Vrakking, "Attosecond electron dynamics," *Annu. Rev. Phys. Chem*, vol. 59, p. 463, 2008.

[11] S. Haessler, J. Caillat, and P. Salières, "Self-probing of molecules with high harmonic generation," *J. Phys. B*, vol. 44, p. 203001, 2011.

[12] A. Szabo and N. Ostlund in *Modern quantum chemistry: Introduction to advanced electronic structure theory*, New York: McMillan, 1982.

[13] M. Guest, I. Bush, H. van Dam, P. Sherwood, J. Thomas, J. van Lenthe, R. Havenith, and J. Kendrick, "The GAMESS-UK electronic structure package: algorithms, developments and applications," *Mol. Phys.*, vol. 103, p. 719, 2005.

[14] P. Cade, K. Sales, and A. Wahl, "Electronic Structure of Diatomic Molecules. III. A. HartreeFock Wavefunctions and Energy Quantities for $N_2(\Sigma_g^+)$ and $N_2^+(X^2\Sigma_g^+, A^2\Pi_u, B^2\Sigma_u^+)$ molecular ions," *J. Chem. Phys.*, vol. 44, p. 1963, 1966.

[15] D. V. Shalashilin, "Quantum and classical molecular dynamics group." http://www1.chem.leeds.ac.uk/CCS/.

[16] J. P. Gordon, H. J. Zeiger, and C. H. Townes, "Molecular microwave oscillator and new hyperfine structure in the microwave spectrum of NH_3," *Phys. Rev.*, vol. 95, p. 282, 1954.

[17] A. Einstein, "On the electrodynamics of moving bodies," *Ann. der Phys*, vol. 17, p. 132, 1905.

[18] D. Strickland and G. Mourou, "Compression of amplified chirped optical pulses," *Opt. Commun.*, vol. 56, p. 219, 1985.

[19] M. Hentschel, R. Kienberger, C. Spielmann, G. A. Reider, N. Milosevic, T. Brabec, P. Corkum, U. Heinzmann, M. Drescher, and F. Krausz, "Attosecond metrology," *Nature*, vol. 414, p. 509, 2001.

[20] R. Kienberger, E. Goulielmakis, M. Uiberacker, A. Baltuska, V. Yakovlev, F. Bammer, A. Scrinzi, T. Westerwalbesloh, U. Kleinberg, U. Heinzmann, M. Drescher, and F. Krausz, "Atomic transient recorder," *Nature*, vol. 427, p. 817, 2004.

[21] C. Vozzi, M. Negro, F. Calegari, G. Sansone, M. Nisoli, S. D. Silvestri, and S. Stagira, "Generalized molecular orbital tomography," *Nat. Phys.*, vol. 7, p. 822, 2011.

[22] J. S. Parker, B. J. S. Doherty, K. T. Taylor, K. D. Schultz, C. I. Blaga, and L. F. DiMauro, "High-energy cutoff in the spectrum of strong-field nonsequential double ionization," *Phys. Rev. Lett.*, vol. 96, p. 133001, 2006.

[23] B. McFarland, J. Farrell, P. Bucksbaum, and M. Gühr, "High harmonic generation from multiple orbitals in N_2," *Science*, vol. 322, p. 1232, 2008.

[24] G. Jordan and A. Scrinzi, "Core polarization effects in molecular high harmonic generation," *N. J. Phys.*, vol. 10, p. 025035, 2008.

[25] D. A. Telnov and S. I. Chu, "Effects of multiple electronic shells on strong-field multiphoton ionization and high-order harmonic generation of diatomic molecules with arbitrary orientation: An all-electron time-dependent density-functional approach," *Phys. Rev. A*, vol. 80, p. 043412, 2009.

[26] S. Sukiasyan, C. McDonald, C. Destefani, M. Y. Ivanov, and T. Brabec, "Multielectron correlation in high-harmonic generation: A 2D model analysis," *Phys. Rev. Lett.*, vol. 102, p. 223002, 2009.

[27] S. Odžak and D. B. Milošević, "Interference effects in high-order harmonic generation by homonuclear diatomic molecules," *Phys. Rev. A*, vol. 79, p. 023414, 2009.

[28] A. McPherson, G. Gibson, H. Jara, U. Johann, T. Luk, I. McIntyre, K. Boyer, and C. K. Rhodes, "Studies of multiphoton production of vacuum-ultraviolet radiation in the rare gases," *J. Opt. Soc. Am.*, vol. B4, p. 595, 1987.

[29] M. Ferray, A. L'Huillier, F. Li, L. Lompré, G. Mainfray, and C. Manus, "Multiple-harmonic conversion of 1064nm radiation in rare gases," *J. Phys. B*, vol. 21, p. L31, 1988.

[30] G. Petite, P. Agostini, and H. G. Muller, "Intensity dependence of non-perturbative above-threshold ionisation spectra: experimental study," *J. Phys. B*, vol. 21, p. 4097, 1988.

[31] A. L'Huillier, L. A. Lompré, G. Mainfray, and C. Manus, "Multiply charged ions induced by multiphoton absorption processes in rare-gas atoms at 1.064 μm," *J. Phys. B.*, vol. 16, p. 1363, 1982.

[32] P. B. Corkum, "Plasma perspective on strong field mulitphoton ionization," *Phys. Rev. Lett.*, vol. 71, p. 1994, 1993.

[33] C Figueira de Morisson Faria and T. Shaaran and X. Liu and W. Yang, "Quantum interference in laser-induced nonsequential double ionization in diatomic molecules : Role of alignment and orbital symmetry," *Phys. Rev. A*, vol. 78, p. 043407, 2008.

[34] C. Figueira de Morisson Faria, "Laser-induced nonsequential double ionization in diatomic molecules: One and two-center rescattering scenarios," *J. Phys. B.*, vol. 42, p. 134008, 2009.

[35] T. Shaaran and M. T. Nygren and C. Figueira de Morisson Faria, "Laser-induced nonsequential double ionization at and above recollison-excitation-tunneling threshold," *Phys. Rev. A*, vol. 81, p. 063413, 2010.

[36] T. Shaaran and C. Figueira de Morisson Faria, "Laser-induced nonsequential double ionization: Kinematic constraints for the recollision-excitation-tunneling mechanism," *J. Mod. Opt.*, vol. 57, p. 11, 2010.

[37] S. Haessler, J. Caillat, W. Boutu, C. Giovanetti-Teixeira, T. Ruchon, T. Auguste, Z. Diveki, P. Breger, A. Maquet, B. Carré, R. Taïeb, and P. Salières, "Attosecond imaging of molecular electronic wavepackets," *Nature*, vol. 6, p. 200, 2010.

[38] B. McFarland, J. Farrell, P. Bucksbaum, and M. Gühr, "High-order harmonic phase in molecular nitrogen," *Phs. Rev. A*, vol. 80, p. 033412, 2009.

[39] Y. Huismans, A. Rouzée, A. Gijsbertsen, J. H. Jungmann, A. S. Smolkowska, P. S. W. M. Logman, F. Lépine, C. Cauchy, S. Zamith, T. Marchenko, J. M. Bakker, G. Berden, B. RedLich, A. F. G. van der Meer, H. G. Muller, W. Vermin, K. J. Schafer, M. Spanner, M. Y. Ivanov, O. Smirnova, D. Bauer, S. V. Popruzhenko, and M. J. J. Vrakking, "Time-resolved holography with photoelectrons," *Science*, vol. 331, p. 61, 2011.

[40] A. H. Zewail in *Femtochemistry: Ultrafast dynamics of the chemical bond*, Singapore: World Scientific, 1994.

[41] S. Baker, J. S. Robinson, C. A. H. amd H. Teng, R. A. Smith, C. C. Chirilă, M. Lein, J. W. G. Tisch, and J. P. Marangos, "Probing proton dynamics in molecules on an attosecond time scale," *Science*, vol. 312, p. 424, 2008.

[42] S. Baker, J. S. Robinson, M. Lein, C. C. Chirilă, R. Torres, H. C. Bandulet, D. Comtois, J. C. Kieffer, D. M. Villeneuve, J. W. G. Tisch, and J. P. Marangos, "Dynamic two-center interference in high-order harmonic generation from molecules with attosecond nuclear motion," *Phys. Rev. Lett*, vol. 101, p. 053901, 2008.

[43] J. Seres, E. Seres, A. J. Verhoef, G. Tempea, C. Streli, P. Wobrauschek, V. Yakovlev, A. Scrinzi, C. Spielmann, and F. Krausz, "Source of coherent kiloelectronvolt X-rays," *Nature*, vol. 433, p. 596, 2005.

[44] M. Drescher, M. Hentschel, R. Kienberger, M. Uiberacker, V. Yakovlev, A. Scrinzi, T. Westerwalbesloh, U. Kleineberg, U. Heinzmann, and F. Krausz, "Time-resolved atomic inner-shell spectroscopy," *Nature*, vol. 419, p. 803, 2002.

[45] M. Uiberacker, T. Uphues, M. Schultze, A. J. Verhoef, V. Yakovlev, M. F. Kling, J. Rauschenberger, N. M. Kabachnik, H. Schröder, M. Lezius, K. L. Kompa, H. G. Muller, M. J. J. Vrakking, S. Hendel, U. Kleineberg, U. Heinzmann, M. Drescher, and F. Krausz, "Attosecond real-time observation of electron tunnelling in atoms," *Nature*, vol. 446, p. 627, 2007.

[46] M. Lewenstein, P. Balcou, M. Y. Ivanov, A. LHuillier, and P. B. Corkum, "Theory of high-harmonic generation by low-frequency laser fields," *Phys. Rev. A.*, vol. 49, p. 2117, 1994.

[47] D. B. Milošević, "Strong-field approximation for ionization of a diatomic molecule by a strong laser field," *Phys. Rev. A*, vol. 74, p. 063404, 2006.

[48] C. C. Chirilă and M. Lein, "Assessing different forms of the strong-field approximation for harmonic generation in molecules," *J. Mod. Opt.*, vol. 54, p. 1039, 2007.

[49] C. Figueira de Morisson Faria, "High-harmonic generation in diatomic molecules: A quantum orbit analysis of the interference patterns," *Pys. Rev. A*, vol. 76, p. 043407, 2007.

[50] C. Kan, C. E. Kapjack, R. Rankin, and N. H. Burnett, "Spectral and temporal structure in high harmonic emission from ionizing atomic gases," *Phys. Rev. A*, vol. 52, p. R4336, 1995.

[51] Y. Liang, S. Augst, S. L. Chin, Y. Beaudoin, and M. Chaker, "High harmonic generation in atomic and diatomic molecular gases using intense picosecond laser pulses - a comparison," *J. Phys. B*, vol. 27, p. 5119, 1994.

[52] C. Vozzi, R. Torres, M. Negro, L. Brugnera, T. Siegel, C. Altucci, R. Velotta, F. Frassetto, L. Poletto, P. Villoresi, S. D. Silvestri, S. Stagira, and J. P. Marangos, "High harmonic generation spectroscopy of hydrocarbons," *App. Phys. Lett.*, vol. 97, p. 241103, 2010.

[53] S. Ghimire, A. D. DiChiara, E. Sistrunk, P. Agostini, L. F. DiMauro, and D. A. Reis, "Observation of high-order harmonic generation in a bulk crystal," *Nature Physics*, vol. 7, p. 138, 2011.

[54] J. P. Marangos, "High-harmonic generation : Solid Progress," *Nature Physics*, vol. 7, p. 97, 2011.

[55] R. Velotta, N. Hay, M. Manson, M. Castillejo, and J. P. Marangos, "High-order harmonic generation in aligned molecules," *Phys. Rev. Lett.*, vol. 87, p. 183901, 2001.

[56] H. Stapelfeldt and T. Seidman, "Colloquium: Aligning molecules with strong laser pulses," *Rev. Mod. Phys.*, vol. 75, p. 543, 2003.

[57] N. Hay, R. Velotta, M. Lein, R. de Nalda, E. Heesel, M. Castillejo, and J. P. Marangos, "High-order harmonic generation in laser-aligned molecules," *Phys. Rev. A*, vol. 65, p. 053805, 2002.

[58] D. Pavičić, K. Lee, D. Rayner, P. Corkum, and D. Villeneuve, "Direct measurement of angular dependence of ionization for N_2, O_2 and CO_2 in intense laser fields," *Phys. Rev. Lett.*, vol. 98, p. 243001, 2007.

[59] M. Abu-samha and L. B. Madsen, "Theory of strong-field ionization of aligned CO_2," *Phys. Rev. A*, vol. 80, p. 023401, 2009.

[60] S. Petretti, Y. Vanne, A. Saenz, A. Castro, and P. Decleva, "Alignment-dependent ionization of N_2, O_2 and CO_2 in intense laser fields," *Phys. Rev. Lett.*, vol. 104, p. 223001, 2010.

[61] V. Usachenko and S. Chu, "Strong-field ionization of laser-irradiated light homonuclear diatomic molecules: A generalized strong-field approximation linear combination of atomic orbitals model," *Phys. Rev A*, vol. 71, p. 063410, 2005.

[62] A. T. Le, X. M. Tong, and C. D. Lin, "Evidence of two-center interference in high-order harmonic generation from CO_2," *Phys. Rev. A*, vol. 73, p. 041402, 2006.

[63] P. Liu, P. Yu, H. Xiong, X. Ge, R. Li, and Z. Xu, "Laser intensity dependence of high-order harmonic generation from aligned CO_2 molecules," *Pys. Rev. A*, vol. 78, p. 015802, 2008.

[64] R. Santra and A. Gordon, "Three step model for high-harmonic generation in many-electron systems," *Phys. Rev. Lett.*, vol. 96, p. 073906, 2006.

[65] S. Patchkovskii, Z. Zhao, T. Brabec, and D. M. Villeneuve, "High-harmonic generation and molecular orbital tomography in multielectron systems: Beyond the single active electron approximation," *Phys. Rev. Lett.*, vol. 97, p. 123003, 2006.

[66] D. A. Telnov and S. I. Chu, "Ab initio study of orientation effects in multiphoton ionization and high-order harmonic generation from the ground and excited electronic states of H_2^+," *Phys. Rev. A*, vol. 76, p. 043412, 2007.

[67] J. Heslar, D. Telnov, and S. Chu, "High-order harmonic generation in homonuclear and heteronuclear diatomic molecules: Exploration of multiple orbital contributions," *Phys. Rev. A*, vol. 83, p. 043414, 2011.

[68] S. Sukiasyan, S. Patchkovskii, O. Smirnova, T. Brabec, and M. Y. Ivanov, "Exchange and polarization effect in high-order harmonic imaging of molecular structures," *Phys. Rev. A*, vol. 82, p. 043414, 2010.

[69] H. D. Cohen and U. Fano, "Interference in the photo-ionization of molecules," *Phys. Rev.*, vol. 150, p. 30, 1966.

[70] R. Kopold, W. Becker, and M. Kleber, "Model calculations of high-harmonic generation in molecular ions," *Phys. Rev. A*, vol. 58, p. 4022, 1998.

[71] M. Lein, N. Hay, R. Velotta, J. P. Marangos, and P. Knight, "Role of intramolecular phase in high-harmonic generation," *Phys. Rev. Lett.*, vol. 88, p. 183903, 2002.

[72] T. Kanai, S. Minemoto, and S. Sakai, "Quantum interferenece during high-order harmonic generation from aligned molecules," *Nature*, vol. 435, p. 470, 2005.

[73] C. Vozzi, F. Calegari, E. Benedetti, J. P. Caumes, G. Sansone, S. Stagira, M. Nisoli, R. Torres, E. Heesel, N. Kajumba, J. P. Marangos, C.Altucci, and R. Velotta, "Controlling two-center interference in molecular high harmonic generation," *Phys. Rev. Lett.*, vol. 95, p. 153902, 2005.

[74] B. Zimmermann, M. Lein, and J. M. Rost, "Analysis of recombination in high-order harmonic generation in molecules," *Phys. Rev. A*, vol. 71, p. 033401, 2005.

[75] M. Busuladžić, A. Gazibegović, D. B. Milošević, and W. Becker, "Angle-resolved high-order above-threshold ionization of a molecule: Sensitive tool for molecular characterization," *Phys. Rev. Lett.*, vol. 100, p. 203003, 2008.

[76] M. Busuladžić, A. Gazibegović, D. B. Milošević, and W. Becker, "Strong field approximation for ionization of a diatomic molecule by a strong laser field. II. The role of electron rescattering off the molecular centers," *Phys. Rev. A*, vol. 78, p. 033412, 2008.

[77] A. Etches, M. B. Gaarde, and L. B. Madsen, "Two-center minima in harmonic spectra from aligned polar molecules," *Phys. Rev. A*, vol. 84, p. 023418, 2011.

[78] X. Zhu, Q. Zhang, W. Hong, P. Lan, and P. Lu, "Two-center interference in high-order harmonic generation from heteronuclear diatomic molecules," *Opt. Exp.*, vol. 19, p. 436, 2011.

[79] I. Gonoskov and M. Ryabikin, "Two-center interference in high harmonic generation from diatomic molecule: detailed numerical study," *J. Mod. Opt.*, vol. 55, p. 2685, 2008.

[80] J. Zhao and M. Lein, "Positioning of bound electron wave packets in molecules revealed by high-harmonic spectroscopy," *Submitted*, 2011.

[81] C. B. Madsen and L. B. Madsen, "High-order harmonic generation from arbitrarily oriented diatomic molecules including nuclear motion and field-free alignment," *Phys. Rev. A*, vol. 74, p. 023403, 2006.

[82] C. I. Blaga, F. Catoire, P. Colosimo, G. G. Paulus, H. G. Muller, P. Agostini, and L. F. DiMauro, "Strong field photoionization revisited," *Nature Physics*, vol. 5, p. 335, 2009.

[83] W. Quan, Z. Lin, M. Wu, H. Kang, H. Liu, J. Chen, J. Liu, X. T. He, S. G. Chen, H. Xiong, L. Guo, H. Xu, Y. Fu, Y. Cheng, and Z. Z. Xu, "Classical aspects in above-threshold ionization with a mid-infrared strong laser field," *Phys. Rev. Lett*, vol. 103, p. 093001, 2009.

[84] T.-M. Yan, S. V. Popruzhenko, M. Vrakking, and D. Bauer, "Low-energy structures in strong field ionization revealed by quantum orbits," *Phys. Rev. Lett.*, vol. 105, p. 253002, 2010.

[85] O. Smirnova, M. Spanner, and M. Y. Ivanov, "Coulomb and polarization effects in sub-cycle dynamics of strong-field ionization," *J. Phys. B.*, vol. 39, pp. S307–S321, 2006.

[86] O. Smirnova, M. Spanner, and M. Y. Ivanov, "Analytical solutions for strong field driven atomic and molecular one- and two-electron continua and applications to strong-field problems," *Pys. Rev. A*, vol. 77, p. 033407, 2008.

[87] S. V. Popruzhenko, G. G. Paulus, and D. Bauer, "Coulomb-corrected quantum trajectories in strong-field ionization," *Pys. Rev. A*, vol. 77, p. 053409, 2008.

[88] M. Herman and E. Kluk, "A semiclassical justification for the use of non-spreading wavepackets in dynamics calculations," *Chem. Phys*, vol. 91, p. 27, 1984.

[89] G. van de Sand and J. M. Rost, "Irregular orbits generate higher harmonics," *Phys. Rev. Lett.*, vol. 83, p. 524, 1999.

[90] G. van de Sand and J. M. Rost, "Semi-classical description of multi-photon processes," *Phys. Rev. A*, vol. 62, p. 053403, 2000.

[91] J. Tate, T. Auguste, H. G. Muller, P. Salières, P. Agnosti, and L. F. DiMauro, "Scaling of wave-packet dynamics in an intense midinfrared field," *Phys. Rev. Lett.*, vol. 98, p. 013901, 2007.

[92] P. Colosimo, G. Doumy, C. I. Blaga, J. Wheeler, C. Hauri, F. Catoire, J. Tate, R. Chirla, A. M. March, G. G. Paulus, H. G. Muller, P. Agnosti, and L. F. DiMauro, "Scaling strong-field interactions towards the classical limit," *Nat. Phys.*, vol. 4, p. 386, 2008.

[93] L. Brugnera, F. Frank, D. J. Hoffmann, R. Torres, T. Siegel, J. G. Underwood, E. Springate, C. Froud, E. I. C. Turcu, J. W. G. Tisch, and J. P. Marangos, "Enhancement of high harmonics generated by field steering of electrons in a two-color orthogonally polarized laser field," *Opt. Lett.*, vol. 35, p. 3994, 2010.

[94] K. Ishikawa, "Photoemission and ionization of he^+ under simultaneous irradiation of fundamental laser and high-order harmonic pulses," *Phys. Rev. Lett*, vol. 91, p. 043002, 2003.

[95] P. Koval, F. Wilken, D. Bauer, and C. Keitel, "Nonsequential double recombination in intense laser fields," *Phys. Rev. Lett.*, vol. 98, p. 043904, 2007.

[96] L. E. Chipperfield, J. S. Robinson, J. W. G. Tisch, and J. P. Marangos, "Ideal waveform to generate the maximum possible electron recollision energy for any given oscillation period," *Phys. Rev. Lett.*, vol. 102, p. 063003, 2009.

[97] C. Buth, M. Kohler, J. Ullrich, and C. Keitel, "High-order harmonic generation enhanced by xuv light," *arXiv*, p. 1012.4903v1, 2010.

[98] G. L. Kamta, A. D. Bandrauk, and P. B. Corkum, "Asymmetry in the harmonic generation from nonsymmetric molecules," *J. Phys. B.*, vol. 38, p. L339, 2005.

[99] X. Bian and A. D. Bandrauk, "Multichannel molecular high-order harmonic generation for asymmetric diatomic molecules," *Phys. Rev. Lett.*, vol. 105, p. 093903, 2010.

[100] Y. Chen and B. Zhang, "Tracing the structure of asymmetric molecules from high-order harmonic generation," *Phys. Rev. A*, vol. 84, p. 1053402, 2011.

[101] H. Akagi, T. O. abd A. Staudte, A. Shiner, F. Turner, R. Dörner, D. M. Villeneuve, and P. B. Corkum, "Laser tunnel ionization from multiple orbitals in HCL," *Science*, vol. 325, p. 1364, 2009.

[102] S. De, I. Znakovskaya, D. Ray, F. Anis, N. Johnson, I. Bocharova, M. Magrakvelidze, B. Esry, C. Cocke, I. Litvinyuk, and M. Kling, "Field-free orientation of CO molecules by femtosecond two-color laser fields," *Phys. Rev. Lett.*, vol. 103, p. 153002, 2009.

[103] L. Holmegaard, J. Hansen, L. Kalhøj, S. Kragh, H. Stapelfeldt, F. Filsinger, J. Küpper, G. Meijer, D. Dimitovski, M. Abu-samha, C. Martiny, and L. B. Madsen, "Photoelectron angular distributions from strong-field ionization of oriented molecules," *Nat. Phys.*, vol. 6, p. 428, 2010.

[104] K. Burnett, V. C. Reed, J. Cooper, and P. L. Knight, "Calculation of the background emitted during high-harmonic generation," *Phys. Rev. A*, vol. 45, p. 3347, 1992.

[105] J. G. Cordes and M. G. Calkin, "Photoionization and the Born approximation," *J. Phys. B.*, vol. 13, p. 4111, 1980.

[106] G. L. Kamta and A. D. Bandrauk, "Three-dimensional time-profile analysis of high-order harmonic generation in molecules: Nuclear interferences in H_2^+," *Phys. Rev. A*, vol. 71, p. 053407, 2005.

[107] A. Gordon and F. X. Kärtner, "Quantitative modeling of single atom high harmonic generation," *Phys. Rev. Lett.*, vol. 95, p. 223901, 2005.

[108] O. Smirnova, M. Spanner, and M. Y. Ivanov, "Anatomy of strong field ionization ii: to dress or not to dress," *J. Mod. Opt.*, vol. 54, p. 1019, 2007.

[109] K. C. Kulander and B. W. Shore, "Calculations of multiple-harmonic conversion of 1064nm radiation in Xe," *Phys. Rev. Lett.*, vol. 62, p. 524, 1989.

[110] J. L. Krause, K. J. Schafer, and K. C. Kulander, "Calculation of photo emission from atoms subject to intense laser fields," *Phys. Rev. A*, vol. 45, p. 4998, 1992.

[111] J. S. Parker, B. J. S. Doherty, K. J. Mehard, and K. T. Taylor, "Time delay between singly and doubly ionizing wavepackets in laser-driven helium," *J. Phys. B*, vol. 36, p. L393, 2003.

[112] G. S. J. Armstrong, J. S. Parker, and K. T. Taylor, "Double-electron above-threshold ionization resonances as interference phenomena," *N. J. Phys*, vol. 13, p. 013024, 2011.

[113] X. M. Tong and S. I. Chu, "Density-functional theory with optimized effective potential and self-interaction correction for ground states and autoionizing resonances," *Phys. Rev. A*, vol. 55, p. 3406, 1997.

[114] J. Caillat, J. Zanghellini, M. Kitzler, O. Koch, W. Kreuzer, and A. Scrinzi, "Correlated multielectron systems in strong laser fields: A multi-configurational time-dependent Hartree-Fock approach," *Phys. Rev. A.*, vol. 71, p. 012712, 2005.

[115] P. Hohenberg and W. Kohn, "Inhomogeneous electron gas," *Phys. Rev.*, vol. 136, p. B864, 1964.

[116] E. Runge and E. K. U. Gross, "Density functional theory for time-dependent systems," *Phys. Rev. Lett.*, vol. 52, p. 997, 1984.

[117] W. Kohn and L. J. Sham, "Self-consistent equations including exchange and correlation effects," *Phys. Rev. A*, vol. 140, p. A1133, 1965.

[118] U. Manthe, H. D. Meyer, and L. S. Cederbaum, "Wave-packet dynamics within the multiconfigurational Hartree framework: General aspects and application to *NOCI*," *J. Chem. Phys.*, vol. 97, p. 3199, 1992.

[119] H. D. Meyer, U. Manthe, and L. S. Cederbaum, "The multi-configurational time-dependent Hartree approach," *Chem. Phys. Lett.*, vol. 165, p. 73, 1990.

[120] P. Botheron and B. Pons, "One-electron atom in a strong and short laser pulse: Comparison of classical and quantum descriptions," *Phys. Rev. A*, vol. 80, p. 023402, 2009.

[121] M. Protopapas, D. Lappas, C. Kietel, and P. Knight, "Recollisions, bremsstrahlung, and attosecond pulses from intense laser fields," *Phys. Rev. A*, vol. 53, p. R2933, 1996.

[122] D. V. Shalashilin, M. S. Child, and A. Kirrander, "Mechanisms of double ionisation in strong laser field from simulation with coupled coherent states: Beyond reduced dimensionality models," *J. Chem. Phys.*, vol. 347, p. 257, 2008.

[123] J. Guo, X. Liu, and S. Chu, "Exploration of strong-field multiphoton double ionization, rescattering, and electron angular distribution of he atoms in intense long-wavelength laser fields: The coupled coherent-state approach," *Phys. Rev. A*, vol. 82, p. 023402, 2010.

[124] L. V. Keldysh *Sov. Phys. JETP*, vol. 20, p. 1307, 1964.

[125] F. H. M. Faisal, "Multiple absorption of laser photons by atoms," *J. Phys. B*, vol. 6, p. L89, 1973.

[126] H. R. Reiss, "Effect of an intense electromagnetic field on a weakly bound system," *Phys. Rev. A*, vol. 22, p. 1786, 1980.

[127] W. Becker, S. Long, and J. K. McIver, "Modeling harmonic generation by a zero-range potential," *Phys. Rev. A.*, vol. 50, p. 1540, 1994.

[128] W. Becker, A. Lohr, M. Kleber, and M. Lewenstein, "A unified theory of high-harmonic generation: Application to polarization properties of the harmonics," *Phys. Rev. A*, vol. 56, p. 645, 1997.

[129] S. P. Goreslavskii and S. V. Popruzhenko, "Irregular orbits generate higher harmonics," *J. Phys. B*, vol. 32, p. L531, 1999.

[130] C. Figueira de Morisson Faria and H. Schomerus and W. Becker, "High-order above-threshold ionization: The uniform approximation and the effect of the binding potential," *Phys. Rev. A*, vol. 66, p. 043413, 2002.

[131] N. Bleistein and R. Handelsman in *Asymptotic expansions of integrals*, New York: Dover Publications, 1986.

[132] C. Chirilă and M. Lein, "Strong-field approximation for harmonic generation in diatomic molecules," *Phys. Rev. A*, vol. 73, p. 023410, 2006.

[133] A. Etches, C. B. Madsen, and L. B. Madsen, "Inducing elliptically polarized high-order harmonics from aligned molecules with linearly polarized femtosecond pulses," *Phys. Rev. A*, vol. 81, p. 013409, 2010.

[134] A.-T. Le, R. Lucchese, S. Tonzani, T. Morishita, and C. Lin, "Quantitative rescattering theory for high-order harmonic generation from molecules," *Phs. Rev. A*, vol. 80, p. 013401, 2009.

[135] C. B. Madsen and L. B. Madsen, "Theoretical studies of high-order harmonic generation: Effects of symmetry, degeneracy and orientation," *Phys. Rev. A*, vol. 76, p. 043419, 2007.

[136] J. B. Watson, A. Sanpera, X. Chen, and K. Burnett, "Harmonic generation from a coherent superposition of states," *Phys. Rev. A*, vol. 53, p. R1962, 1996.

[137] D. V. Shalashilin and M. S. Child, "Time dependent quantum propagation in phase space," *J. Chem. Phys.*, vol. 113, p. 10028, 2000.

[138] D. V. Shalashilin and M. S. Child, "Description of tunneling with the help of coupled frozen Gaussians," *J. Chem. Phys.*, vol. 114, p. 9296, 2001.

[139] D. V. Shalashilin and M. S. Child, "The phase space CCS approach to quantum and semi-classical molecular dynamics for high-dimensional problems," *J. Chem. Phys.*, vol. 304, p. 103, 2004.

[140] D. V. Shalashilin and M. S. Child, "Electronic energy levels with the help of trajectory-guided random grid of coupled wave packets. I. Six dimensional simulation of H_2," *J. Chem. Phys.*, vol. 122, p. 224108, 2005.

[141] D. V. Shalashilin and M. S. Child, "Basis set sampling in the method of coupled coherent states: Coherent state swarms, trains, and pancakes," *J. Chem. Phys.*, vol. 128, p. 054102, 2008.

[142] B. B. Augstein and J. Wu and A. Kirrander and D. V. Shalashilin and C. Figueira de Morisson Faria, "High-order harmonic generation in single electron atoms: The coupled coherent state approach," *in preperation*, vol. xx, p. xxx, 2011.

[143] R. Uzdin and N. Moiseyev, "Classical harmonic generation in rare gases," *Phys. Rev. A*, vol. 81, p. 063405, 2010.

[144] D. Bauer and P. Koval, "Qprop: A *S*chrödinger solver for intense laser-atom interaction," *Comp. Phys. Comm.*, vol. 174, p. 396, 2006.

[145] C. F. de Morisson Faria, *Interaction of atoms with intense laser fields and ultrashort pulses*. PhD thesis, Technical University Berlin, 1999.

[146] W. C. Henneberger, "Perturbation method for atoms in intense light beams," *Phys. Rev. Lett.*, vol. 21, p. 838, 1968.